FACULDADE DE ENGENHARIA DA UNIVERSIDADE DO PORTO

Design and construction of a structure with monitoring of its structural integrity

Jorge Luís Fortuna Madureira

U.PORTO
FEUP FACULDADE DE ENGENHARIA UNIVERSIDADE DO PORTO

Master's in Mechanical Engineering

Supervisor: Mário Augusto Pires Vaz

Second Supervisor: Pedro Miguel Guimarães Pires Moreira

August 4, 2022

Design and construction of a structure with monitoring of its structural integrity

Jorge Luís Fortuna Madureira

Master's in Mechanical Engineering

August 4, 2022

Abstract

The integration of structural monitoring systems that are able to analyse the behaviour of a structure under various service loads, to detect existing damage and to estimate the service life, has become increasingly possible and desirable by those responsible for its management. Ideally, these systems should provide relevant information about the parameters being monitored, such as displacements, stresses, strains, accelerations, among others, in order to enable those responsible for the supervision of the structure to make the right decisions in a timely manner. The present work focuses on the design and construction of a bridge prototype with the subsequent design of a system for monitoring its structural integrity.

The reasons that led to the increasing demand for the implementation of these systems were stated and the methodology to be followed for such purpose was also detailed. The operation and advantages of various strain measurement technologies were exposed and examples of bridges in which they are currently being used were given. The experimental character was initiated by the study of the best truss style to be implemented, having designed, built and instrumented the bridge for the study of strains and vibrations. Different load and impact tests were carried out and compared with numerical simulations of the tests under the same conditions and prediction calculations, to evaluate the accuracy of the measuring devices.

Finally, the obtained deformation results for each of the load tests and the validity of the frequencies observed in the various impact tests were discussed with the help of graphs and tables. The conclusions were detailed and some proposals for future works were suggested.

Keywords: Structural health monitoring, strain, truss bridge

Resumo

A integração de sistemas de monitorização estrutural que sejam capazes de analisar o comportamento de uma estrutura sob várias cargas de serviço, de detetar dano existente e de estimar a vida útil, tem vindo a ser cada vez mais possível e desejada pelos responsáveis pela sua gestão. Idealmente, estes sistemas devem fornecer informação relevante sobre os parâmetros em monitorização, tais como os deslocamentos, tensões, deformações, acelerações, entre outros, afim de permitir aos encarregados pela supevisão da estrutura de tomar as decisões corretas e atempadamente. O presente trabalho foca-se no projeto e construção de um protótipo de uma ponte metálica com posterior conceção de um sistema de monitorização da sua integridade estrutural.

Enunciaram-se os motivos que levaram à crescente procura pela implementação destes sistemas e a metodologia a seguir para o efeito foi também detalhada. O funcionamento e vantagens de várias tecnologias de medição de extensões foram expostas, dando-se exemplos de pontes em que estas estejam atualmente a ser utilizadas. O caráter experimental iniciou-se pelo estudo do estilo de treliça a implementar, tendo-se projetado, construído e instrumentado a ponte para o estudo de deformações e vibrações. Diferentes testes de carga e impacto foram realizados e comparados com simulações numéricas dos ensaios nas mesmas condições e cálculos de previsão, para avaliar a precisão dos aparelhos de medição.

Por último, procedeu-se à discussão dos resultados obtidos de deformação para cada um dos ensaios de carga e à validade das frequências observadas nos vários testes de impacto com a ajuda de gráficos e tabelas. As devidas conclusões foram detalhadas e sugeriram-se algumas propostas de trabalhos a realizar no futuro.

Keywords: Monitorização estrutural, extensão, ponte treliçada

Acknowledgements

Personally I would like to start by thanking my supervisors, Professor Mário Vaz and Professor Pedro Moreira for their constant availability and dedication in guiding me throughout the project and for all the knowledge shared not only in the more theoretical parts, but also in the experimental aspects of the work.

A special thanks to the INEGI institution and in particular to the LOME section, for making space available for the various stages of construction and monitoring, and to the engineers Job Silva, Behzad Farahani, Nuno Viriato, Andreia Flores and Rogério Lopes for their essential help in the many different phases of the project.

I would like to thank all my friends with whom I have shared unforgettable moments in the course of my academic career, without forgetting to appreciate their constant help and affection, specially to Francisca Guerra and Mário Oliveira for the spirit of camaraderie and unity that has been developed since the start of the dissertation.

Finally, a big heartfelt thanks to all my family, but in particular my parents and my siblings for their unconditional support throughout my academic course.

Jorge Luís Fortuna Madureira

Contents

List of Figures

List of Tables

Abbreviations

NDT	Nondestructive testing
SHM	Structural Health Monitoring
DAQ	Data Acquisition System
ADC	Analog-to-Digital Converter
FBG	Fiber Bragg Grating
FFT	Fast Fourier Transform

Chapter 1

1. Introduction

1.1 Context

Bridges are one of the most important structural works of art present in every society, allowing easy connection between people and cultures, and contributing to the prosperity of the economic sector of the surrounding regions. They also make it possible to cross between places that would otherwise be inaccessible and ease traffic congestion in busy areas [9].

Because of these crucial roles in today's day to day lives combined with their size and complexity, it is imperative to ensure their safety and durability through a series of adequate measuring and monitoring techniques, as bridges, much like any other structure, are prone to material ageing and subsequent deterioration. Furthermore, damage caused by intense environmental conditions, such as strong winds, earthquakes or extreme heat, accidental collision of vehicles and increasing traffic loads, combined with possible design defects [1], can lead to the loss of load carrying capacity, resulting in the considerable decrease of the structure's lifespan.

Although, most bridges undergo somewhat regular inspection and maintenance works (mostly annual), in which visual observation and occasional simple non-destructive tests (NDT) are the main methods for assessing structural integrity, many defects may remain unidentified or unsolved. Additionally, it is not uncommon to have some sections along the structure that are difficult to access where extra equipment and more numerous teams are required to carry out the inspection operation and insecurity might be a factor to consider. Naturally, these more complex measures considerably increase the time spent on the tasks and may also, in some works of art, result in their temporary closure, which ultimately leads to higher amounts of money spent in the process [10]. One effective tool to overcome these obstacles is to have a fully integrated and continuously operating monitoring system installed in the structure.

Structural health monitoring (SHM) main goal is to accurately and efficiently monitor a structure's *in-situ* behaviour, analyze its performance under varied service loads, detect damage or degradation, and estimate the structure's health, also know as condition. The SHM system should be able to give trustworthy information about the various parameters being monitored to ensure the structure's safety and integrity on demand. Furthermore, the system serves as a useful tool to assess, validate and correct the numerical models and hypotheses considered when designing and carrying out the construction stages of the structure [11], thus enabling the people responsible for its maintenance to manage, on the basis of data acquired from a sensor network installed in the most relevant locations, the decisions to be taken within the scope of inspection, repair and, if applicable, rehabilitation [12].

Ideally, the system needs to be able to store relevant information relating to a variety of events such as adverse environmental conditions, heavy vehicle traffic or disasters, and transmit that data wirelessly to an acquisition system in which engineers can observe the state of the structure. Given the recent technological advancements in the areas of sensing, data collecting, processing, and data management, the application of SHM systems in bridges as become widely desirable, although it is not as of yet a common practice [13].

1.2 Motivation

The rising trend and human desire to design bridges with increasingly complex geometries, in high-risk locations and using innovative materials, in order to develop more rigid and durable structures from a mechanical point of view and to reduce design and maintenance costs, demonstrates the demand and importance of installing monitoring systems. The evaluation of the structure's behaviour in the construction and operation phases is of enormous interest as it allows designers to validate their hypotheses or to make the necessary corrections to the numerical models in time in order to obtain a more accurate assessment of the bridge's response. Continuous monitoring provides critical data for bridge management decision-making, both in terms of maintenance operations and future projects, because it allows the effectiveness of implemented solutions to be assessed [11, 14].

The concern for improving the safety of structures and increasing their life span is also a strong motivation for the implementation of these systems. According to the USA's 2021 infrastructure report card, approximately 7.5% of its bridges were in a structurally deficient condition in the year 2019 and the number of bridges in the process of being designated as having fair condition is increasing annually. It is also estimated to take over 50 years to repair all of these bridges, given the current state of slowly increasing rate of improvement in repair, rehabilitation and replacement, and that an increase of 58% on the annual spending on bridge rehabilitation (14.4 billion dollars) is needed to improve the condition [15].

Although, both the need and the benefits of SHM systems are clear, not only in terms of safety reassurance but also in the more realistic understanding of bridges' real time defects and behaviour, there is still some push back on the costs such implementation will have for an effective and accurate measurement [16]. However, due to unfortunate disasters, such as the collapse of the Hintze Ribeiro bridge, in Castelo de Paiva, Portugal, on march 2001, that claimed 59 lives [11] or the collapse of the St. Anthony Falls Bridge (also known as the I-35W bridge), over the Mississippi

River in Minneapolis, USA, on august 2007 in the middle of rush hour killing 13 people, injuring 145 others and generating massive economic losses in the region, additional pressure is put on bridge building authorities and companies to develop and implement more advanced and cost-effective monitoring technologies [17, 16].

It is especially important to give proper attention to old metal bridges that are still in service, although they show a significant level of deterioration. In the USA alone, 42% of bridges (about 259,000) were built at least 50 years ago, and those in a structurally deficient state were completed about 69 years ago, on average, and most of them were designed for a service life of about 50 years. The natural increase in traffic intensity and vehicle speed results in a greater demand on the part of the structures in terms of the loads they have to support, efforts that were most probably not considered in the initial project [15].

When structural damage is detected in its early stages, it is possible to take action to avoid the structure from having to support loads for an extended length of time while it is damaged. As a result, over designing bridges is no longer needed, lowering construction costs and improving the overall efficiency of infrastructure projects. Early damage detection also allows for repairs to be undertaken as soon as the damage occurs, which can substantially reduce repair and maintenance costs and avoid future deterioration [9]. Additional cost savings can be realized by reducing site visits and manual examinations by maintenance employees, as relevant data can be sent remotely from the structure to an offsite location for analysis in some circumstances [1, 15].

1.3 Dissertation objectives and structure

1.3.1 Objectives

The work aims to design and build a structure with monitoring of its structural integrity. The structure selected was a truss metal bridge on a reduced scale that approximately represents a real bridge. In a first instance, through experimental mechanics techniques, it is intended to validate the numerical solutions obtained from the modelling of the structure in appropriate software, and then the network of sensing devices should be able to measure in real time the strains due to service loads.

1.3.2 Structure

The present dissertation is divided into the following chapters:

In Chapter 1, a contextualisation is given on the subject of structural monitoring of bridges, highlighting the most motivating reasons for its implementation. In addition, the main objectives of the present thesis are listed.

Chapter 2 covers all of the research conducted in the field of structural monitoring techniques and methods in terms of strain is presented, highlighting the methodology that must be followed for the correct installation of an SHM system. Several types of strain gauges are addressed with reference to their mode of operation, advantages and disadvantages.

Chapter 3 shows in great depth the steps that preceded the construction phase, emphasizing the study of the advantages of truss bridges, the choice of the best design and the design of the gusset plates, as well as the numerical modeling of the structure. The entire construction process was also described in great detail.

In Chapter 4, is where the experimental component of the work carried out is described. A first experimental and numerical evaluation of the vertical displacement is performed. Following , the sensor installation methodology is detailed, with reference to sensor type specifications, surface preparation, and type of bonding to the structure. All the tests performed were supported by numerical simulations or prediction calculations and are described in this chapter, with the results being discussed in the final section.

Finally, in Chapter 5, the final conclusions are made about the project and potential additional work to be performed further in the future is proposed.

Chapter 2

State of the art

2.1 Methodology of structural health monitoring

Although, structural implementation of measuring instruments may seem an expedient process, in reality, in order to achieve an accurate monitoring of the behaviour of artworks, a detailed conception of the procedure to be performed and of the intended objectives for the system, has to be carried out. Only by the sequential obedience of the methodology outlined by the designer, from the construction phase of the structure (if applicable) to the operation phase, the implementation of a monitoring system is truly beneficial from an economic and practical point of view. Frequently, SHM systems are composed of a network of sensors, software for acquisition, transmission and processing of data, and a data storage and management system as is shown in Figure 2.1 [1]. Information regarding each of the steps to follow for the correct implementation of a health monitoring system is detailed below.

2.1.1 Structure identification and risk analysis

The response of each bridge depends on a large number of factors such as its length, its style, the load cycle, the materials used, among others. For this reason, the greater or lesser probability of the occurrence of a particular type of risk will also vary, and it is important to perform a proper analysis of the risks in the design of structural monitoring systems, as well as of the locations where it would be most beneficial to obtain information about their severity. This evaluation arises as a requirement to determine which quantities should be monitored [18].

These quantities can be associated to the global behaviour of the structure (deflections, displacements, rotations), to the local behaviour of the structure (stresses, strains, crack widths) or even associated to environmental conditions (temperature, humidity, wind). Most bridges are subject to considerable temperature variations, and this is a factor of growing concern, since it may induce deformations in the structure, as well as compromise the accuracy and reliability of the measurement equipment. Therefore, a careful installation of temperature gauges combined with other sensors is essential for a more reliable monitoring of the real behaviour of the structure [18, 1].

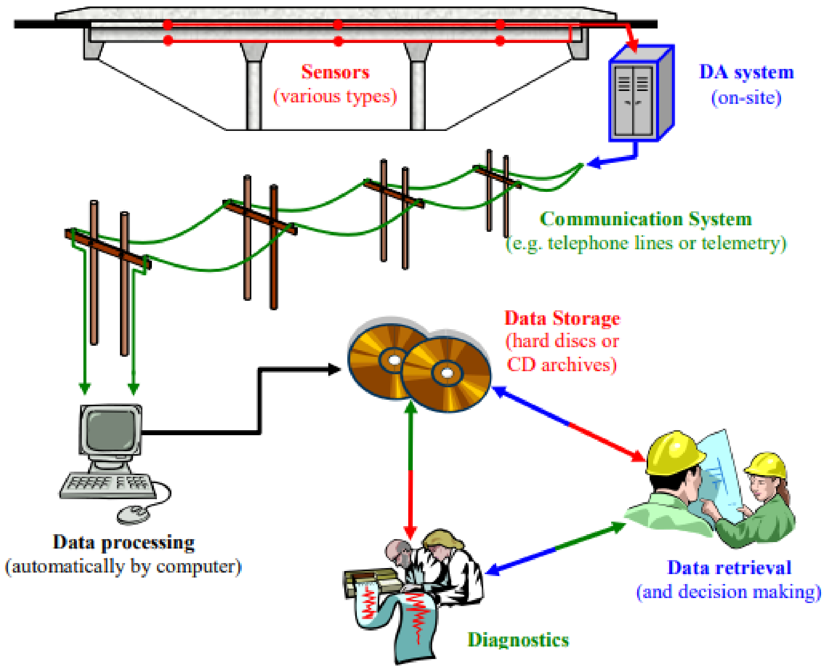

Figure 2.1: Schematic of a typical SHM system design [1]
.

2.1.2 Sensor selection, installation and calibration

Once the parameters to be monitored and the areas to be instrumented have been established, the next step is to choose sensors with the appropriate specifications to measure the response in their future location, taking into account their cost, life span, precision, resolution, stability and the intended quantity, for example. Often, sensors that are generally superior in technological terms to others may not be ideal for installation at a particular site, due to access restrictions, environmental conditions or even unforeseen design issues. It is also in this phase that we analyse the type of cables and acquisition systems available on the market and which are most suitable for installation in the real conditions of the job [18, 19].

Next, the installation and subsequent calibration of all systems must be carried out in accordance with the supplier's specifications and with appropriate supervision without compromising the structure's behavior [18, 1].

2.1.3 Data acquisition system

Already in the operation phase, the information collected by the network of sensors, whether they are wired or wireless, has to be transferred to a data acquisition equipment located close to the structure. The data acquisition system (DAQ) collects analogue signals issued by the sensors, conditions them and converts them into relevant data before they are transferred to a location outside the worksite. In certain works, the amount of data stored becomes so exaggeratedly large that it is necessary to implement sampling simplification techniques, so as not to compromise the usefulness of the SHM system and overload it, making interpretation difficult. Although, in the case of dynamic monitoring, the rate of data is substantially higher to accurately measure the structure's response [18, 1, 19].

To properly select a DAQ, similar to the choice of the most appropriate sensors, there are a number of important criteria to consider, including: the type of analog-to-digital converter (ADC) that converts the analog voltage signal to a digital value, as this influences the accuracy and speed of the measurements; the architecture of the equipment; the operating technology of the sensors used that dictate many of the characteristics of the DAQ (accuracy, speed, resolution, input configuration, input range); and data acquisition mode.

There are two basic types of data acquisition modes, polled and event-based. In polled mode, a data acquisition system is continuously run, and the associated sensor signals are received and recorded at regular intervals. A polled data acquisition mode is ideal for sensors that measure physical variables that are static or change slowly over time. In event-based data acquisition sensor signals are only collected during the occurrence of a pre-defined event of interest (either deterministic of random). Depending on the pace of the event, the physical variables detected by the sensors during the occurrence of such events can change slowly or quickly over time [19].

2.1.4 Data preprocessing

The initial calibration of sensors and data acquisition hardware followed by their periodic recalibration has been proved to be indeed beneficial, but nowhere near sufficient for accurate data cleansing. Before it is stored, obtained data will most probably contain irrelevant parts of information that must be eliminated [1, 18]. Some of the available preprocessing operations of data include filtering, which aims to smooth the signal in specific frequency ranges and remove any existing noise, integration of algorithms in the DAQ's software to evaluate and validate incoming data, rejecting extraneous information and noise automatically, and the implementation of methods to appropriately sample data at a certain rate, avoiding the analysis of vast amounts of data. The latter, also known as data compression, is typically applied when continuous monitoring is desired and serves as a tool to record only when changes in readings occur, when data exceeds an established threshold value or when high peak values due to a specific event are observed [1, 19].

2.1.5 Data transmission

The transmission of data from the acquisition system to the location where processing, evaluation and long-term storage will occur is one of the most beneficial and crucial aspects of any structural monitoring system. This communication enables the parameters being measured to be observed remotely, so that it is not necessary to visit the site to carry out inspections or to make decisions about maintenance operations [1].

2.1.6 Data storage and diagnosis

When storaging processed data, one must make sure that it will be available for analysis and future consultation without the risk of corruption or overwriting with newer data. Thus, a reliable unit with sufficient memory to hold large amounts of easy to read data should be selected. The task that follows, which generally coincides with the final one in the design of a SHM system and considered the most difficult, is the decision making step based on collected and processed data. A deep structural knowledge on the behaviour of structures and what causes are likely to dictate that behaviour, is required. The sophistication of the analysis will vary depending on the monitoring program's and SHM system components' needs. In some cases, most of the workload associated with data interpretation is demanded from the system itself, that should be capable of executing suitable commands upon a certain set of criteria, being the issue of an alert the most basic example [1].

2.2 Strain measurements

The instruments designed to measure the relative distance between two well-defined points of a structure due to applied force, also known as gauge-length, are called strain gauges and these can be mounted directly on a surface or embedded in structural elements. The different types of sensors most commonly found in SHM systems are shown below, with emphasis on their operating principle, benefits, and the works in which they are currently implemented.

2.2.1 Foil strain gauge

Electrical resistance strain gauge

These sensors, also known as electrical resistance gauges, are the most economically affordable on the market and, mostly for this reason, the most frequently used. They are applied directly to the surface of structural elements, generally metallic, by proper adhesives and are connected to a data acquisition system by means of connecting cables. They consist of a resistive metal foil in a specific configuration (rosette, full bridge, linear, double linear, etc.) supported by a flexible insulator that measures the deformations through the variation of the electrical resistance [16, 1]. It registers compression as a decrease in resistance (negative strain) and traction as an increase in resistance (positive strain) [20, 1, 21].

Even though these are the most commonly observed, integrated into monitoring systems, their proper selection and careful surface preparation are factors of great importance, since an effective measurement depends on them. Some criteria to be considered are accuracy, maximum extension, sensitivity to environmental conditions, lifetime, nominal electrical resistance, thermal expansion coefficients of both the sensor and the material being instrumented and the gauge factor [11].

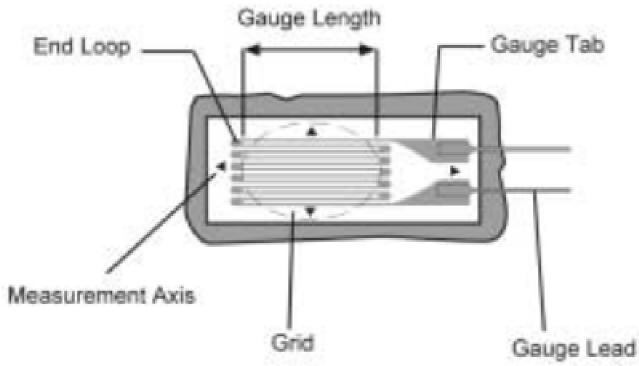

Figure 2.2: Schematic of a foil strain gauge of the resistive type [1].

Weldable strain gauge

Another type of foil gauge are weldable strain gauges that are manufactured attached to a metal support especially suitable for spot welding on steel elements such as rebar. Although electrical resistance strain gauges have a better measurement accuracy, these sensors appear as an alternative and solution in places of desired instrumentation where Adhesive Bonding is not suitable and environmental conditions are more severe [1, 2].

Embedment strain gauge

When designing monitoring systems to be implemented in structures, it is common to require the instrumentation of concrete elements throughout their life, from the construction phase to the operation phase. To this end, there are embedment strain gauges available on the market for measuring deformations inside these components. These are characterised by their long detection grid, embedded in a polymer concrete body, which allows the average strain of the aggregate materials to be measured instead of measuring localised strains due to discontinuities in the concrete. The sensor is protected from mechanical damage during casting, from moisture and from corrosive attack by the polymer concrete block in which it is embedded [1, 3].

Despite its low cost and effective use and implementation in locations with diverse environmental and operating conditions, this range is not suitable when the instrumented areas and the data acquisition equipment are considerably distant from each other. The low voltage levels of the

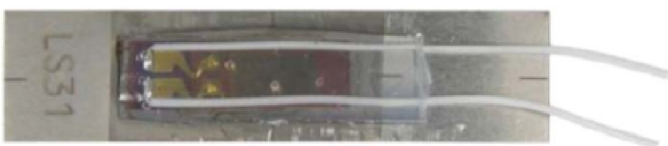

Figure 2.3: LS31 weldable strain gauge distributed by HBM [2].

Figure 2.4: EGP-Series embedment strain gauge distributed by Micro Measurements, VPG [3].

signals produced by the sensor during measurement are highly susceptible to electromagnetic interference. If these signals are not properly conditioned, they can lead to inaccurate measurements and incorrect analysis, as electrical noise overrides the interference generated by external sources. When the dynamic parameters of a structure are to be measured and evaluated, the problem of signal interference becomes even more critical, as filtering the signal may result in the characteristics of the original signal being altered [1].

2.2.2 Vibrating wire strain gauge

These strain gauges operate on the relationship between the vibration frequency of a string and the associated tension and are designed to be welded to steel structures or embedded in concrete. They have two flanges attached at the ends, which are the elements to be fixed to the structure, with a string under tension between them. When the material deforms, the two blocks move relative to each other, resulting in a change of tension in the string and consequently a change of its resonance frequency. There is also a magnet/coil in the centre of the strain gauge which excites the string and measures its vibration frequency, which is then converted into strain units by suitable equipment [22, 1, 23]. The monitoring system of the recently reconstructed I-35W bridge in Minneapolis, USA, uses vibrating wire strain gauges where the measurement of static strain, aims to address concrete shrinkage and creep [18]. The Sutong cable-stayed bridge in China, that carries the G15 Shenyang-Haikou expressway, has in its SHM system 96 vibrating wire strain gauges and 309 resistive strain gauges [24]. On the Lezíria bridge, that forms part of the A10 highway from Bucelas to Carregado in Portugal, vibrating wire strain gauges were installed on steel bars to be embedded in the piles of the main bridge [25].

A very advantageous aspect of this type of sensors is the possibility to have a great distance between the instrumented points and the signal acquisition equipment, since the output of the signal in frequency is practically immune to electrical noise, without a considerable degradation of the signal. Their simple installation is also a key factor contributing to their widespread use, although attention must be paid to the available space on site, as vibrating wire strain gauges are usually of considerable size [22, 1]. Additionally, in the same sense as the foil strain gauges, these sensors are not suitable for dynamic applications, since its measuring period is quite long when in comparison to others, being inadequate where high frequency readings are intended. They also have built-in temperature gauges, due to their sensitivity to temperature variations, allowing not only the value of this parameter to be known at the place of instrumentation, but also the appropriate correction in the strain measurement [11].

Figure 2.5: Vibrating wire arc weldable strain gauge distributed by RST Instruments Ltd [4].

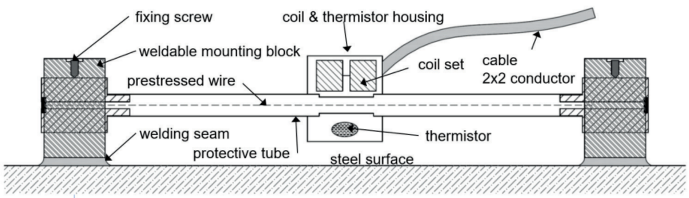

Figure 2.6: Schematic of a vibrating wire arc weldable strain gauge (adapted from [5]).

2.2.3 Fibre optic strain gauge

In recent decades, there has been an increase in the application of fibre-optic sensors for monitoring structures, largely due to advances in telecommunications and the growing size of construction sites and the adverse conditions to which they are subjected. This range of sensors is especially attractive for remote monitoring due to the high sensitivity to external physical perturbations it can measure, its immunity to electromagnetic interference, its small size that facilitates the installation on surfaces or embedded, its stability and its high sensitivity [26, 14].

Optical fibers are very thin "lines" of silica glass capable of signal transmission across large distances and are made of three components. A core similar in size to human hair, with the functionality to transmit signals by light waves, covered by a lower density layer of reflective glass, which guides and reflects the light waves along the core called cladding. A polymeric coating protects the fibre from environmental damage and promotes flexibility without the fibre breaking.

The principle behind fiber optic sensing technology is that light waves traveling down an optical cable vary the light patterns and signals depending on the cable's condition. A light beam is sent down the fiber optic cable to the sensor, modified by the amount of change in length of the sensor (expansion or compression). The sensor sends an optical signal to a measuring device that converts reflected light into numerical measurements of sensor length change. These values reveal exact levels of structural strain at the sensor location and have to be compensated in terms of temperature, as these sensors are extremely susceptible to temperature variations.

Since fibre optic sensors operate by measuring variations in the physical properties of the propagated light that passes through them, there are several sensors that operate according to different light detection techniques. Within these types the ones that stand out are the spectrometric sensors and the Brillouin scattering sensors.

Spectrometric sensors - Fiber Bragg Grating

Bragg sensors or Fiber Bragg Gratings (FBG) are the sensors within this technology that have been growing in use the most. To effectively detect strain variations, in the design of optical fibres, the core has to undergo an inscription process with so-called fibre Bragg grating. This consists of a unique pattern of interfering material (reflectors) which reflect light differently from the rest of the core. The imposed spacing of the grating is proportional to the wavelength of light reflected when a light pulse is directed along the fiber. These spacings vary if the fibre undergoes strain (extension or compression) which causes a variation in the wavelength of the reflected light. The refractive index of the core varies periodically due to the variation in the shape of the grating when strained. The optical fibre is connected to an interrogator that continuously transmits light at different wavelengths, which is reflected by the fiber Bragg grating and returned to this equipment. The data obtained from this spacing can then be converted into strain values and used to assess the condition of the instrumented zone (local measurement).

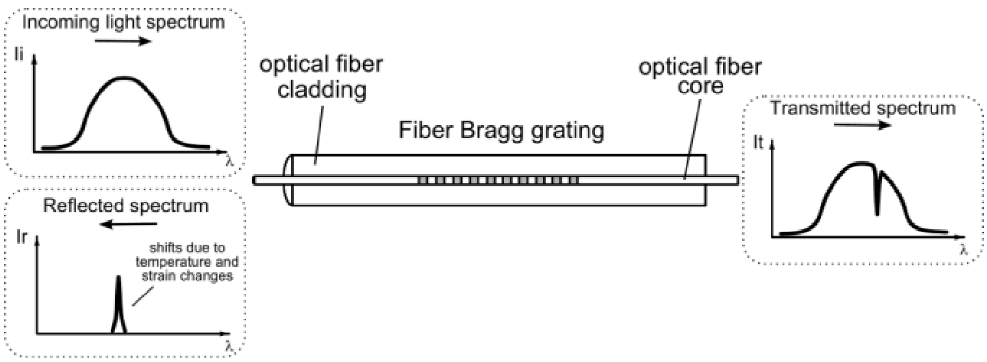

Figure 2.7: Schematic of the functional principle of FBG sensors [6].

These sensors can be used for both static and dynamic structural monitoring, are weldable and bondable and can be effectively multiplexed. The latter aspect is actually extremely useful in the sense of SHM applications where multiple sensors are required. Multiplexed sensing is the integration of a number of independent gauges to measure perturbations across a large structure

[1]. Kersey et. al 1993 [27], explored a technique of wavelength division multiplexing by using fiber Bragg grating sensors. However, even when single-point fiber sensors are multiplexed to form quasidistributed fiber sensors, they do not give the wealth of information that inherently distributed optical fiber-based methods that operate throughout the full fiber length may supply [7]. This type of sensor accounts for 15% of the total number of sensors included in the SHM system of the Lezíria bridge, intended for strain, vertical displacement and temperature measurements [25]. Also in Portugal, the Eiffel bridge in Viana do Castelo has been being monitored by FBG sensors for bondable applications with a fast-curing cyanoacrylate-based adhesive [12]. The Caofeidian bridge in China, benefits from FBG sensors for both temperature and strain measurements, having 34 sensors installed for each quantity. The existing monitoring system of the three-span cable-stayed Jindo bridge in Korea, has 24 incorporated FBG sensors [24].

Brillouin scattering sensors

Distributed fiber sensor technology has successfully been employed in a variety of structural applications focused on its monitoring, demonstrating the advantages of distributed fiber sensors in which the optical fiber itself acts as a sensing element. This increases the measurement capabilities in terms of sensing distance and reduces the overall cost. One of the most commonly used distributed fiber sensors currently is based on the (spontaneous or stimulated) Brillouin scattering phenomena, although other sensors based on different optical scattering effects exist such as the Raman scattering and Rayleigh back-scattering.

Light interacts with the constituent material as it travels through the fiber and a small fraction is back scattered. Part of the back scattered signal has specific intensity or spectral features that are dependent on local stimuli applied to the environment near the fiber and allow various measurements of external factors like strain and temperature at multiple locations. In Figure 2.8, the frequency spectrum of scattered light is illustrated which includes Raman, Brillouin and Rayleigh scattering.

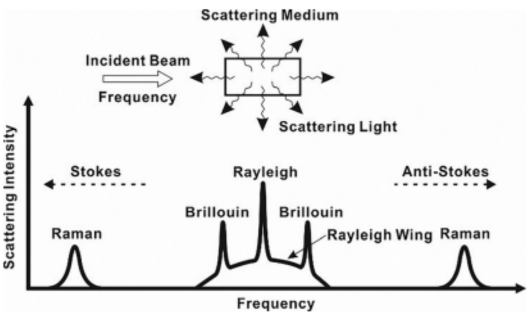

Figure 2.8: Illustration of a frequency scattering spectrum [7].

Rayleigh scattering is characterized by a single centered peak at the incoming light frequency that results from non-propagating material-density fluctuations caused by entropy fluctuations, culminating in spectral broadening without a central frequency shift. Because no frequency shift is induced between the incident photon and the scattered photon, Rayleigh scattering is known as elastic scattering [7, 28]. The interaction of light with sound waves or acoustic phonons of a material causes Brillouin scattering. The photon-phonon inelastic interaction in silica optical fibers leads to a frequency shift of the scattered light that depends on the velocity of the sound wave. Brillouin scattering is classified as inelastic scattering because of the frequency shift between the incident and scattered light fields. Stokes components refer to scattering shifted to lower frequencies with regard to incoming photons, while anti-Stokes components refer to scattering shifted to higher frequencies. The Brillouin Gain Spectrum (BGS) is dependent on the presence of heating or fiber expansion in measurements based on spontaneous Brillouin scattering. The Brillouin Frequency Shift (BFS) is a frequency offset between the peak of the BGS and the spectrum of the incident light that is linearly dependent on the strain or temperature at each point of the fiber [29, 28, 7].

This type of sensing technology has been implemented to monitor cracks and anomalous or changes in the behaviour of the Götaälvbron bridge over the Göta river in Sweden, by means of distributed fibre optic strain sensors, and to study the thermal effects on the bridge and strain sensors as well as extreme temperatures using distributed fibre optic temperature sensors [18].

Chapter 3

Design and execution

This chapter presents in detail the procedures carried out for the development and construction of the structure adopted, highlighting the motivations for its choice. In a first instance, a brief history about truss bridges is presented, addressing the main advantages of this type of design and the risks to which they are subjected. Secondly, the preparation of the numerical model of the structure and the justification of all the solutions and simplifications taken, is highlighted. The construction stage is set out in the third section of this chapter and covers the ordering phase of the required material, assembly sequence and final assembly.

3.1 Project assignment and research

The first objective of the work involves the design and construction of a structure, and a metallic truss bridge was selected as the test structure. This was mainly based on the fact that it was considered easy to design a truss compared to other bridge styles, and that the objective of another thesis being developed at the same time was to study methods for measuring deflections in steel bridges, so that we could put the useful and the pleasant together. One other particular aspect was that it was suggested that the structure be fully dismountable, i.e., after being built and put into service, if necessary, all the structural elements could be dismantled and reassembled elsewhere.

In order to fully understand what truss styles exist so as to begin to conceptualize the bridge to be built, a research was conducted on the subject.

3.1.1 Truss bridges

A truss is a rigid and strong structure that utilizes materials in a efficient and cost effective manner. They are composed of horizontal, vertical and inclined elements that connect with others in locations called the nodes [30]. These elements form a base shape in the form of a triangle that is typically repeated along the structure as this demands that the angles between elements remain the same, resulting in a stable shape. However, for a structure, in the particular case of a bridge, to be considered as a truss and analysed as one, a few assumptions ought to be made. Firstly, the joints are assumed to be pin-connected allowing the rotation of the members. Additionally, any existing loads are only ever applied at the joints, meaning the members can only carry axial loads, being either in compression or tension which substantially simplifies its analysis.

There are several designs of truss bridges and these present differences mainly at the level of the distribution of loads, beyond the clear visual differentiation. Following, some examples of configurations are presented, highlighting the main differences between them. In the Howe truss the vertical elements are in tension, while the diagonals are subject to compression. The elements that due to the bridge design will be subject to compression, are designed to support the buckling effects felt in the structure, and are therefore thicker elements. This ultimately leads to an increase in the total project costs. In the Pratt truss, on the other hand, the inner vertical members are in compression and the inner diagonal members in tension, resulting in a more economical construction as the larger members are tensioned. Warren truss design takes advantage of equilateral triangle shapes, combining strength and efficient use of material, as fewer components are needed than in the previous styles, making this one of the most efficient solutions. The diagonal members alternate between tension and compression according to the loads applied to the structure.

3.2 Modelling

In order to begin with the modelling phase of the project a rough sketch of the bridge should be made and afterwards, if necessary, make the appropriate improvements. Additionally, Bosch 20x20 aluminium linear profiles will be defined as the structure's struts, as shown in Figure 3.1, being these the cheapest and smaller profiles the company distributes. Keeping that in mind, it was decided to model a Warren truss bridge with $2,4m$ in length and $1m$ in width with 4 equilateral triangles without chords connecting the two sides from above, to allow the possibility of evaluating the load a person induces while standing on top of it (see Figure 3.2). It was concluded that this design would be much more simpler to build and model and would require less material, thus contributing to the overall cost saving.

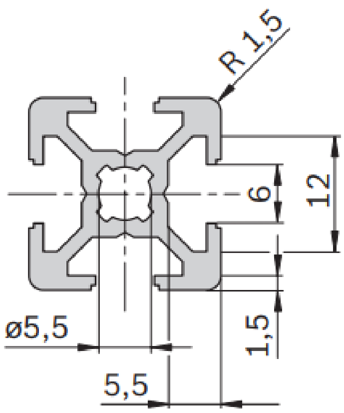

Figure 3.1: Geometry of the chosen profile [8].

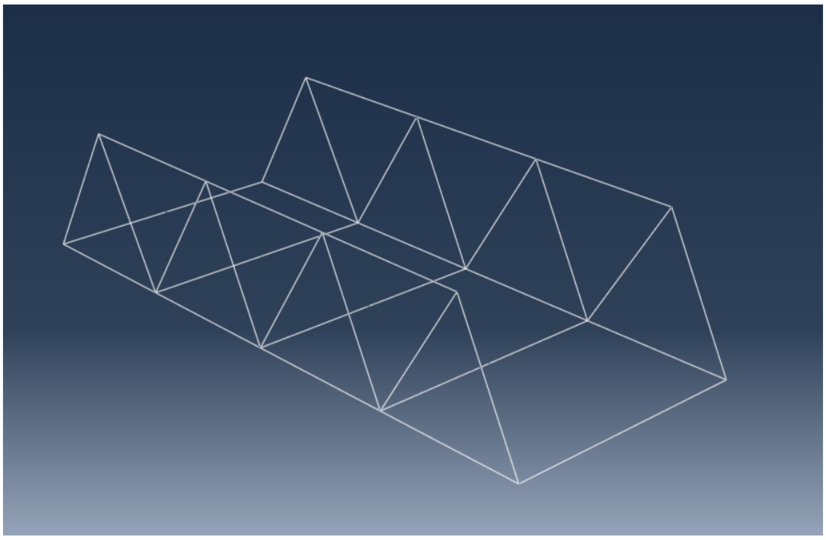

Figure 3.2: Initial three-dimensional design sketch of the bridge.

One other aspect to consider before initiating the bridge modelling is to choose which type of base feature should the model be based on: solid, shell or wire. To address this question and properly select the most representative element for the intended structure, the profile deflection equation given by the supplier (3.1) was used to compare with the results of the different hypotheses considered (more information in Appendix A.2). For such purposes, a series of modelling studies were conducted on a 100 mm profile statically loaded at mid-length to analyse which of the element displacements would come closest to the expected value. The theoretical calculated value for the deflection f, considering $F = 250N$, $L = 100\ mm$, $E = 70000\ N/mm^2$ and $I = 0.7\ cm^4$ was $2.657 \times 10^{-3}\ mm$.

$$f = \frac{F \times L^3}{192 \times E \times I \times 10^4} \tag{3.1}$$

The first approach made was to consider solid elements to mesh the profile with the intended length, exact geometry and material properties (available in the supplier's catalogue - Appendix A.1). The ends were considered as fixed and a load of $250N$ was applied in the negative y direction. Ideally, by modelling the profile as a solid one may think that the deflection results would come very close if not equal to the anticipated value. However, that as not the case as the obtained value was higher by about an order of magnitude, as shown in Figure 3.3. Furthermore, it was noticed that the computational cost needed for the simulation of a "simple" $100mm$ part is immense, mainly due to the high number of elements utilized (79632 elements) and necessary to mesh the complex geometry of the profile.

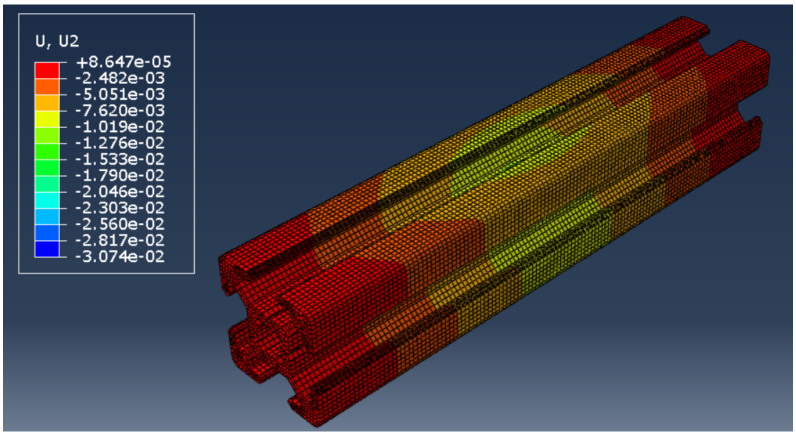

Figure 3.3: Resulting plot of the part by solid element modelling.

Secondly, the wire shape hypothesis was evaluated. For this type of element, it is required to define the shape of the profile most representative of the cross-section of the structure's elements. Considering the complexity of the adopted profile, it was decided to approximate its geometry to a square (box) profile with a side length of $20mm$ and a thickness of $2.25mm$, since the resulting area of $159.75mm^2$ is very close to that of the real profile ($160mm^2$). Moreover, in order to have another means of comparison, one more profile shape was analysed (generalized profile) assuming as the input data the cross-sectional area, principal moments of inertia and torsional rigidity of the Bosch profile, all available in the above-mentioned catalogue. Both simulations had the same boundary conditions and loads applied as the solid model and the respective results of the vertical displacement are shown below (see Figure 3.4 and Figure 3.5).

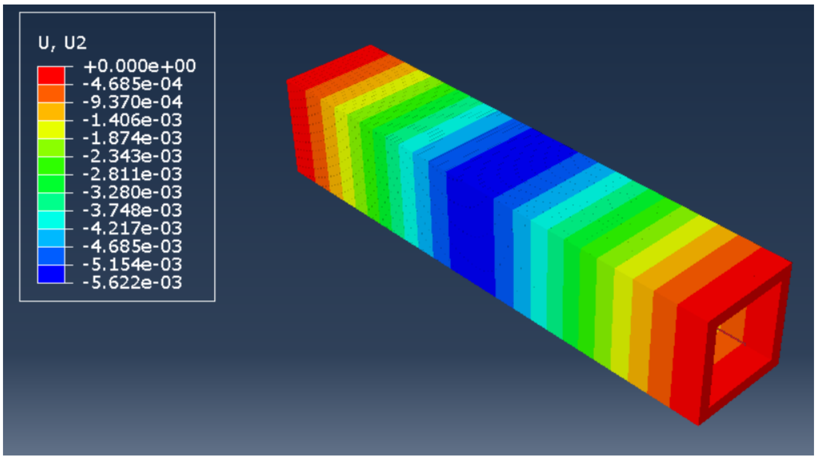

Figure 3.4: Resulting plot of the part by considering a wire base feature with a box profile shape.

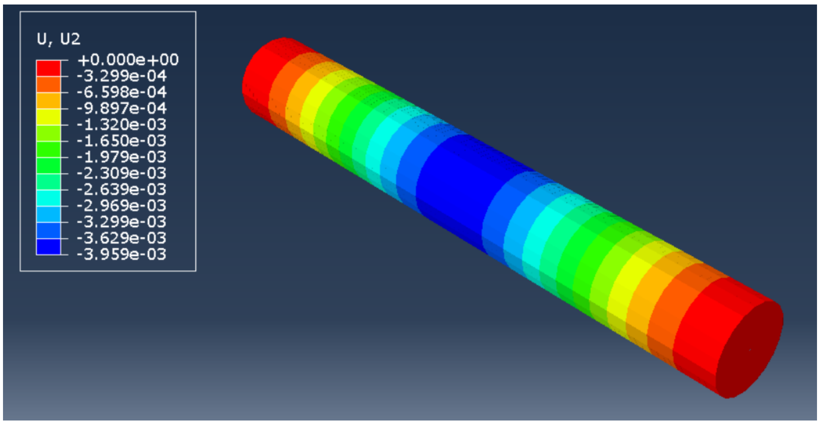

Figure 3.5: Resulting plot of the part by considering a wire base feature with a generalized profile shape.

Having analysed and compared the observable results in the contour plots with the calculated vertical displacement, it is clearly evident that modelling with the wire base feature considering a generalized shaped profile containing the accessible geometric characteristics of the real part presents the lowest relative error (49%) and when a box shaped profile is considered the given relative error is 111.59%. Even though the box profile is the most similar out of the two in shape to the actual aluminium profile, the fact that it is hollow on the inside may be the reason for the discrepancy in the results obtained. The possibility of modelling with solid elements was quickly discarded, not only as it would have been difficult to assemble all the different members of the structure, but also because of the substantially large amount of time it would have taken to complete the simulation and because of the high disparity between deflection values. However, it was decided to model the bridge in box beam shaped profiles as they resemble more strongly the actual profile of the bridge.

The next logical step was to study the behaviour of the modelled structure to static loads concentrated at the nodes of the central floor beams. Several simulations were performed with progressively greater loads to understand which elements would be in compression or tension, registering the values of deformation and vertical displacement with the main objective of achieving results that could be measurable in a real application. These studies were carried out considering one of the end floor beams simply supported and the other double supported. Bridges with the same dimensions and style but with a different number of modules (triangles) were also evaluated to understand the major differences between them and whether it would be advantageous to adopt one of them for the final model. Since increasing the number of modules increases the number of nodes and decreases the height of the structure, and considering that the length, width and load applied to the central nodes remain constant, a greater deflection is observed the more modules are added.

After a series of tests, it was concluded that the dimensions chosen for the bridge resulted in a very rigid structure whose vertical displacement and resulting deformations, for considerably high loads applied at the central nodes, were too low to be able to measure interesting values.

Still keeping in mind the main goal of achieving measurable values, the decision was made to change the design of the side of the structure to try to achieve a slightly more flexible solution. Altering the dimensions of the structure was also considered, specifically increasing the length and/or width, however, for practical reasons it was decided to keep the original configuration and just try to improve its design. As a source of inspiration, the new pedestrian bridge present in the recently inaugurated Parque da Asprela in Porto served as a major influence, and a similar style to this structure was adopted, not only in the arrangement of the lateral members, but also in the addition of a diagonal floor beam in each section of the deck (see Figure 3.6). The triangles making up the modules were changed from equilateral ones to scalene.

Figure 3.6: Picture of the pedestrian bridge in Parque da Asprela.

In Figure 3.7 the model made in ABAQUS with the dimensions and final configuration adopted without the visual representation of the chosen (box) beam profile is showed. The width of the bridge was modelled with a length of 960*mm* instead of 1000*mm* to compensate for the 20*mm* cross-sectional side length of the real aluminum profiles on either side. When designing the orientation of the members that form each triangle, it was preferred to have angles multiple of 10, since it was believed that, at the construction stage, this option would contribute to the desired simplicity of the assembly process. However, due to geometric requirements, this could not be fulfilled. The technical drawing with the dimensions of the design adopted for the side of the structure is shown in Figure 3.8.

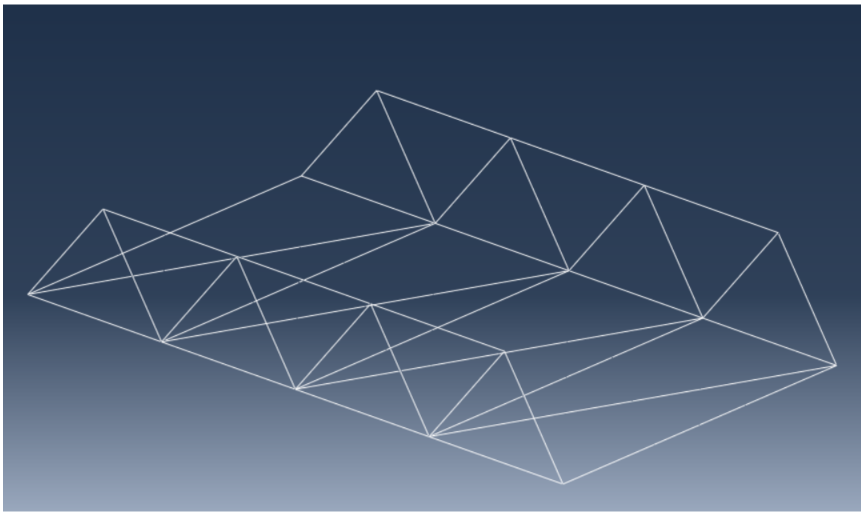

Figure 3.7: Final bridge model.

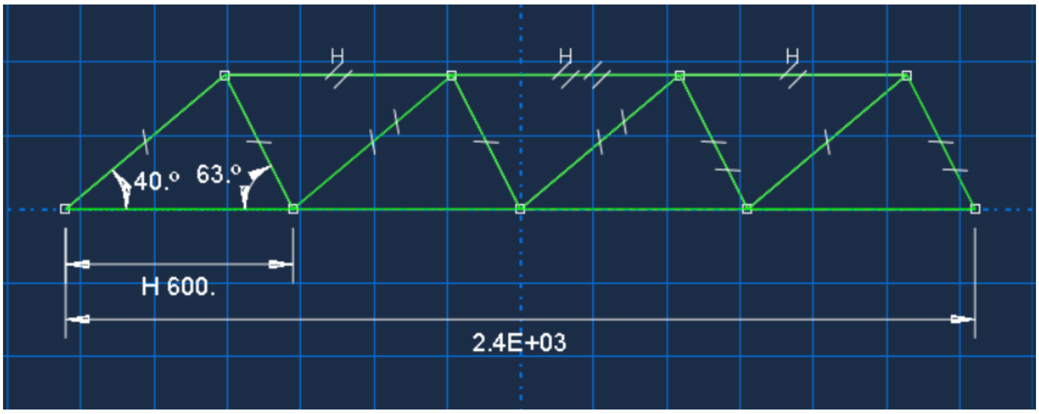

Figure 3.8: Two-dimensional sketch of the side of the bridge.

In order to prove the reliability of the designed model, the feasibility of carrying out load tests on the already instrumented structure was studied. These tests consist of statically loading the bridge in one or more well-defined locations with equally specified loads and analysing whether its behaviour was well predicted by the model. Through prior simulation of the tests to be carried out by numerical methods, it is possible to determine the most critical areas to be instrumented with strain gauges and the strain values that the sensors should provide at the time of testing. The available weights were $10kg$ each, so each simulation was submitted by applying loads of multiple values of 10.

One aspect that is quite easy to observe from the images presented and is supported by what was mentioned at the beginning of the chapter, specifically in the section on the characterisation of truss bridges, is the fact that the connections between profiles were assumed to be pin-connected, i.e., in contact at a single point. Now this is not entirely true in a real application, since it is impossible to connect more than two elements to the same point and trying to blindly build the structure without paying attention to this phenomenon would be irresponsible, to say the least.

Therefore, a careful and meticulous modelling with the real geometry of the profiles to be utilised was elaborated in SOLIDWORKS, with a special focus on the connections between members. Firstly, it was thought sensible to create a list with the different types of connections existing in the structure, according to the number of profiles that are in contact and their description, as well as in what quantity these connections are repeated. Once all the joints have been differentiated and established, the assembly process becomes more expedient and allows for the determination of which parts or methods should be used to effectively connect the members. The list just mentioned is displayed below in Table 3.1.

Table 3.1: Identification and description of connections within the structure.

Quantity	Nº Connecting Profiles	Description
10	4	Connection between longitudinal members and triangle inclined members
8	3	Connection of floor diagonal member with frame
8	2	Connection between longitudinal and lateral floor members
2	3	Upper corner connection
2	3	Upper corner connection
2	2	Floor corner connection
2	2	Floor corner connection

Since the chosen aluminum profile has a slot with a gap of 6*mm*, for the right-angled connections between longitudinal and lateral floor members, it was decided to have the angle brackets available in the supplier's catalogue (see Appendix B.1) as they can withstand greater loads than the other connectors. These are supplied together with the appropriate fixing accessories, these being M4 screws and M4 T-nuts, the latter being produced with the intention of being inside the profile's slot (see Appendix B.2). For all the other remaining connections, having gusset plates linking the profiles with each other seemed to be the most logical and only option to take. Gusset plates are commonly used to transfer stresses between connected members and aid in strengthening the joint, triangular or rectangular shaped and are fastened to beams with the use of rivets, bolts and even welding. For the present case, six different aluminium sheet gusset plates where designed with two holes assigned in the direction of each profile so they can be fastened together with the help of bolts, washers and t-nuts, also with a nominal diameter of 4*mm*. The design of the plates was inspired by an already existing one that was found on an online Bosch Rexroth CAD file database. The chosen material was also aluminium since the material sheet was already in stock. All the plates' technical drawings are available in Appendix B.3. Having all these components established, it was then possible to proceed to the finalization of the modeling in which the perception of the bridge closer to reality is obtained, and in Figures 3.9 - 3.10 some of the view orientations of the final structure can be found.

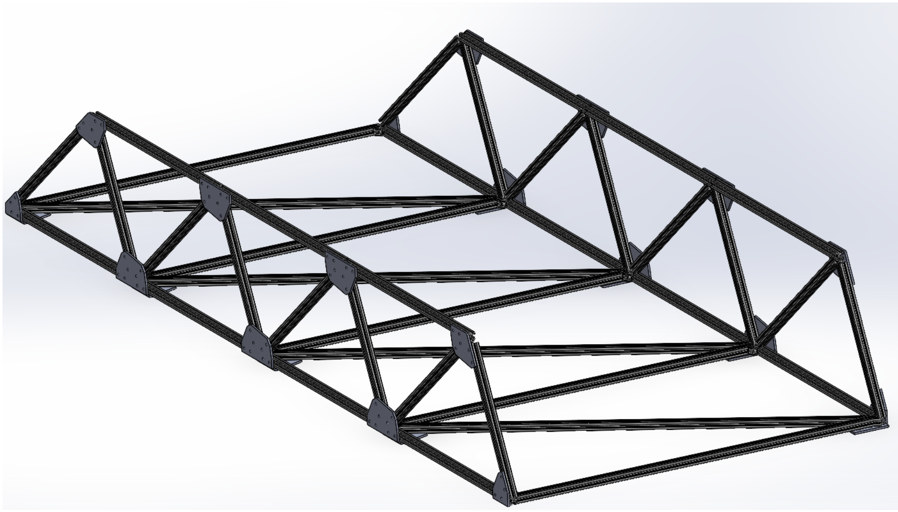

Figure 3.9: Three-dimensional isometric representation of the bridge.

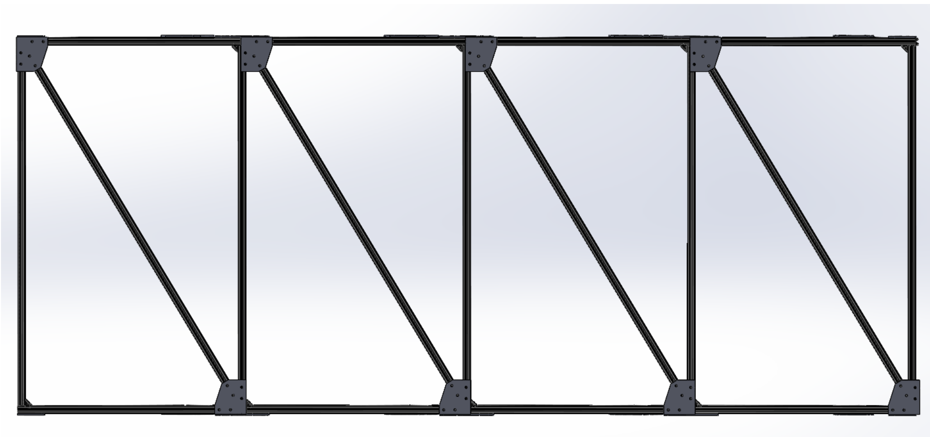

Figure 3.10: Bottom view orientation of the bridge.

3.3 Construction phase

Once the conceived design was accepted, the assembly sequence of all the elements of the structure was planned with the aim of coming up with a solution that would allow for greater efficiency in terms of construction and time management. Given the considerable size of the bridge, it was imperative to speed up the construction process in order not to disrupt or impede the normal operation of the laboratory, without compromising structural integrity. Additionally, the parts that were in storage and could be used in the project were studied, as well as those that would need to be ordered from the supplier. The screws, washers, and some M4 t-nuts needed for fixing the plates, as well as the aluminum sheet from which the gusset plates were to be cut and machined, were the only parts of the structure that were not ordered. With the goal of spending as less money as possible on ordering the required parts, and knowing that since there are profiles of variable length and shape in the structure, whose cutting involves an extra expense, the possibility of making most of the cutting with the help of the means available in the laboratory was evaluated. To aid the cutting process a list was prepared of the different lengths of the existing bridge members and their quantity (see Table 3.2). It should be noted that some values were overestimated to compensate for the cuts of the profiles made in planes other than the main ones. Table 3.3 shows the length and quantity of the profiles to be ordered, these being combinations of the values shown in Table 3.3, to later be split. The eight angle brackets and the missing t-nuts were also ordered.

Table 3.2: List of different existing members lengths to be ordered.

Length	373	506	600	960	1200
Quantity	8	8	14	5	4

Table 3.3: Calculated combinations of profiles to be cut.

Total Length	**Quantity**	**Combinations**
1200	11	600*14+1200*4
1518	2	506*3
1706	4	960+373*2
1972	1	960+506*2

While the order was being processed and the delivery date was not approaching, work started on obtaining the desired gusset plates. To do so, the rectangular outline of each of the plates was first outlined on the aluminium sheets available, after considering the distribution that would result in the least amount of wasted material. It is important to highlight the fact that the thickness of the two aluminum sheets supplied were not identical, so it had to be decided which sheets would end up having a smaller or larger thickness. The decision was made to make a rectangular outline rather than the original geometry for simplicity's sake and due to the capacity and availability of the existing machines at the lab's facilities to make the required cuts. Figure 3.11 and 3.12 show the contours outlined in the two available sheets.

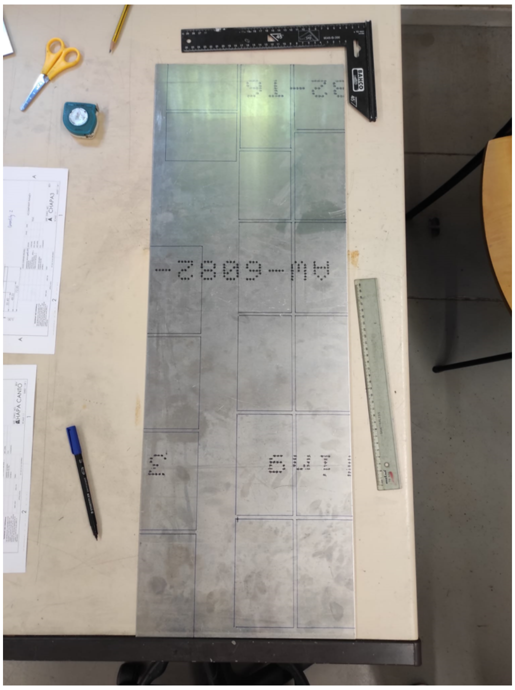

Figure 3.11: Gusset plates’ contours made on the thicker aluminium sheet.

Figure 3.12: Gusset plates’ contours made on the thinner aluminium sheet.

The two sheets were then forwarded to the most appropriate machine to carry out the cutting process, this being the hydraulic metal guillotine existing in the workshop of INEGI (Institute of Science and Innovation in Mechanical Engineering and Industrial Engineering), a science and research institute operating in partnership with the faculty. The operator starts the machine, positions the work piece in the cutting location and by means of a foot pedal operates the rams and the blade at a nominal pressure of $45kg/mm^2$ in a downward movement, performing the desired cut. He does not follow the contours made on the plate, since the machine produces straight cuts with excellent precision, being only necessary to know the dimensions of the plates to be obtained. The guillotine available was the Guifil GHE-630 (see Figure 3.13) with a length of $3m$ and indicated to cut metal sheets with a thickness of $6mm$ or less, being perfect for the cutting of the aluminium sheets.

Figure 3.13: Guifil GHE-630 hydraulic metal guillotine.

Once all the sheets were cut and delivered to the laboratory, the next step was to drill them for subsequent bolting. Before any drilling operation it is first necessary to make a hole or centering dent in the places intended for the holes to prevent the drill from slipping and drilling in the wrong place or damaging the tool. To this end, an automatic manual centring punch was used. As the required number of markings to be made was considerably high, the most efficient way of making them had to be found with the available material. It was decided to print the technical drawings of the plates and cut out the rectangular outline of the front view and, with the help of simple rubber bands and a paper clip, the paper was fixed to the plate and the punching operation was performed over the hole dimensions. An example of the set-up arranged for punching the plates in the correct places is shown in Figure 3.14. The whole process was relatively straightforward and did not take a substantial amount of time to finish, which clearly is beneficial since it was intended to have all the plates ready before the order arrived.

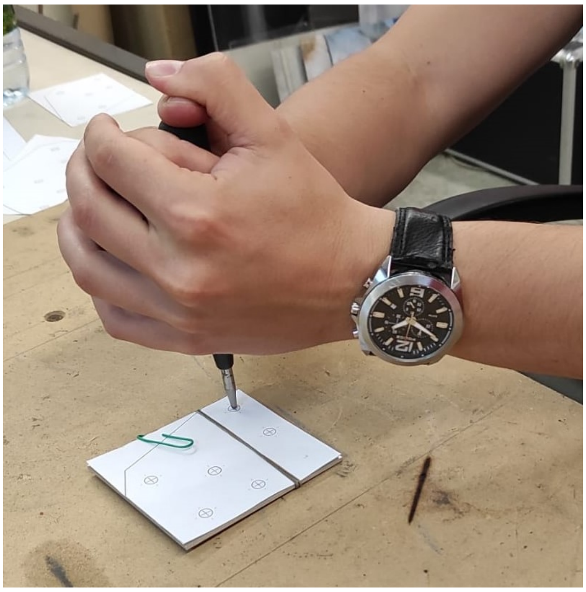

Figure 3.14: Centering punch process showing the fixation method of the drawing to the aluminium plate.

Following, the drilling itself could be carried out by the proper equipment, this being a bench mounted drill press machine. The available drill was the Dinamix 13mm drill press (see Figure 3.15) with a voltage of 220V and 1300rpm, and due to the drill chuck that supports drill bits up to 13mm in diameter, it is perfectly suited to drill the intended through holes of 4mm in diameter. After having been briefed on how the drilling machine works by the laboratory coordinator, the drilling process began autonomously and was completed in a relatively short amount of time, as the plates, being made of aluminium, offered no great resistance to the forward movement of the drill bit.

Figure 3.15: Dinamix 13mm drill pressing machine.

In the meantime, the material ordered was finally delivered and the cuts of the profiles mentioned above were made immediately. The tool available for the purpose was the GTM 12 JL Professional combination saw from Bosch, mounted on the GTA 2600 Professional workbench also marketed by Bosch, installed in INEGI's workshop. The first cuts were made with the help and supervision of the responsible of that area, having then been allowed the free use of the tool. Figure 3.16 shows the above mentioned equipment.

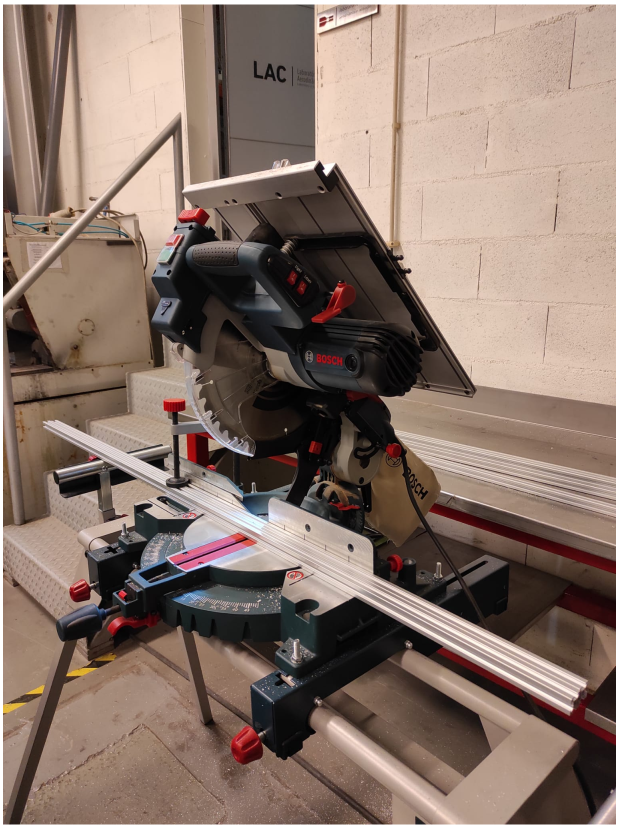

Figure 3.16: GTM 12 JL Professional saw mounted on GTA 2600 Professional workbench.

The first section of the structure to be built was the bridge slab, more specifically the entire frame without the diagonal bars. This sequence was chosen because, as the diagonal members would have to be cut in directions other than the main ones, with all the longitudinal and lateral floor profiles already assembled, it would be easier to accurately mark the diagonals for subsequent cutting. In Figure 3.17 shows one of the bridge deck modules assembled. When the assembly of the floor frame was completed, it was noticed that two of the diagonal members had been incorrectly sawn and were relatively shorter than originally assumed. This was probably due to possible careless marking or misalignment of the profiles on the saw supports, but the construction process was nevertheless maintained. The structure at this point was quite unstable and flexible, obtaining a vertical displacement of $5cm$ only due to its own weight when it was simply supported on two chairs at the ends.

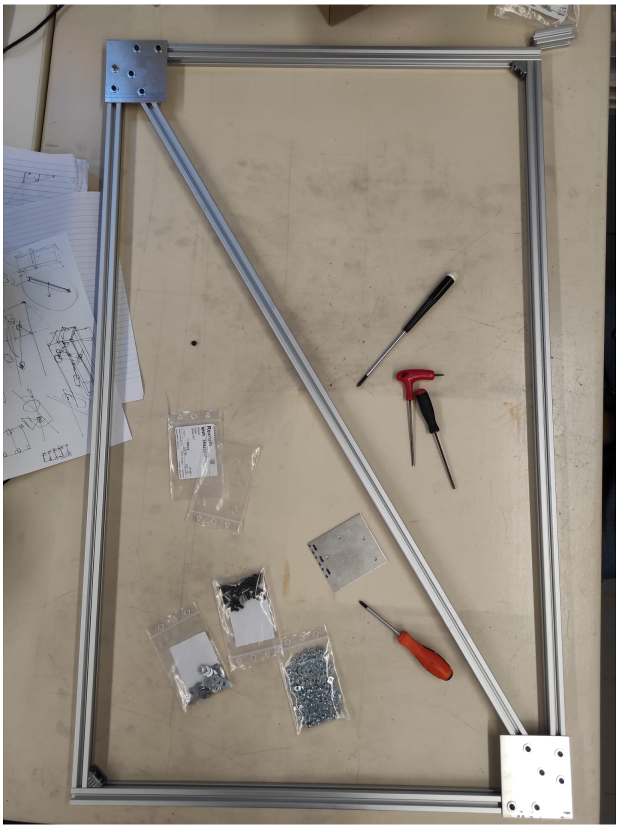

Figure 3.17: Finalised assembly of one of the bridge' deck's modules.

The plates connecting the longitudinal members and the side frames were then fastened and the assembly of one side of the bridge began. First, the top longitudinal profiles were properly aligned and screwed to the corresponding plates and, consequently, the inclined members constituting each module were also connected. In this phase, it was necessary to cut the inclined members so that when assembled with the deck of the bridge, the resulting height would coincide with the value obtained in the SolidWorks model. In order to accomplish this, all the profiles that surpassed this value were marked with a permanent ink pen, and after a careful removal, the excess was cut in the saw. These members were again joined to the side frame and this whole process was repeated on the opposite side of the bridge, after which the whole structure could finally be assembled. The difference once the build was completed, compared to the preliminary test made, considering only the deck frame, is notorious and shows just how important a lateral truss structure is in terms of rigidity and stability in the entirety of the bridge.

Chapter 4

Testing and result discussion

In this chapter, all the numerical and experimental analysis of the developed structure is presented. In the first instance, a preliminary test to the bridge is detailed and performed, and the subsequent review of the results is discussed. Then, after the appropriate instrumentation of the structure, whose procedure is also described, the load tests mentioned in the previous chapter are conducted and its results are evaluated and compared to the numerical model.

4.1 Preliminary evaluation

In order to determine if the stiffness obtained had been well achieved in the construction in terms of similarity with the numerical model considered, four vertical displacement measurements were made at one of the central nodes of the structure with progressively higher loads. Two digital comparators were placed on each side of the gusset plate to obtain two experimental results in each of the measurements, considering as final value the average of both. These devices are generally used when linear displacements are to be measured, and measure the difference based on a reference position that can be set by the user. The available loads were lead disks weighing $100N$ each, and due to their considerable size (about $25cm$ in diameter) it was not possible to load the bridge exactly at the nodes. The test consisted on placing a disk as close as possible to the central nodes, recording the measured value on the display of both comparators, and repeating the process until eight disks were loading the structure simultaneously, thus having a total load of $800N$. Figure 4.1 shows the last measurement taken during the described test, with the eight discs placed on the structure.

Figure 4.1: Real structure loaded by the eight lead disks at the central nodes.

As previously mentioned, the value considered for the measurement of the real deflection for each static load resulted from the average of the values of both comparators, so it was decided to present only the single final result. The comparators used were the Mitutoyo Digimatic Indicator 543-250B standard type. These measurements are presented in tabular form below (see Table 4.1).

Table 4.1: Obtained values for the real defletion.

Force (N)	**Real Deflection (mm)**
0	0.0000
200	0.2180
400	0.4545
600	0.6965
800	0.9950

As one can concluded, the vertical displacement for a load of about $80kg$ is a little less than a millimetre, which at first seems quite appreciable. However, it is necessary to confirm if this deflection value is close to the one obtained from the numerical model and if it follows the construction standards imposed for metallic structures. The standards adopted were ABNT NBR 8800:2008 - Design of steel and composite structures for buildings and AISE TR 13 - Guide for the Design and Construction of Mill Buildings - 2003. These two standards dictate that for the type of structure that has been developed in this project, the maximum deflection value allowed in service V is given by Equation 4.1, in which L is the length of the bridge in centimeters.

$$V <= \frac{L}{600} = \frac{240}{600} = 0.4cm = 4mm \tag{4.1}$$

According to the standards followed, the obtained deflection is within the stipulated interval, thus being within the imposed standards. However, applying a safety coefficient equal to 1.35, recommended for steel bridges, a value for the deflection of 2.96*mm* is obtained, which still corroborates the value of the measurements performed. Additionally, it was found interesting and most importantly to determine, approximately, which load would result in the theoretical collapse of the structure, i.e., which load on the bridge would give rise to a vertical displacement of 2.96*mm*. Through a simple rule of three by using the values from the last measurement, a maximum allowable load of 2379*N* is obtained and this was then simulated to verify its accuracy. The following figures (Figure 4.2 and Figure 4.3) show the plots obtained from the numerical model for the deflection values by the action of static loads at the central nodes corresponding to 400*N* and 1190*N*, respectively.

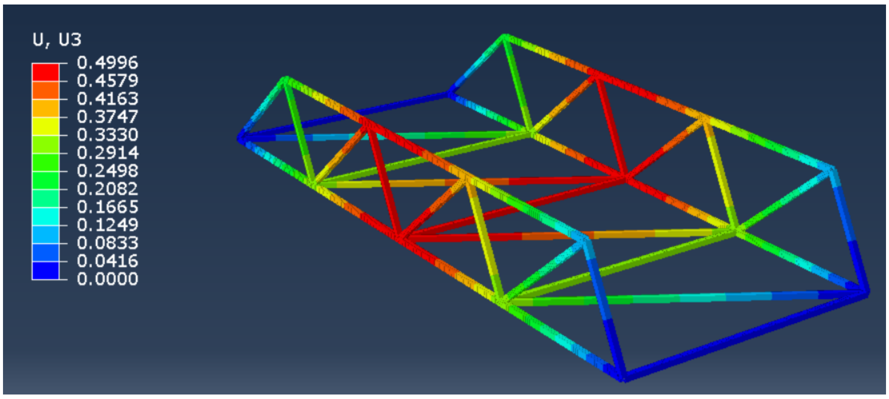

Figure 4.2: Resulting plot when a static load of 400 N is applied in each central node.

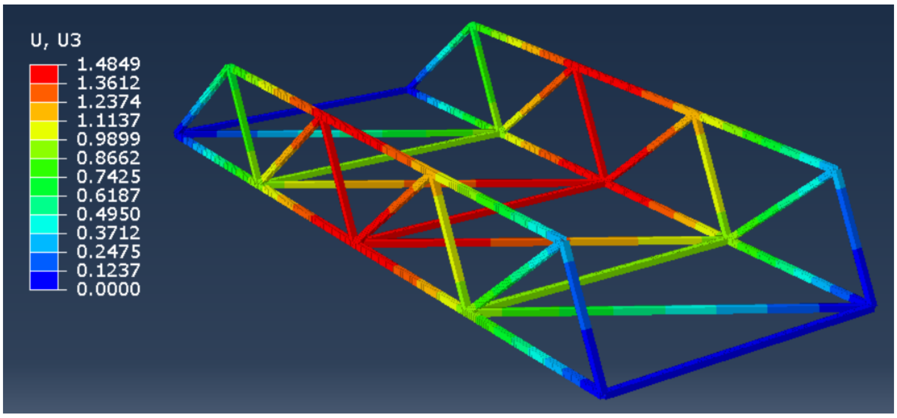

Figure 4.3: Resulting plot when a static load of 1190 N is applied in each central node.

The results show a significant variation from the expected values with a relative error in the region of 100%.

4.2 Instrumentation

A constant obstacle in the implementation of structural monitoring techniques is identifying which areas of the structure are most subject to damage and which parameters should be monitored.

Since the present project is concerned with monitoring the structural integrity of the bridge, it was decided to simulate the load tests that will be carried out in order to determine in advance and with precision the critical areas in terms of strain. This way, it is possible to study the configuration of sensors and cables that best suits the application in question

After analyzing the plots obtained, one can conclude that the members under the greatest stress are the upper central members, which have to bear the greatest compression load, and the lateral members near the central nodes. It is also possible to observe that the strain is more significant in the main direction along the x-axis. Given that the imposed loading is always symmetrical, i.e. the same number of discs are placed on each side of the bridge, it can be assumed that both sides of the structure behave equally. However, since the actual structure is on an irregular and uneven floor due to space availability issues, the decision was made to instrument and study the more easily accessible side. As strain is concerned, only the upper faces of the critical members will be instrumented, again, for accessibility reasons and because it was not considered extremely important and relevant to analyze the behavior of both sides of the profiles, since theoretically the deformation values would be symmetrical. However, in some applications, to ensure redundancy in measurements, symmetric-sided instrumentation may be justified, as it enables the characterization of loads whose position changes transversely.

Also recalling that any structure is in constant vibration, the installation of an accelerometer in a highly oscillatory location where the amplitude is maximum is of considerable importance and relevance for this project. Not only does this enable the amplitudes felt in the structure during the load tests to be obtained and stored, but through manipulation of the captured signal it is also possible to obtain the magnitude of these peaks in the frequency domain in order to visualize the natural frequencies of vibration of the bridge.

4.2.1 Strain gauge installation

Taking into account that the highest strain value was obtained in one of the main directions, it was decided to select unidirectional strain gauges and position them on the structure aligned in the desired direction. Motivated by monetary reasons, it was decided to allocate only one sensor per member and the strain gauges selected were the HBM 1-LY43-3/120 foil strain gauges. These are perfectly suited for aluminium applications and have a measuring grid made of constantan (a copper-nickel alloy), protected by a polyimide cover, a gauge factor of approximately 2 and also have higher sensitivity to lower frequencies

For the installation of any type of strain sensor, it is imperative to first prepare the surface so that the data provided by them are as correct as possible and are not compromised by anomalies when in contact with the face. In the case of a resistance sensor, as previously mentioned in Chapter 2, adhesion to the material is achieved via the application of an adhesive. However, before applying the adhesive, the surface first had to be sanded a little following a specific set of directions and then cleaned with a ammonia-based material to ensure it was smooth and had optimal conditions for bonding. Once the surface was completely treated, the sensor to be implemented was prepared, which consisted of cleaning and drying a mirrored surface with acetone, and then placing the gauge on it. Then, the instrumentation area is subjected to the application of a catalyst that allows a fast curing of the adhesive glue to be added, this being cyanoacrylate. As soon as it dried, the adhesive was introduced and with the help of a strip of tape, the sensor was moved from the mirror to the area with adhesive, and by applying thumb pressure for about a minute, good adhesion was assured. The described process was replicated for the installation of each of the three strain gauges and the final look of the installation is shown in Figure 4.4. More specifications regarding this particular gauge can be found in Appendix C.1.

Figure 4.4: Selected HBM 1-LY43-3/120 foil strain gauge installed in the upper central member.

The next step involves establishing the connection between the sensors and the acquisition system, the latter previously implemented in other similar monitoring systems by LOME. The available data acquisition system was the NI cDAQ-9188 equipped with 8 slots and an Ethernet connector, that also has timing resolution of $12ns$. This connection was made via electrical cables that also had to be prepared for the application at hand. The type of resistance strain gauge used has the particularity of allowing the direct soldering of cables in the sensor itself, presenting two channels for that purpose. For this reason, of the nine terminals at each end of the available cables, only three were used and two of these were interconnected, specifically the red and green terminals (see Figure 4.5). The tips were coated with tin to promote greater hardness and resistance through a soldering process with the aid of a soldering iron powered by Weller's WD1 soldering station power unit. The station's temperature was set to between 250 and 300 degrees Celsius, as the melting temperature of tin is about 230 degrees. The interconnected ends of the cable were then soldered to the right hand side channel of the gauge and the remaining terminal, the blue one, was connected to the left hand side channel (see Figure 4.6).

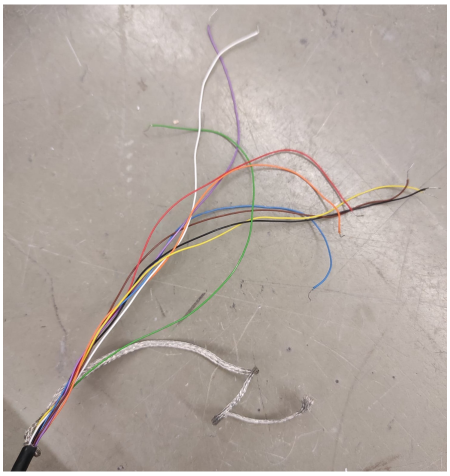

Figure 4.5: Close up view of one end of the cable.

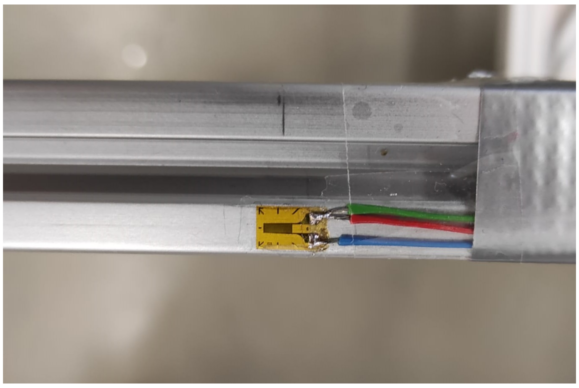

Figure 4.6: Installed strain gauge with the cables already soldered.

In order to avoid irrelevant and/or inaccurate information, the contact between the aluminium strip and the bridge is promoted to remove the effect of noise in the transmission of the signal obtained by the sensors and transmitted to the DAQ. The fact that the instrumented zones and the DAQ were close to each other, contributes to justify the choice of this type of sensors, because in that sense the signal produced by them is not so vulnerable to major interference. The data transmission from the acquisition system to the storage system and analysis software is done via cables, with the DAQ operating in polled mode. This means that while the system is being monitored, there will be uninterrupted data capture and storage, and it will also be possible to observe variations in the structure in real time. A fundamental parameter of the strain gauge is its sensitivity to strain, this being the gauge factor. The gauge factor is the proportionality factor between the relative change in resistance and the strain to be measured. This parameter exists in an attempt to minimize sensor sensitivity to temperature, by treating the gauge material to account for the thermal expansion of the target material for which the sensor is intended.

When setting up the cables in the acquisition system, it was necessary to number the connections so that the software could correctly identify the resistive variation of the strain gauges and match it to the right sensor. To do so, the gauge installed in the upper member was identified by the number 1 and the others, allocated to the lower profiles were identified with the numbers 2 and 3, as shown in Figure 4.7. Equally important to mention is that the DAQ extensometry module used for establishing the connections was the NI 9235 and the signal acquisition and analysis software implemented was SignalExpress from LabView.

Figure 4.7: Numerical identification of strain gauges.

4.2.2 Accelerometer installation

Considering that the bridge when loaded vertically will vibrate with greater intensity in this direction and that in order to obtain the true acceleration variation of the structure the sensor must be mounted directly on it, it was decided to install the accelerometer aligned with the vertical direction and laterally on the member that contains the strain gauge number 2. Since the PCB Piezotronics Series 356 Triaxial Accelerometer accelerometer was available and is designed to perform simultaneous measurements along three orthogonal axis in lightweight structures (due to its low weight) and suited for modal analysis, it was decided to implement it.

The selected sensor was mounted in the chosen location by means of a common adhesive, this being beeswax. Special care was taken to ensure that both the surface of the accelerometer intended for contact with the structure and on which the adhesive would be applied, and the area of the bridge that would serve as the contact surface, were thoroughly cleaned. This sensor requires cabling to emit and store the recorded signals. After the installation, one end of a fiber optic cable specially commercialized by PCB Piezotronics for accelerometers was connected to the sensor and the other end to the acquisition system. This latter end has three terminals each associated with one of the three axes, so it is necessary that the connections are correctly established to the respective terminal on the DAQ. Should one of the ends be accidentally misplaced, the measurements would be totally incorrect. In Figure 4.8 the mounted sensor with its corresponding cable connection is shown.

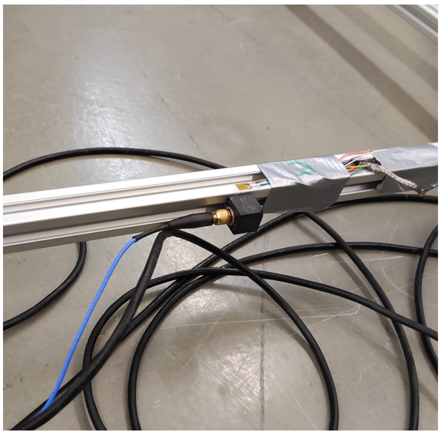

Figure 4.8: PCB Piezotronics accelerometer mounted on the structure.

The data acquisition system and the data processing and signal interrogation software used and discussed in the strain gauge installation section is the same for the analysis of the sensed accelerations with the particularity that the accelerometry module used was the NI 9234.

4.3 Experimental analysis

This section covers all the steps of the experimental tests carried out on the structure. The reason why each one was carried out is firstly highlighted along with the detailed presentation of the process to be conducted. Next, the contour plots obtained from the numerical simulation of the tests are presented, as well as the final product of the manipulation of the data provided by the sensors. Finally, the validity of these results is discussed.

4.3.1 Loading test 1

Evidently, the area of the structure that deflects the most or should deflect the most is the central zone. For this reason, it was decided to perform a test with the highest load available in the laboratory applied at the central nodes or as close as possible, to study the maximum strain values felt on the bridge, similarly to the preliminary test performed and detailed previously. The test will have a maximum load of 800N, divided by the two nodes located in the central part of the structure, with successive increments of 200N. Once the data processing software has started, the bridge is loaded with the first pair of discs and to allow the structure to stabilise, a time interval of a few seconds is set between loadings. This is repeated until the entire load is set on the bridge and only then was the software stopped.

Initially, a force of 400N was applied to each central node in the numerical model and the simulation of the experiment was run, obtaining the plot seen in Figure 4.9 for the unidirectional strain in the x-axis (E11). The boundary conditions considered were the ones that prevent the movement of the structure in the vertical axis and the whole process was fairly quick and simple to complete.

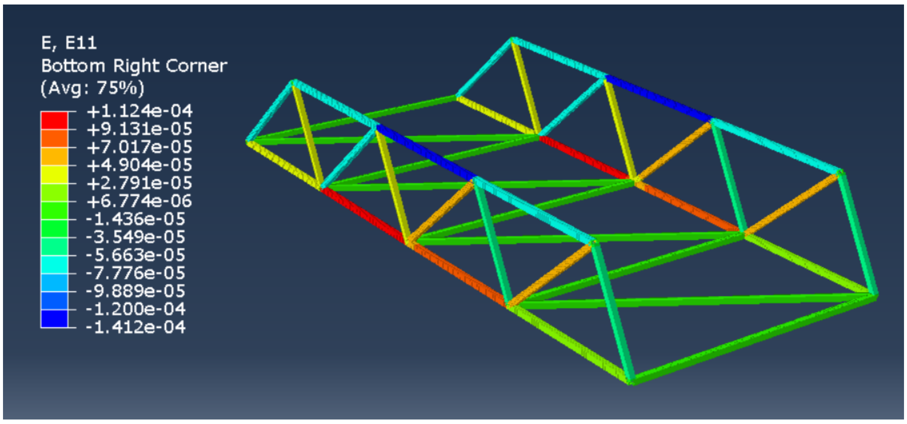

Figure 4.9: Resulting plot of the simulation run of the first loading test.

During the loading test, efforts were made to place the disks on the structure as carefully as possible and at the same time, because it was seen as advantageous in the later analysis of the results. The strain gauge readings were recorded as a function of test time and stored in a tabular form. However, to facilitate analysis and to effectively get a sense of how the sensors deform when loads are applied, the data was processed to be presented graphically, as shown in Figure 4.10.

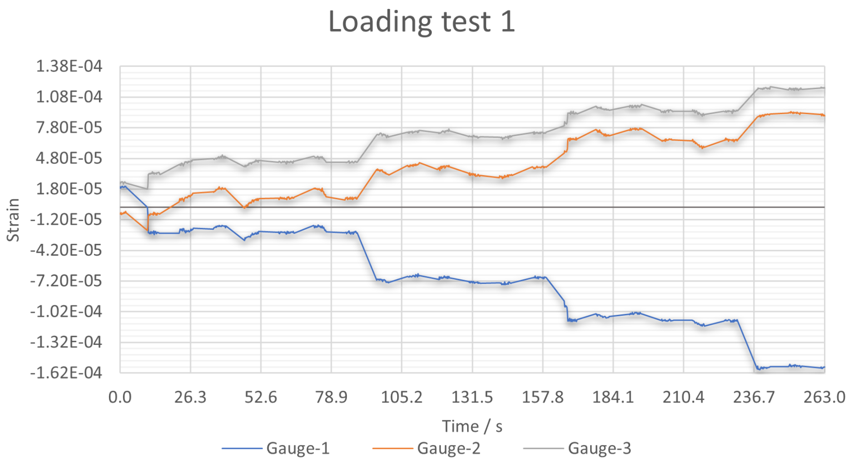

Figure 4.10: Graphic representation of the strain evolution with time, due to the load action in the first test.

Through the analysis of each of the trend lines of strain variation, four distinct levels can be observed, corresponding to the instance of the disks' placement. It is also evident that strain gauge number 1 shows a more noticeable flattening of the curve than the others and that the latter, although transmitting different strain values, their behaviour throughout the test was practically the same, which was somewhat predicted.

Analysing the colour scheme of the numerical model resulting from the test simulation, the member under greater traction stress is identified as the one in red and on which strain gauge number 3 is installed. Naturally, the strain values emitted by this sensor should be higher than those transmitted by strain gauge number 2. This was confirmed in the loading test, as the grey curve in the graph (StrainGauge-3) reaches higher ordinate values than the orange curve (StrainGauge-2).

Lastly, to firmly state that the test was well performed and that the results corroborate those expected, the maximum value felt by each strain gauge was studied and the relative error compared to the numerical model values are shown in Table 4.2.

Table 4.2: Comparison between loading test values and simulation results.

	Real Strain	**Modelled Strain**	**Relative error (%)**
Strain Gauge 1	-1.59E-04	-1.41E-04	12.37%
Strain Gauge 2	9.36E-05	9.13E-05	2.46%
Strain Gauge 3	1.18E-04	1.12E-04	5.18%

By examining Table 4.2, the first aspect that can be seen with relative ease is that the order of magnitude between the obtained and expected results is the same. Additionally, the compressive and tensile stresses, negative and positive strain values respectively, are in accordance with the numerical model. The obtained deviations in the results are relatively small to be considered acceptable, being strain gauge number 2 the one that gives the best approximation with a relative error of just 2.46%.

4.3.2 Loading test 2

In the second load test, the aim was to check whether in fact the structure would deform more severely with all the load applied in the central area, so it was decided to distribute the weight over all the nodes of the floor frame. At the central nodes, instead of the previous 800*N* applied, only four discs were placed in total, two on each side. The remaining four weights were spread over the nodes adjacent to the central ones, having each node loaded with a disk. The methodology of the previous test was followed, maintaining the care in the positioning instant of the loads and the temporal spacing between phases. The boundary conditions remained unchanged, having only redone the application of loads in the model. The first loading stage was to place the fours disks at the nodes next to the central ones simultaneously and then, again with increments of 200*N* loads were applied in the middle nodes. The resulting contour plot from ABAQUS regarding the unidirectional strain in the x direction is given in Figure 4.11 and the graphical representation of the transmitted strain values from the gauges is shown in Figure 4.12.

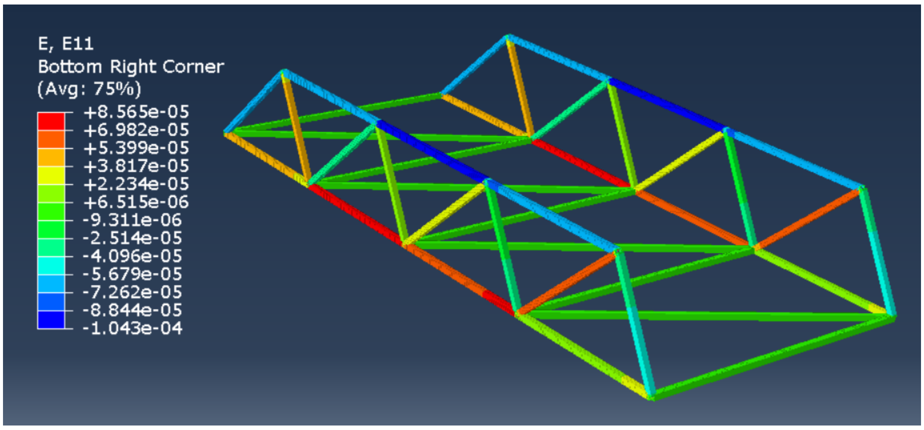

Figure 4.11: Resulting plot of the simulation run of the second loading test.

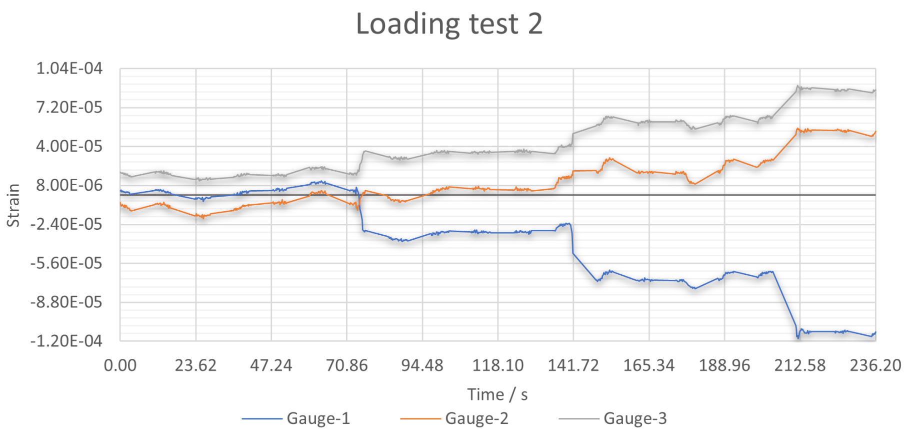

Figure 4.12: Graphic representation of the strain evolution with time, due to the load action in the second test.

By analysing the two figures, it can once again be verified that the colour scheme resulting from the simulation indicating which members are under the most stress is in agreement with the results obtained from the load test. Strain gauge number 1 recorded the highest strain value among the three, and the strain gauge mounted on the orange profile (strain gauge number 2) emitted the signal corresponding to the lowest tensile stress value.

What is also interesting is that, contrary to the previously mentioned test in which there were four positioning phases for the weights, in this test there were three loading phases, since in the first step four discs were placed. For each loading stage, a plateau is observed in the strain curves to which the values recorded by the strain gauge will tend.

Moreover, the similarities between the evolution of the signals emitted by the strain gauges installed on the lower limbs can still be verified. Just like the previous experiment, it was considered appealing to represent the data graphically (see Table 4.3).

Table 4.3: Comparison between loading test values and simulation results.

	Real Strain	Modelled Strain	Relative error (%)
Strain Gauge 1	-1.18E-04	-1.04E-04	13.15%
Strain Gauge 2	5.49E-05	6.98E-05	21.38%
Strain Gauge 3	9.02E-05	8.57E-05	5.33%

Once again, the orders of magnitude of the measured strains coincide with the numerical model, with the sensor installed in the member under the greatest traction load the one that presents the closest approximation. Further analyzing Table 4.3, one may come to the conclusion that the relative error associated with strain gauge number 2 may be related to a slight tendency to place the disks closer to the profile that contains the said sensor.

4.3.3 Loading test 3

The purpose of this test was to analyze the evolution of strain not only during the various loading steps with the weights, but also with the successive relief of the forces exerted on the structure. Thus, it was decided to repeat the entire procedure introduced in the execution of the first loading test, with the particularity that the test would continue until the bridge was free from the action of the disks. The disks were removed with immense care and temporally spaced out, with increments of 200N. Since the numerical simulation has already been run when the first loading test was performed, the resulting plot will not be presented again. Nevertheless, the graph of the strain variation recorded by the sensors over the test time is shown in Figure 4.13.

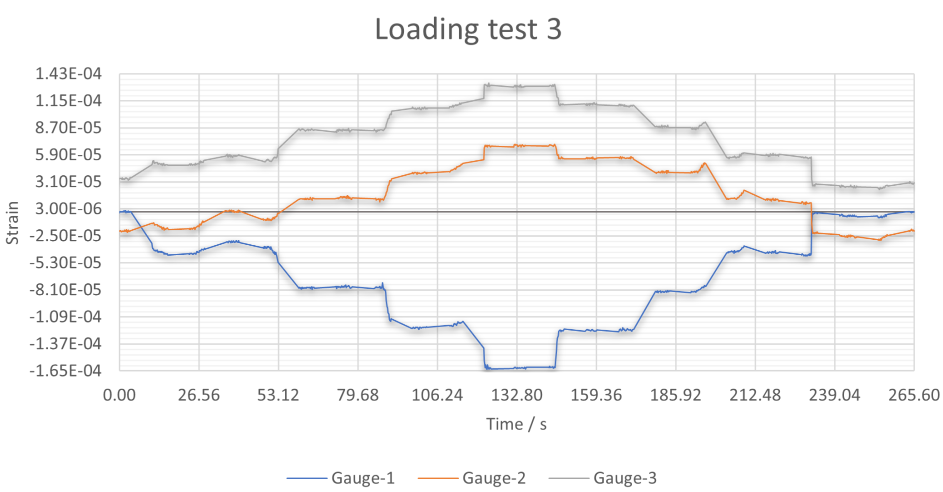

Figure 4.13: Graphic representation of the strain evolution with time, due to the load action in the third test.

In Figure 4.13 , one can easily identify all the steps of the test under discussion by the clear existence of the already mentioned plateaus. Also evident is the continuous pattern correlation between the two bottom extensometers, even in situations of unexpectedly high oscillation, as in the case of the lifting of the second pair of discs, around 200*s*. The evolution of strain values seems slightly more oscillating when compared to that shown in Figure 4.10, particularly at the load placement instants.

As expected, the maximum strain values felt by each gauge were once more listed and compared with the expected strain values obtained from the numerical model (see Table 4.4). Additionally, since the test proceeded until all weights were removed, it was considered interesting to highlight the initial and final values recorded by the sensors in Table 4.5, with the absolute error between the mentioned measurements also included.

Table 4.4: Comparison between loading test values and simulation results.

	Real Strain	**Modelled Strain**	**Relative error (%)**
Strain Gauge 1	-1.63E-04	-1.41E-04	15.73%
Strain Gauge 2	7.01E-05	9.13E-05	23.25%
Strain Gauge 3	1.34E-04	1.12E-04	18.88%

Table 4.5: Comparison of the initial value with the final value of the loading test carried out.

	Initial Strain	**Final Strain**	**Absolute error**
Strain Gauge 1	-9.05E-07	-2.48E-07	6.57E-07
Strain Gauge 2	-2.05E-05	-1.98E-05	7.01E-07
Strain Gauge 3	3.43E-05	3.02E-05	4.09E-06

In Table 4.4 and taking into account the tests already discussed, it is evident that this was the test that generated the most differentiation between results. Although the orders of magnitude and the positive and negative symbols of the signals emitted by the sensors follow what was expected, there may have been some accidental impact against the structure during the test that caused these disparities. What is also curious is the fact that the sensors did not return to the initial strain value as shown in Table 4.5.

4.3.4 Impact test 1

Knowing that the natural mode of vibration of a given mechanical system or structure depends on its mechanical properties, thus being an intrinsic property, and that it is represented by the movement in which all degrees of freedom perform the movement of identical frequency and respective amplitude, performing a modal analysis over the duration of the approached load tests would not make much practical sense. So, in order to identify the natural frequencies of the bridge, it was decided to perform an impact test without any external loads and then converts the signal obtained by the accelerometer with the Fast Fourier Transform (FFT) technique, which converts the signal to the frequency domain.

In dynamic analysis, one of the most difficult aspects to achieve is to obtain repeatability of results due to the strong possibility of not managing to keep the solicitation conditions exactly the same, since a small variation may result in the invalidation of the test. To counter such a hypothesis, three tests of equal duration and equal initial conditions were performed, with the impact applied at the central node of the uninstrumented bridge side and with relative low magnitude.

Firstly, a prediction calculation was performed, to estimate between which values the natural frequencies will lie or of what values will it be close to. Recalling the formula for the undamped natural frequency of vibration, it requires the knowledge of the stiffness constant of the bridge and its total mass. Since a preliminary vertical displacement test was performed with a load of $800N$, obtaining a deflection of $0.9950mm$, the stiffness constant k is easily calculated by Equation 4.2.

$$k = \frac{P}{\delta} = \frac{800}{0.9950 \times 10^{-3}} = 804020N/m \tag{4.2}$$

Taking into consideration the information presented in Table 3.2 regarding the length of the profiles that were ordered, the total length of the members in the structure is obtained which multiplied by its weight per meter, results in the total mass value of the profiles of $10.0128kg$. Approximating the weight of all other bridge components (gusset plates, angle brackets, bolts, washers and T-nuts), the total mass of the structure is approximately $13.2984kg$, however $14kg$ is assumed. Finally, the natural frequency can be calculated by Equation 4.3.

$$\omega = \sqrt{\frac{k}{m}} = \sqrt{\frac{804020}{14}} = 38.1408Hz \tag{4.3}$$

What can also be done to further increase the chances of accurately estimating the natural frequency is to perform modal analysis on the numerical model of the bridge. The first 15 natural frequencies of vibration of the model with no applied loads are listed in Table 4.6, having maintained the boundary conditions of the loading tests. Since the first vibration mode features a null frequency, presumably due to the rigid body movement performed by the structure, it was decided to present the value referring to the sixteenth natural frequency.

Table 4.6: Obtained natural frequency values from the numerical model.

Modes	Natural Frequency (Hz)	Modes	Natural Frequency (Hz)
1	0.000	9	85.376
2	34.107	10	86.905
3	52.174	11	88.401
4	55.250	12	91.035
5	58.391	13	91.705
6	79.618	14	93.855
7	81.767	15	97.812
8	83.416	16	104.72

Through the analysis of Table 4.6, the first natural frequency is $34.107Hz$, slightly lower than the calculated value. Thus is deduced that the first true vibration mode will vibrate at around $36Hz$.

All that remains is to effectively conduct the impact tests and assess whether the probable values presented earlier are in fact accurate.

The tests were performed with extreme care to ensure that the results were reliable, with 30 seconds intervals between runs to allow the structure to stabilize. The impact was done with a small cleaning brush to prevent high shocks that could lead to signal saturation. By enabling a common feature the signal interrogation software (SignalExpress) makes it possible to visualize the magnitude results as a function of both time and frequency. In the following figures, the plots from the first test are displayed, as well as graphs in the frequency domain for all tests scaled to $[0,100]Hz$. The remaining figures can be found in Appendix D.1.

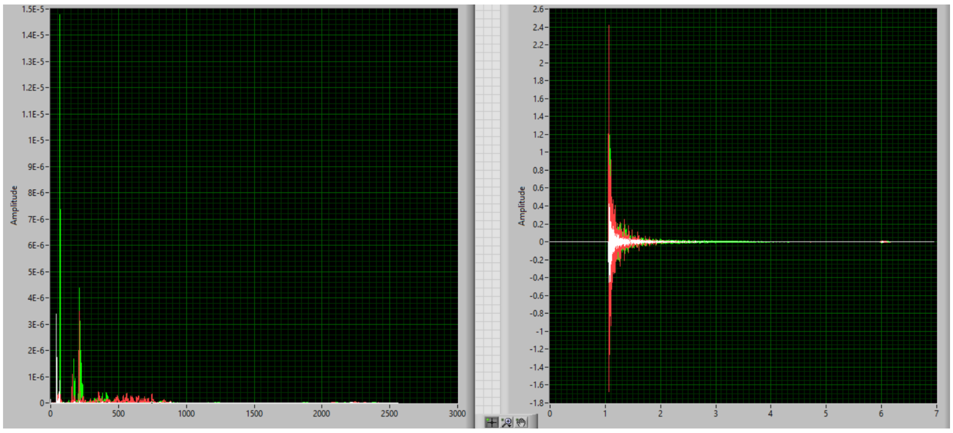

Figure 4.14: Graphical representation of the impact response amplitude of the first test as a function of frequency (left) and time (right).

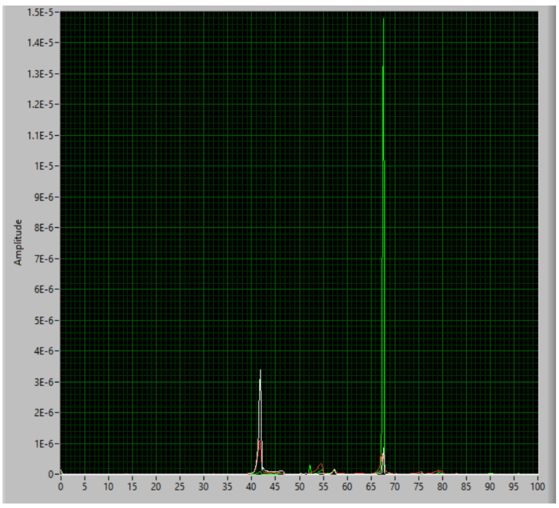

Figure 4.15: Graphical representation of the impact response amplitude of the first test as a function of frequency up to $100Hz$.

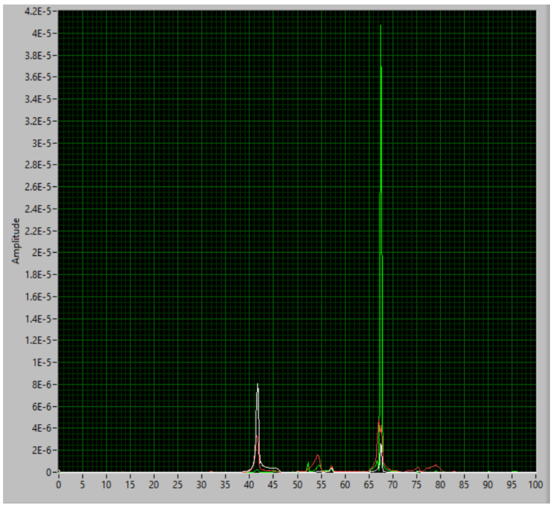

Figure 4.16: Graphical representation of the impact response amplitude of the second test as a function of frequency up to $100Hz$.

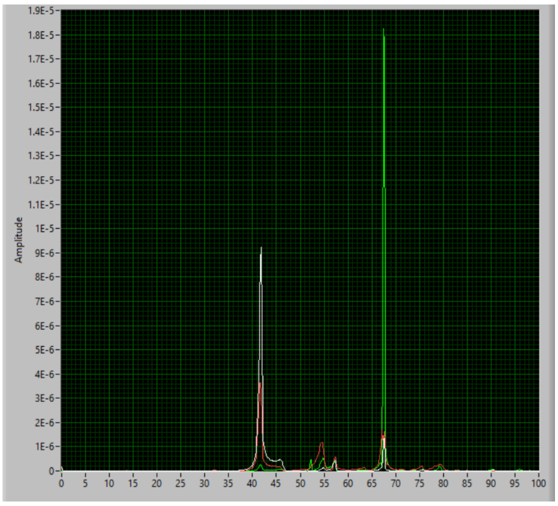

Figure 4.17: Graphical representation of the impact response amplitude of the third test as a function of frequency up to $100Hz$.

In the three scaled figures it is easily observed well-defined peaks at the frequencies of $41.5Hz$ (assumed to be the first natural frequency) and $67.5Hz$, as well as some not so clearly noticeable peaks at $52.5Hz$, $54.5Hz$, $57.5Hz$, $75Hz$ and $79Hz$. The difference between the predicted results and the real natural frequency value may be due to a series of factors, one of them being the fact that the total mass of the structure was over-approximated, thus lowering the value of the natural frequency. Another possible reason may lie in the inaccuracy of the center deflection measurement caused by the loading of the disks which resulted in a stiffness constant that could be considerably lower than it actually is.

4.3.5 Impact test 2

In order to prove the reliability of the acquisition system, the signal integration software, and the sensor itself, it was decided to perform another impact test similar to the previous one, with the particularity that in this case the test would be carried out with the bridge fully loaded. Since the mass of the structure is being increased by about 5 times, a shift of the natural frequencies to lower values for the same stiffness constant is expected. The loads were again applied with the eight lead discs, placing half on each central node as gently as possible and simultaneously. After loading, a roller hockey ball was dropped on top of the weights on the side of the bridge without any sensory installation, from a height of about $60cm$. Once more, the test consisted on three trial runs.

Much like the previous test, a prediction calculation of the new natural frequency can be performed considering the mass applied to the structure, as well as identifying the frequency values associated with the respective natural modes from the numerical model. Assuming that the stiffness constant is unchanged, the natural frequency is obtained from Equation 4.4.

$$\omega = \sqrt{\frac{k}{m}} = \sqrt{\frac{804020}{14+80}} = 14.719Hz \tag{4.4}$$

Then, efforts were made to try to apply the mass of the weights at the exact locations in the numerical model so that the resulting natural frequencies would be closest to the real value. Additionally, a mass was also applied to each node of the structure to bring the weight of the model closer to the weight of the real bridge, and this extra mass value was made to be equivalent to the sum of the masses of the components found at that node. The first 18 natural frequencies of the model are listed in Table 4.7, having maintained the boundary conditions of the previous impact test.

Table 4.7: Obtained natural frequency values from the numerical model

Modes	**Natural Frequency (Hz)**	**Modes**	**Natural Frequency (Hz)**
1	0.0000	10	34.530
2	8.518	11	38.043
3	11.994	12	43.828
4	12.233	13	45.327
5	12.951	14	65.384
6	14.918	15	65.409
7	15.879	16	80.108
8	23.003	17	84.866
9	25.245	18	87.768

Analyzing Table 4.7, specifically the frequency associated with the second vibration mode and comparing it with the calculated value, it is understood that the true natural frequency will be around these values ($[8.518, 14.719]Hz$). However, based on the example of the previous test, it is quite possible that the real value is not within this range.

The three trial runs where then conducted, leaving a longer time interval between impacts due to the greater oscillation felt. In the following figures, the plots from the first impact test run are presented, as well as graphs in the frequency domain for all runs scaled to $[0,50]Hz$ and $[0,100]Hz$. The remaining figures can be found in Appendix D.2.

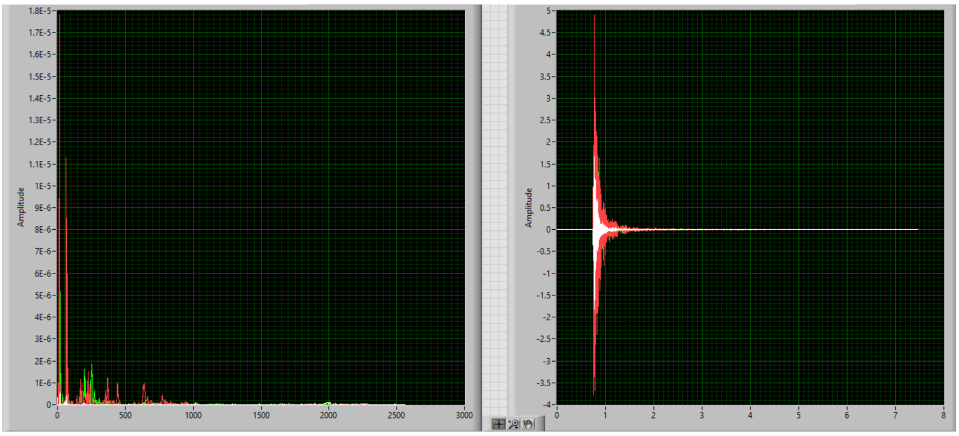

Figure 4.18: Graphical representation of the impact response amplitude of the first test as a function of frequency (left) and time (right).

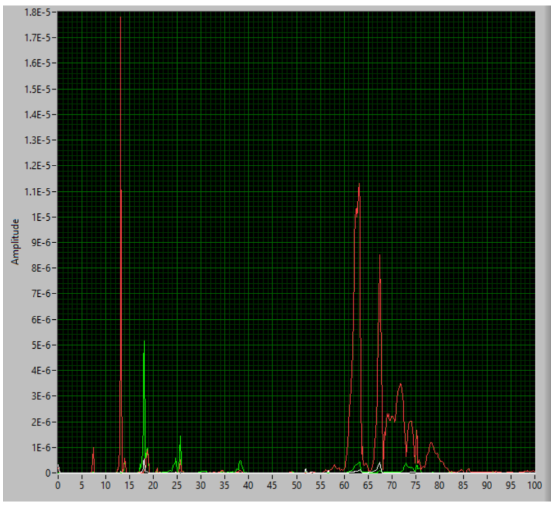

Figure 4.19: Graphical representation of the impact response amplitude of the first test as a function of frequency up to $100Hz$.

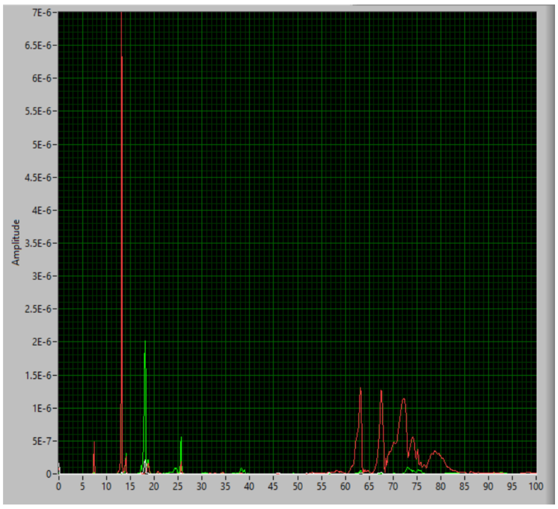

Figure 4.20: Graphical representation of the impact response amplitude of the second test as a function of frequency up to $100Hz$.

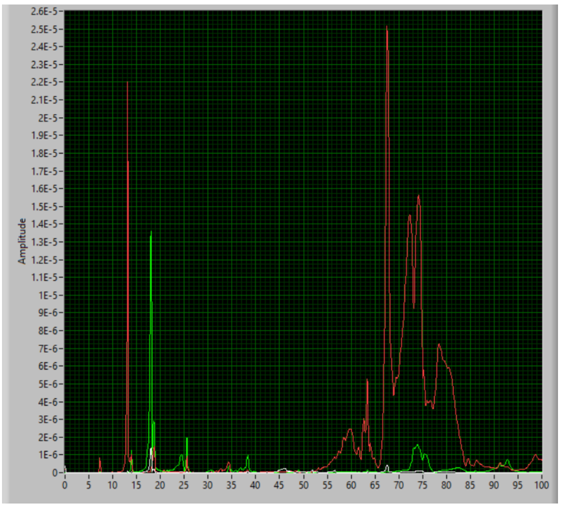

Figure 4.21: Graphical representation of the impact response amplitude of the third test as a function of frequency up to $100Hz$.

From the analysis of the graphs in the frequency domain scaled down to $100Hz$, it is possible to realize that not all tests had the same impact force and the respective response of the structure was also slightly different. This is proven by the amplitude of the peaks obtained, which although different do not show any relationship within the same test, for example, in Figure 4.20 we see a difference of about 7 times between red peaks, while in Figure 4.21 said difference is not so pronounced.

Moreover, it can be concluded that the value of the fundamental frequency obtained through the modal analysis of the numerical model was not very far from that recorded by the software. Well defined peaks are detected around the frequencies of $7.2Hz$, $14Hz$, $18Hz$, $25.5Hz$ and $38.5Hz$, and some small oscillations are visualized around $14Hz$, $18.5Hz$ and $24.5Hz$.

4.3.6 Impact test 3

Damage detection of a structure can be accomplished by appropriate modal analysis of the frequencies picked up by the appropriate sensing devices. In order to put this to the test, it was decided to perform another series of three trials on the structure with two of its members slightly unscrewed to simulate a possible fatigue failure on the bridge. The profiles chosen were those connecting the member under the greatest compressive stress to the central node, again on the side opposite to the instrumented one, since these are in tension when the bridge is loaded with four discs in each central zone.

The loosening was performed with the load already applied, trying as much as possible to make sure that the loosening torque was the same for all affected bolts and that the process was done as smoothly as possible. Only the bolts connecting the profiles to the upper gusset plates were untightened. It should be noted that it was clearly visible and audible the impact that the process had on the structure, so a decrease of the natural frequencies was predicted due to the reduction of the bridge's stiffness.

The impact was again achieved by dropping the same plastic ball with a weight of $114g$ and under the same conditions as in the previous experiment, the present test was performed. The signal captured during the trials was again processed and transformed by the interrogation software and presented graphically in both the time domain and frequency domain. In the following figures these results are displayed as well as graphs in the frequency domain magnified for better and easier analysis. The rest of the graphs can be found in the Appendix D.3.

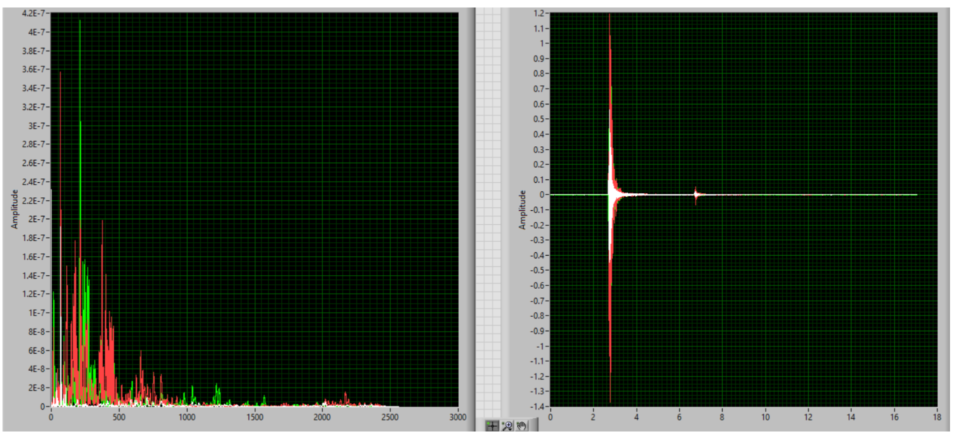

Figure 4.22: Graphical representation of the impact response amplitude of the first test as a function of frequency (left) and time (right).

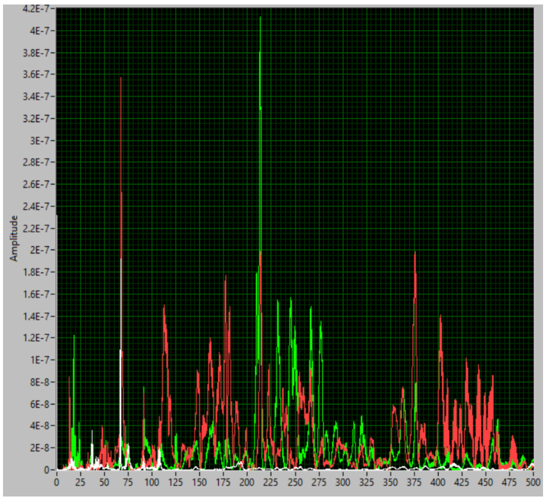

Figure 4.23: Graphical representation of the impact response amplitude of the first test as a function of frequency up to $500Hz$.

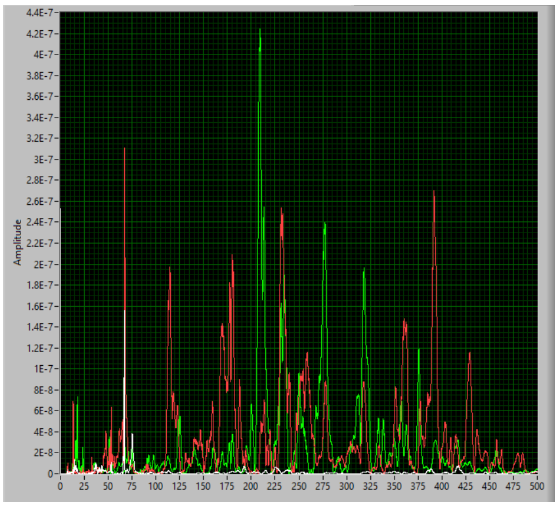

Figure 4.24: Graphical representation of the impact response amplitude of the second test as a function of frequency up to $500Hz$.

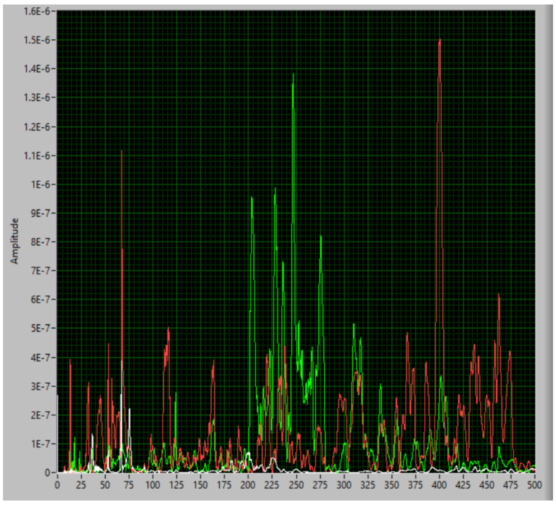

Figure 4.25: Graphical representation of the impact response amplitude of the third test as a function of frequency up to $500Hz$.

The most obvious aspect taken from the analysis of the plots is that the signal was highly contaminated by noise. The fact that the rigidity of the structure was reduced meant that the loads that would have been supported by the loosened members were distributed among the other components of the bridge, thus resulting in greater uncertainty of interpretation and prediction of results, as well as a greater oscillation of the bridge under any external perturbation. Additionally, it is noticeable that the amplitude of the peaks around the frequencies listed in the previous test results discussion was more attenuated, as was the overall amplitude of the remaining peaks. It can be noticed that the impact has redistributed the frequencies to much higher values than before.

4.4 Result discussion

This section covers the final analysis and discussion of the results obtained from all the tests performed and is divided into three subsections allusive to the different nature of them.

4.4.1 Preliminary evaluation

The main reason for this evaluation was to really get an idea of the similarity or differentiation between the structure modeled in ABAQUS and the one that was actually built. It was observed that the values of vertical displacement for the maximum available load and for the admissible load, obtained from the numerical model were about two times smaller than those resulting from the measurements made with the comparator and calculated according to the standards, respectively. This disparity of values can be motivated by several factors, one of them being the fact of having considered pin-connections in the simulation that increased the stiffness of the structure compared to the real model. The built bridge, when compared to the one modeled in ABAQUS, loses stiffness in the bolted connections and in the cutting errors made in some profiles, which do not provide perfect contact between the various members

Furthermore, the fact that the bridge is mounted at its ends on BOSCH 60x60 profiles, which in return are simply resting on the highly uneven and tilted floor, leads to even more measurement uncertainties. It was found that a simple touch on the structure would very easily change its position and consequently lead to the variation of values obtained. Nevertheless, due to the repeatability and consistency of the deflection values obtained in other tests unrelated to this dissertation, but which were performed in parallel, it can be concluded that the experiment was well performed.

4.4.2 Loading tests

The study of strain evolution upon applying loads on the structure was the driving motive for this series of tests. Through the comparison between the values recorded by the strain gauges during the tests and the strain plots resulting from the simulation of the structure in ABAQUS under the test conditions, a slight degree of inaccuracy was obtained. Given that the entire installation process and subsequent wiring was done by someone with very little experience, it is possible that there were mistakes made during the setup that led to the observable errors. A badly prepared surface or a poorly handled and/or mounted sensor can be the source of this variance.

In the numerical model, the structure was modeled considering pin-connections, which evidently is not the case in the built bridge due to physical impossibility. Nonetheless, the strain values obtained came very close to those expected. Also, it was considered that the loads were concentrated at the floor frame nodes, this being one of the assumptions necessary to consider the structure as a truss. However, due to the dimensions of the loads available in the laboratory these were placed exactly next to the nodes loading the bridge at slightly different locations than originally intended. This combined with the fact that it was not always possible to place the disks exactly in the same place and with the desired smoothness given their weight, are possible factors behind the small deviation in results observed.

In the third and final loading test, the sensors did not return to their initial state, i.e., after the removal of the load they did not emit the same signal as they did in the initial instants of the test, resulting in a variation in the final and initial value. As already mentioned, the structure was not supported on firm foundations, so the positioning and removal of the weights may have induced longitudinal displacements or unwanted oscillations, affecting the accuracy of the measured values.

4.4.3 Impact tests

Modal analysis is of utmost importance in the field of structural engineering, therefore studying the forced response of the bridge built by applying impulses on it in order to obtain its natural frequencies and vibration modes was the purpose given for this series of tests. It is evident that the prediction calculations performed to estimate the natural frequencies and the values taken from the modal analysis performed in ABAQUS were not entirely consistent with those actually obtained by the transformation of the signal, in either of the first two tests. Not only could a higher total mass of the structure have been considered when compared to the real value, but also, there may have been inaccuracies in the measurement of the vertical displacement of the bridge that underestimated the obtained stiffness constant. The fact that the connections between the profiles were achieved by bolting gusset plates or angle brackets, means that the signal captured by the accelerometer is at risk of contamination if these elements are not properly fastened. The dynamic behavior is the most sensitive to changes in the mass and stiffness properties of the structure, therefore it is dependent on the precision of the behavior of the nodes, hence the large divergence of the numerical results obtained.

The repeatability of peaks around fixed frequencies observed in the graphs generated by the software after signal transformation prove the effectiveness and validity of the measurements taken, even though their amplitude was not always the same. This was due to the practical impossibility of replicating an impulse of equal intensity between runs within the same test, since these were generated by a person and not by a piece of equipment. Additionally, in real applications it is possible to use methods of analysis in which the excitation comes from ambient noise caused by wind or passing vehicles.

In the last test, in which two members were loosened to assess whether this anomaly would be picked up by the acquisition system and later visualized in the graphical representation of the signal in the frequency domain, the unpredictability of the results was virtually guaranteed, since the loads had to be redistributed throughout the structure. It was predicted that either the natural frequencies would shift to lower frequency values given the induced stiffness reduction in the bridge or that the intensity of their peaks would drop considerably, with the latter being the case observed. The overall intensity of all the peaks was attenuated by about two orders of magnitude, and a distribution of the peaks to considerably higher frequency values was recorded.

Chapter 5

Conclusions

The present dissertation, with the main objective of designing and building a reduced scale metallic bridge with subsequent design of a system capable of monitoring its structural integrity, provides a better understanding of the existing monitoring techniques and the importance of the subject in current engineering projects. The drive to construct safer, stronger, but at the same time lighter structures has boosted the research in the area of structural engineering. Since poor verification of the calculations made in the design of a structure, by experimental means combined with numerical tools, can result in devastating human, economic and environmental damage, the monitoring of structural integrity appears as almost mandatory. The present project was developed based on the recognition that a bridge is in constant vibration and that if excited at frequencies close to its natural modes of vibration, it can result in excessive deformation of its structural elements and an increase in damping is foreseeable.

Throughout the course of the present thesis, all the steps and challenges encountered in the design and construction phases of the structure were discussed in great detail. The different designs of truss bridges most frequently employed were discussed, exposing their advantages and most important aspects. The choice of design and dimensions of the structure was justified, as well as all the elements that compose it, highlighting the manufacturing process adopted to obtain the gusset plates. The designed and achieved stiffness of a truss was strongly verified in this project.

Regarding the experimental component of the dissertation, the methods and practices adopted for the correct installation of the strain gauges and the accelerometer were discussed in great detail. A series of loading and impact tests were performed, and the results obtained were compared with numerical simulations or prediction calculations. The fact that the data acquisition system had already been previously configured with the interrogation and signal manipulation software, facilitated to a significant extent the execution of the various tests and subsequent analysis of the results. The choice of the members to be instrumented resulted from the numerical analysis of the model, based on the intention of studying the behavior of the most critical elements. The placement of the loads was prompted to prevent bending of the cross members and to also approximate the loading to a real situation where stresses are exerted at the nodes of the structure.

Finally, it is legitimate to state that the main objectives of the proposed thesis were all well achieved and addressed. The obtaining of the structural elements and the consequent construction of the structure phase proved to be extremely important, since if some more serious imprecision had been made when cutting the profiles, marking the holes in the gusset plates or tightening the bolts, the behavior of the bridge could have been completely different and its stiffness could have been compromised. From the signals emitted by the strain gauges, the effectiveness of the measurements is proven through comparison with the values obtained from the numerical modeling, having verified relative errors considerably low and acceptable, even though the foil strain gauges are the strain sensing devices with the lowest accuracy. The modal analysis performed was found to be greatly influenced by the intensity and location of the external force. The predicted and calculated natural frequencies turned out to be correct, deviating slightly from the values observed in the graphs in the frequency domain. Recall that on a real bridge the mass is much greater and its connections, both between members and externally, are much more robust and simpler to model. It was also possible to study the effect of noise in the measurements performed, more specifically in the last test.

As future works, it is believed that the repetition of the performed tests could further verify the results obtained, as well as the improvement of the numerical model so that it represents to a greater extent the constructed structure. In particular, the loosened members could be screwed back on, to verify that by releasing the ball on top of the discs, the natural frequencies would remain similar to those obtained in the second impact test. Furthermore, it would also be interesting to use the measurements taken by the accelerometer and, by means of a double signal integration algorithm, arrive at the bridge displacement in order to calculate the expected deformation. Naturally, the strain gauges already installed would serve as a means of verifying the accuracy of the method.

References

[1] Yongtao Dong, Ruiqiang Song, Helen Liu, et al. Bridges structural health monitoring and deterioration detection-synthesis of knowledge and technology. Technical report, Alaska. Dept. of Transportation and Public Facilities, 2010.

[2] HBM. Strain gage and accesssories. accessed on 27-04-2022.

[3] VPG Micro Measuremnets. Special use sensors—concrete embedment strain gages. docs.micro-measurements.com/?id=2647&_ga=2.202726358.657563296.1653300617-967108844.1651507767, 5 2017. accessed on 02-05-2022.

[4] RST Instruments Ltd. Vibrating wire arcweldable strain gauge (vwsg-a) manual. https://rstinstruments.com/wp-content/uploads/ELM0086C-Vibrating-Wire-Arcweldable-Strain-Gauge-VWSG-A-Manual.pdf, 10 2020. accessed on 30-04-2022.

[5] GEODATA Group. Surface mount strain gauge. https://www.geodata.com/wp-content/uploads/2020/07/Surface-mount-strain-gauges_20200723.pdf, 2020. accessed on 01-05-2022.

[6] Domingos Matos, Ricardo Pimentel, Joaquim Figueiras, Carlos Rodrigues, Remy Faria, and António Castro. Novel fiber optic transducers embedded into concrete mass applied to the new alto ceira dam. 10 2012.

[7] Ping Lu, Nageswara Lalam, Mudabbir Badar, Bo Liu, Benjamin Chorpening, Michael Buric, and P.R. Ohodnicki. Distributed optical fiber sensing: Review and perspective. *Applied Physics Reviews*, 6:041302, 09 2019.

[8] Bosch Rexroth AG. Basic mechanic elements. https://www.equinotec.com/web/galeria/family/pdf/158071623940392_MGE_14_EN_2019_07_Media_PDF.pdf, 2019. accessed on 10-04-2022.

[9] Daniele Inaudi and Branko Glisic. Continuous monitoring of concrete bridges during construction and service as a tool for data-driven bridge health monitoring. 2006.

[10] Jorge Brito, S. Santos, and Fernando Branco. Inspectionability? of bridges. *Structural Concrete*, 3:29–34, 01 2002.

[11] Américo Ocua Dimande. *Análise experimental de pontes durante a construção e em serviço*. PhD thesis, Faculdade de Engenharia da Universidade do Porto, 2008.

[12] Carlos Rodrigues, Carlos Félix, and Joaquim Figueiras. Monitorização estrutural de pontes com sistemas em fibra Ótica – três exemplos em portugal. 06 2013.

[13] Ana Cláudia Neves, John Leander, Ignacio Gonzalez, and Raid Karoumi. An approach to decision-making analysis for implementation of shm in bridges. *Structural Control and Health Monitoring*, 26, 03 2019.

[14] Filipe José Moreira Guerra dos Santos Cavadas. *Monitorização e análise do comportamento de pontes metálicas antigas : a Ponte Eiffel*. PhD thesis, Faculdade de Engenharia da Universidade do Porto, 2008.

[15] 2021 infrastructure report card. Technical report, 2021.

[16] Mehdi Modares and Natalie Waksmanski. Overview of structural health monitoring for steel bridges. *Practice Periodical on Structural Design and Construction*, 18:187–191, 08 2013.

[17] J Collins, G Mullins, C Lewis, D Winters, et al. State of the practice and art for structural health monitoring of bridge substructures. Technical report, United States. Federal Highway Administration. Office of Infrastructure, 2014.

[18] D. Inaudi. *Structural health monitoring of bridges: General issues and applications*, pages 339–370. 08 2009.

[19] Horst Czichos. *Handbook of Technical Diagnostics: Fundamentals and Application to Structures and Systems*. 01 2013.

[20] Konrad Bergmeister and U. Santa. Global monitoring concepts for bridges. *Structural Concrete*, 2:29–39, 01 2001.

[21] HBM. Strain gauges:first choice for strain measurements. https://www.hbm.com/fileadmin/mediapool/hbmdoc/technical/S01265.pdf. accessed on 02-05-2022.

[22] Miguel Montenegro. *Ensaios de carga em pontes - sistemas de medição e análise de resultados*. PhD thesis, 07 2011.

[23] RST Instruments Ltd. Vibrating wire strain gauge. https://rstinstruments.com/product/vibrating-wire-strain-gauge?action=genpdf&id=1684. accessed on 30-04-2022.

[24] Hui Li and Jinping Ou. The state of the art in structural health monitoring of cable-stayed bridges. *Journal of Civil Structural Health Monitoring*, 6, 05 2015.

[25] Helder Sousa, Carlos Félix, João Bento, and Joaquim Figueiras. Design and implementation of a monitoring system applied to a long-span prestressed concrete bridge. *Structural Concrete*, 12:82–93, 06 2011.

[26] Gerard Fernando, A. Hameed, D. Winter, J. Tetlow, Leng Jinsong, R. Barnes, G. Mays, and G. Kister. Structural integrity monitoring of concrete structures via optical fiber sensors: Sensor protection systems. *Structural Health Monitoring-an International Journal - STRUCT HEALTH MONIT*, 2:123–135, 06 2003.

[27] Alan D. Kersey and William W. Morey. Multiplexed bragg grating fibre-laser strain sensor system with mode-locked interrogation. *Electronics Letters*, 29, 1993.

[28] Yonas Muanenda, Claudio J. Oton, and Fabrizio Di Pasquale. Application of raman and brillouin scattering phenomena in distributed optical fiber sensing. *Frontiers in Physics*, 7, 2019.

[29] Weiwen Zou, Xin Long, and Jianping Chen. Brillouin scattering in optical fibers and its application to distributed sensors. In Moh Yasin, Hamzah Arof, and Sulaiman Wadi Harun, editors, *Advances in Optical Fiber Technology*, chapter 1. IntechOpen, Rijeka, 2015.

[30] Baidar Bakht and Aftab Mufti. *Bridges: Analysis, design, structural health monitoring, and rehabilitation*. Springer, 2015.

Appendix A

A.1 Bosch Profile Properties

Technical data – profiles

Profile	Slot	Profile surface A (cm^2)	Moment of inertia I_x (cm^4)	I_y (cm^4)	Moment of resistance W_x (cm^3)	W_y (cm^3)	Torsion index I_t (cm^4)	W_t (cm^3)	Weight m (kg/m)	Page
20x20	6	1.6	0.7	0.7	0.7	0.7	0.08	0.17	0.4	2-11
20x20 1N	6	1.9	0.8	0.8	0.8	0.8	0.60	0.67	0.5	2-11
20x20 2N	6	1.8	0.7	0.8	0.7	0.8	0.31	0.52	0.5	2-11
20x20 2NVS	6	1.8	0.7	0.7	0.7	0.7	0.37	0.52	0.5	2-12
20x20 3N	6	1.7	0.7	0.8	0.7	0.7	0.19	0.34	0.5	2-12
20x20 R	6	1.6	0.6	0.6	0.5	0.5	0.21	0.39	0.4	2-12
20x40	6	2.9	4.6	1.2	2.5	1.4	0.68	0.91	0.8	2-13
20x60	6	3.5	14.2	1.7	4.7	1.7	2.30	2.00	0.9	2-13
20x40x40	6	4.2	6.0	6.0	2.6	2.6	1.50	1.30	1.1	2-13
10x40	6	2.1	3.2	0.2	1.6	0.4	–	–	0.6	2-14
30x30	8	3.1	2.8	2.8	1.8	1.8	0.29	0.33	0.9	2-16
30x30 1N	8	3.7	3.1	3.5	2.0	2.3	2.80	1.50	1.0	2-16
30x30 2N	8	3.5	2.8	3.5	2.1	2.7	1.50	1.20	1.0	2-16
30x30 2NVS	8	3.5	3.1	3.1	2.0	2.0	1.70	1.10	1.0	2-17
30x30 3N	8	3.3	3.1	2.8	2.3	2.1	0.86	0.73	0.9	2-17
30x30°	8	3.7	3.5	3.6	2.0	1.9	1.50	2.00	1.0	2-17
30x45°	8	4.0	3.6	5.1	2.1	2.3	2.10	2.40	1.1	2-18
30x60°	8	3.6	3.0	4.1	1.7	1.9	1.50	2.00	1.0	2-18
30x30 R	8	2.9	2.3	2.3	1.4	1.4	0.81	1.20	0.8	2-18
30x60	8	5.5	19.6	5.1	7.0	3.9	2.60	2.10	1.5	2-19
30x60 4N	8	5.8	20.2	5.5	6.7	3.8	4.80	2.40	1.6	2-19
30x60x60	8	8.2	26.2	26.2	7.6	7.6	6.40	3.60	2.2	2-19
30x90	8	7.7	60.7	7.3	13.5	4.9	5.10	3.80	2.1	2-20
30x120	8	9.9	136.3	9.6	22.7	6.4	7.60	5.60	2.7	2-20
30x45	8/10	4.0	8.1	3.9	3.9	2.9	1.30	1.30	1.1	2-21
60x60 8N	8	9.8	39.7	39.7	13.2	13.2	19.30	6.80	2.6	2-21
11x20	8	1.0	0.5	0.1	0.7	0.3	–	–	0.3	2-21
15x120	8	9.0	110.4	2.2	18.4	2.7	–	–	2.4	2-22
40x40L	10	5.6	9.1	9.1	4.5	4.5	1.30	0.74	1.5	2-25
40x40L 0N	10	6.3	10.4	10.4	5.2	5.2	10.70	4.30	1.7	2-25
40x40L 1N	10	6.1	9.8	10.3	4.7	5.1	6.90	3.70	1.7	2-25
40x40L 2N	10	6.0	9.0	10.3	4.5	5.2	4.00	3.00	1.6	2-26
40x40L 2NVS	10	6.0	9.7	9.7	4.9	4.9	4.50	2.70	1.6	2-26
40x40L 3N	10	5.8	9.7	9.0	4.8	4.5	2.60	1.70	1.6	2-26
40x30°	10	6.2	9.4	11.8	4.7	5.9	3.00	3.10	1.7	2-27
40x45°	10	6.8	9.9	16.6	5.0	8.3	4.20	3.70	1.8	2-27
40x60°	10	6.3	8.7	13.1	4.3	6.5	3.00	3.10	1.7	2-27
40x40L R	10	5.0	7.2	7.2	3.6	3.6	2.50	2.00	1.3	2-28
40x40 HR	10	5.5	8.1	7.6	4.0	3.6	4.60	2.80	1.5	2-28

2

Bosch Rexroth AG, 3 842 540 392 (2019-07)

Figure A.1: BOSCH's 20x20 mm profile properties [8].

A.2 Profile Deflection

Profile deflection

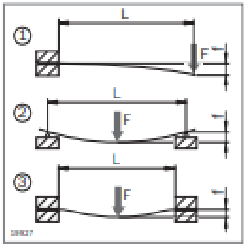

$f_{①} = \frac{F \times L^3}{3\,E \times I \times 10^4}$ $f_{②} = \frac{F \times L^3}{48\,E \times I \times 10^4}$ $f_{③} = \frac{F \times L^3}{192\,E \times I \times 10^4}$	Profile deflection due to force F for static load cases ①②③
$f_{①} = \frac{m' \times g \times L^4}{8\,E \times I \times 10^4}$ $f_{②} = \frac{5 \times m' \times g \times L^4}{384\,E \times I \times 10^4}$ $f_{③} = \frac{m' \times g \times L^4}{384\,E \times I \times 10^4}$	Profile deflection due to the profile's own weight
$\sigma_{①} = \frac{(m' \times g \times L + F) \times L}{W \times 10^3}$ $\sigma_{②} = \frac{(m' \times g \times L + F) \times L}{4\,W \times 10^3}$ $\sigma_{③} = \frac{(m' \times g \times L + F) \times L}{8\,W \times 10^3}$	Control of max. occurring bending stress $\sigma_{b\,max}$
$\sigma_{b\,max} < \sigma_{b\,zul.}!$ $\sigma_{b\,zul.} = \frac{R_{p0,2}}{S_{F\,erf.}}$	$S_{F\,req}$: Safety value required to avoid deformation (flow) $\sigma_{b\,zul}$: Max. permissible bending stress

f (mm)	W (cm^3)
F (N)	E = 70000 N/mm^2
L (mm)	m' (kg/mm); m' = m/1000; m (p. 2-3 ... 2-6)
I (cm^4)	g = 9.81 $m/s^2 \approx 10\ m/s^2$

Figure A.2: Profile deflection [8].

Appendix B

Profile Connections

B.1 Angle Brackets

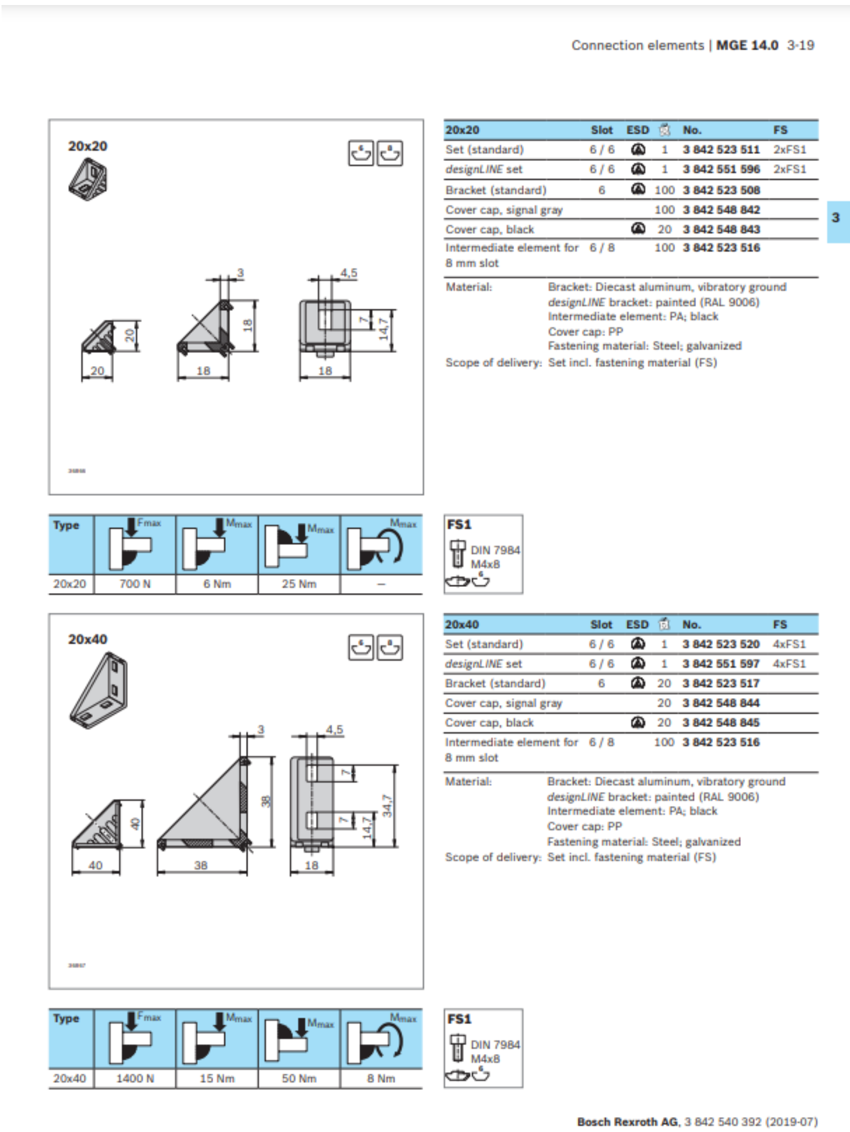

Connection elements | **MGE 14.0** 3-19

20x20	Slot	ESD		No.	FS
Set (standard)	6 / 6		1	**3 842 523 511**	2xFS1
designLINE set	6 / 6		1	**3 842 551 596**	2xFS1
Bracket (standard)	6		100	**3 842 523 508**	
Cover cap, signal gray			100	**3 842 548 842**	
Cover cap, black			20	**3 842 548 843**	
Intermediate element for 8 mm slot	6 / 8		100	**3 842 523 516**	

Material: Bracket: Diecast aluminum, vibratory ground
designLINE bracket: painted (RAL 9006)
Intermediate element: PA; black
Cover cap: PP
Fastening material: Steel; galvanized
Scope of delivery: Set incl. fastening material (FS)

Type	F_{max}	M_{max}	M_{max}	M_{max}
20x20	700 N	6 Nm	25 Nm	–

FS1: DIN 7984 M4x8

20x40	Slot	ESD		No.	FS
Set (standard)	6 / 6		1	**3 842 523 520**	4xFS1
designLINE set	6 / 6		1	**3 842 551 597**	4xFS1
Bracket (standard)	6		20	**3 842 523 517**	
Cover cap, signal gray			20	**3 842 548 844**	
Cover cap, black			20	**3 842 548 845**	
Intermediate element for 8 mm slot	6 / 8		100	**3 842 523 516**	

Material: Bracket: Diecast aluminum, vibratory ground
designLINE bracket: painted (RAL 9006)
Intermediate element: PA; black
Cover cap: PP
Fastening material: Steel; galvanized
Scope of delivery: Set incl. fastening material (FS)

Type	F_{max}	M_{max}	M_{max}	M_{max}
20x40	1400 N	15 Nm	50 Nm	8 Nm

FS1: DIN 7984 M4x8

Bosch Rexroth AG, 3 842 540 392 (2019-07)

Figure B.1: 20x20 Angle Bracket [8].

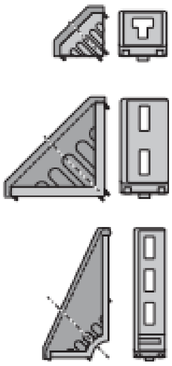

	Slot			F_{max}	M_{max}	M_{max}	M_{max}
20/20	6	↻	3 Nm	700 N	6 Nm	25 Nm	–
20/40	6	↻	3 Nm	1400 N	15 Nm	50 Nm	8 Nm
30/30	8	↻	10 Nm	1250 N	25 Nm	75 Nm	–
30/60	8	↻	10 Nm	2500 N	100 Nm	170 Nm	25 Nm
30/120	8	↻	10 Nm	3750 N	100 Nm		47 Nm
60/60-8	8	↻	10 Nm	5000 N	320 Nm	370 Nm	110 Nm
60/60-10	10	↻	25 Nm	3000 N	125 Nm	150 Nm	–
40/40	10	↻	25 Nm	3000 N	55 Nm	145 Nm	35 Nm
40/80	10	↻	25 Nm	6000 N	180 Nm	400 Nm	60 Nm
40/160	10	↻	25 Nm	9000 N	250 Nm		60 Nm
80/80	10	↻	25 Nm	14000 N	500 Nm	1000 Nm	400 Nm
45/45	10	↻	25 Nm	3000 N	60 Nm	160 Nm	–
45/90	10	↻	25 Nm	6000 N	180 Nm	400 Nm	60 Nm
45/180	10	↻	25 Nm	9000 N	250 Nm		65 Nm
90/90	10	↻	25 Nm	12000 N	370 Nm	800 Nm	200 Nm
43x42	10	↻	25 Nm	2000 N	–	160 Nm	–
50/50	10	↻	25 Nm	4000 N	125 Nm	250 Nm	38 Nm
50/100	10	↻	25 Nm	7500 N	300 Nm	600 Nm	73 Nm
100/100	10	↻	25 Nm	15000 N	550 Nm	1100 Nm	480 Nm

Bracket (p. 3-18)

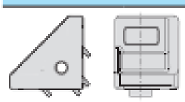

	Slot			F_{max}	M_{max}	M_{max}
S 20x20	6	↻	2.5 Nm	700 N	3.6 Nm	25 Nm
S 30x30	8	↻	8.5 Nm	1250 N	16 Nm	75 Nm
S 40x40	10	↻	25 Nm	3000 N	36 Nm	160 Nm
S 45x45	10	↻	25 Nm	3000 N	36 Nm	160 Nm

Bracket S (p. 7-8)

18

Figure B.2: 20x20 Angle Bracket [8].

B.2 T-nuts

3-4 **MGE 14.0** | Connection elements

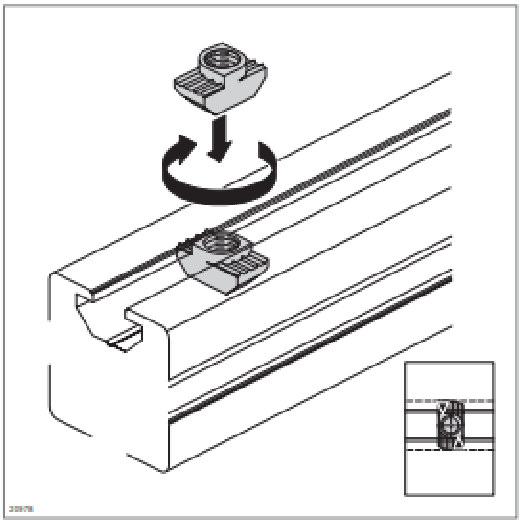

T-nut

- Standard element for a secure and conductive connection
- End stop for correct positioning in the profile slot
- Stainless steel T-nut, e.g. for outdoor or cleanroom applications
- Profile finishing: Not required

Technical data (p. 18-15)

Accessories:
Insulating cap (p. 3-5)

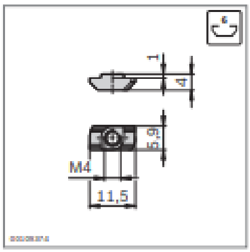

Slot	F_{max}
6	1700 N

T-nut, 6 mm slot	Slot	M	ESD		No.
Steel; galvanized	6	M4		100	3 842 523 135
Stainless steel	6	M4		100	3 842 536 599

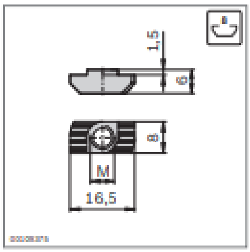

Slot	F_{max}
8 (M6)	4000 N

T-nut, 8 mm slot	Slot	M	ESD		No.
Steel; galvanized	8	M4		100	3 842 501 751
		M5*		100	3 842 501 752
		M6*		100	3 842 501 753
Stainless steel	8	M4		100	3 842 536 600
		M5		100	3 842 536 601
		M6		100	3 842 536 602

* Suitable for standard screws. **Attention:** T-nuts have driving torque for safe turning in the base of the slot.

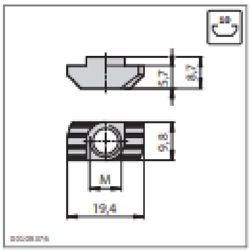

Slot	F_{max}
10 (M8)	6000 ... 18000 N[1]

[1] Depending on profile (p. 19-5)

T-nut, 10 mm slot	Slot	M	ESD		No.
Steel; galvanized	10	M4		100	3 842 530 281
		M5*		100	3 842 530 283
		M6*		100	3 842 530 285
		M8*		100	3 842 530 287
Stainless steel	10	M4		100	3 842 536 606
		M5		100	3 842 536 605
		M6		100	3 842 536 604
		M8		100	3 842 536 603

* Suitable for standard screws. **Attention:** T-nuts have driving torque for safe turning in the base of the slot.

Bosch Rexroth AG, 3 842 540 392 (2019-07)

Figure B.3: Used M4 T-nuts [8].

B.3 Gusset Plates

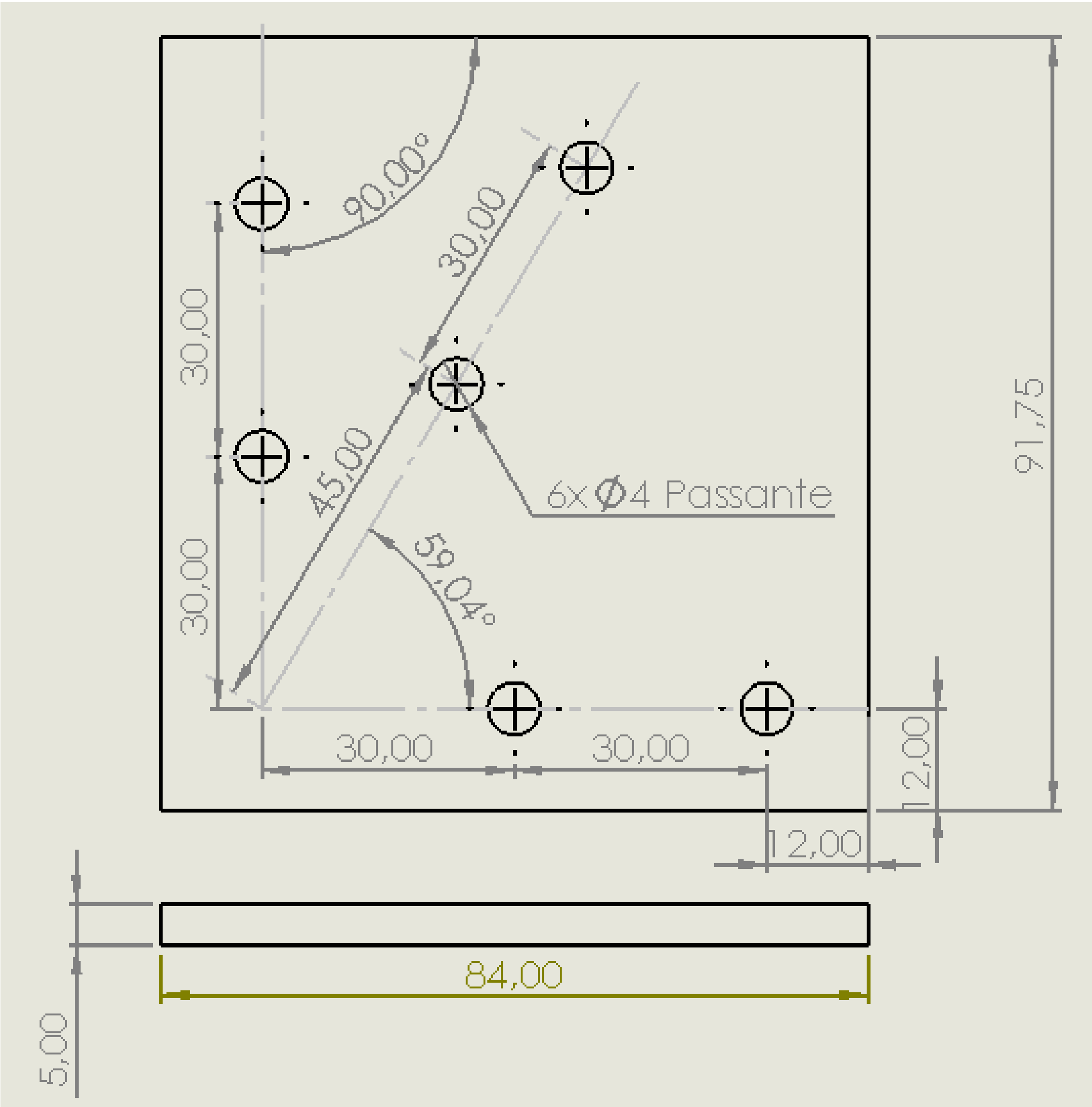

Figure B.4: Connection of floor diagonal member with frame.

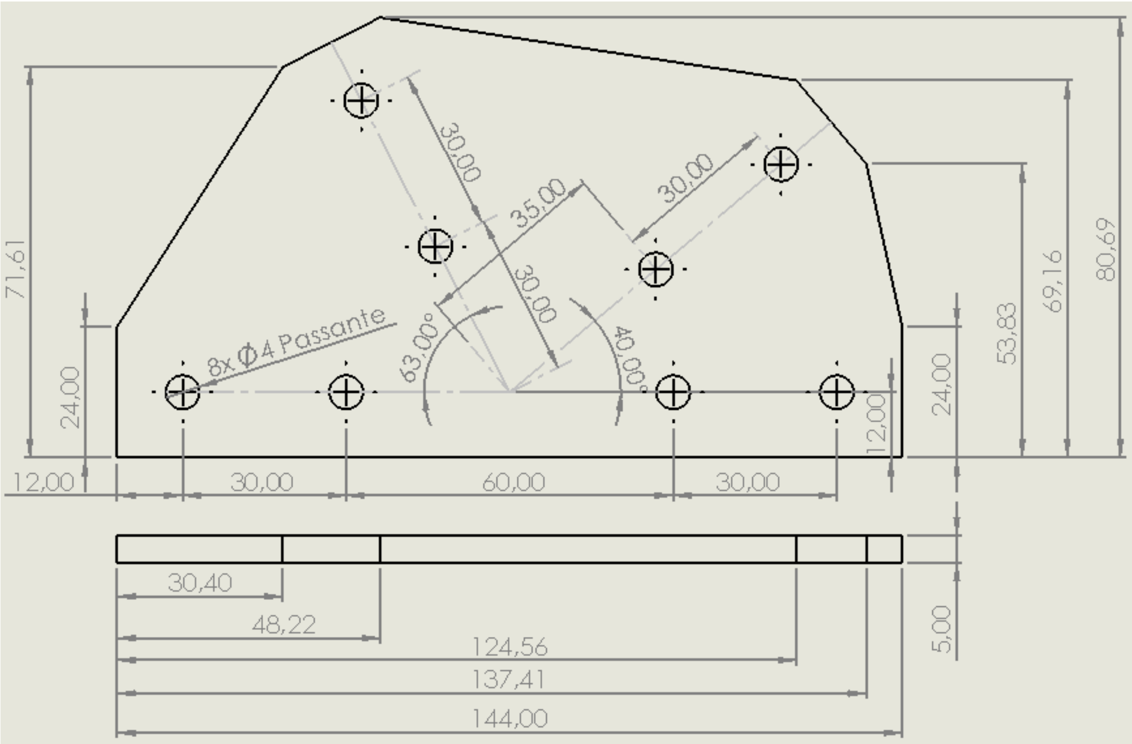

Figure B.5: Connection between longitudinal members and triangle inclined members.

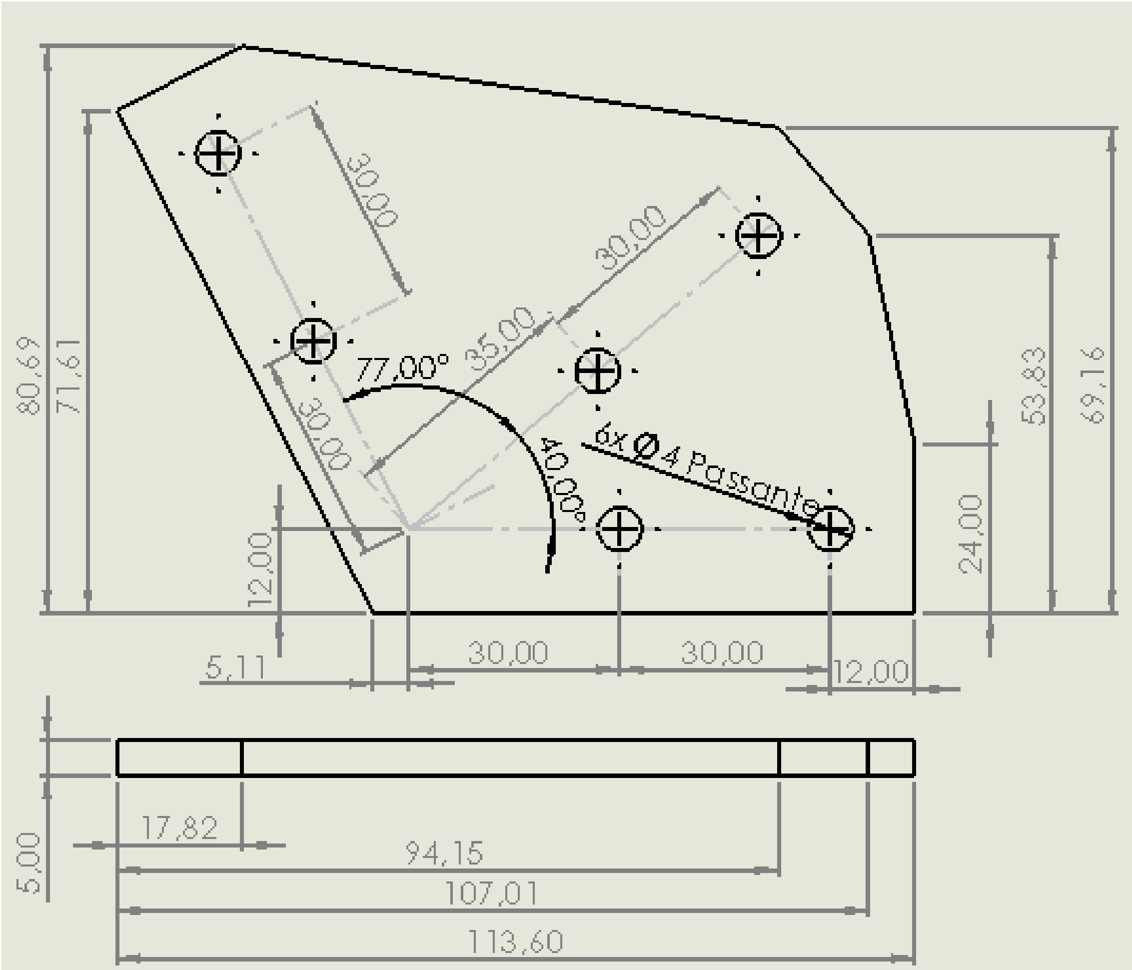

Figure B.6: Upper corner connection 1.

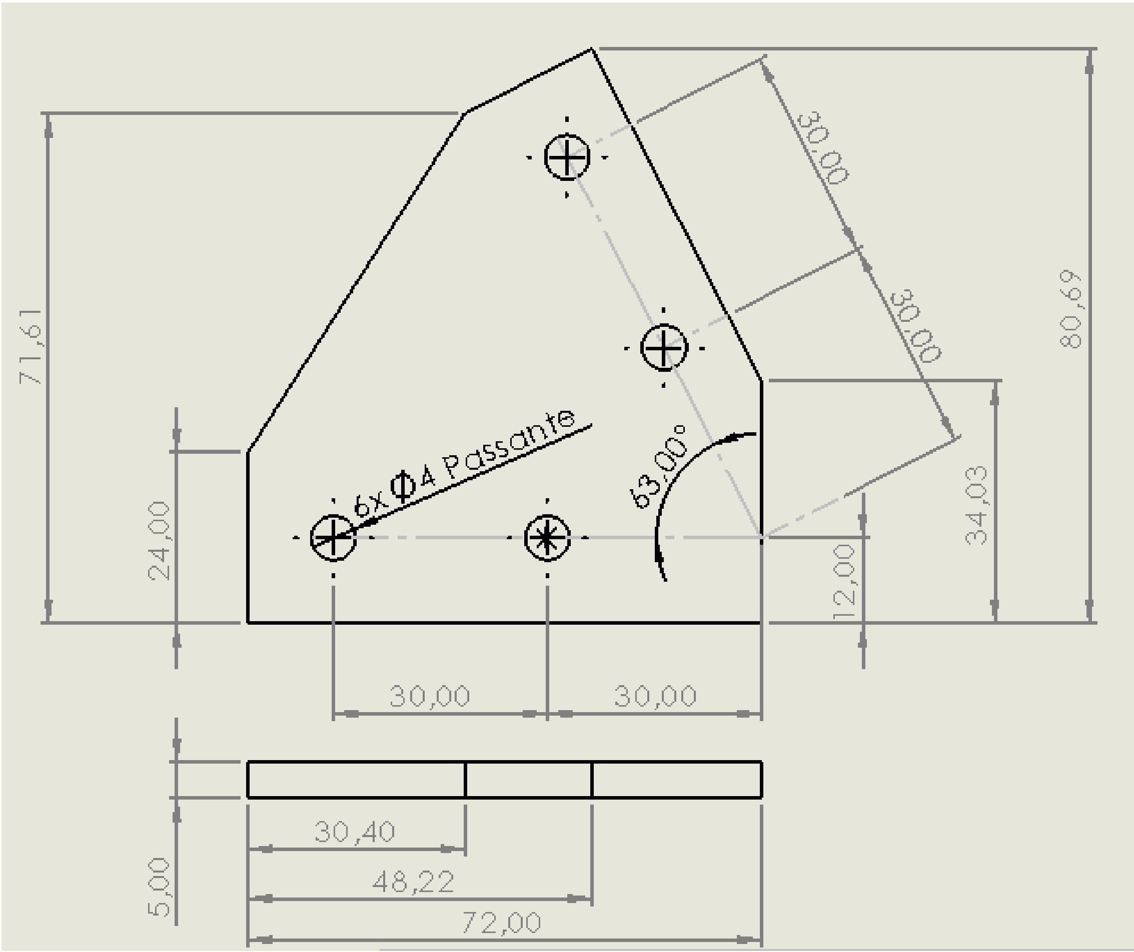

Figure B.7: Upper corner connection 2.

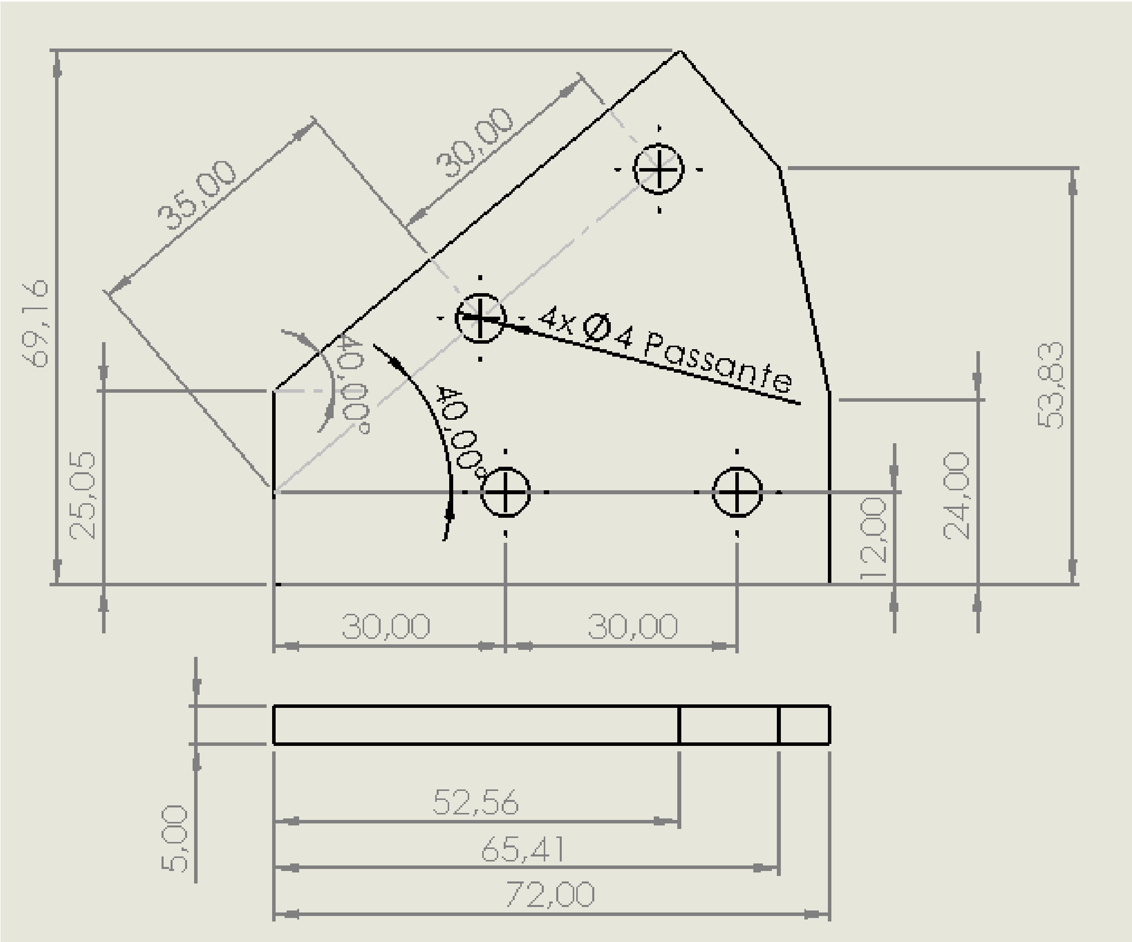

Figure B.8: Floor corner connection 1.

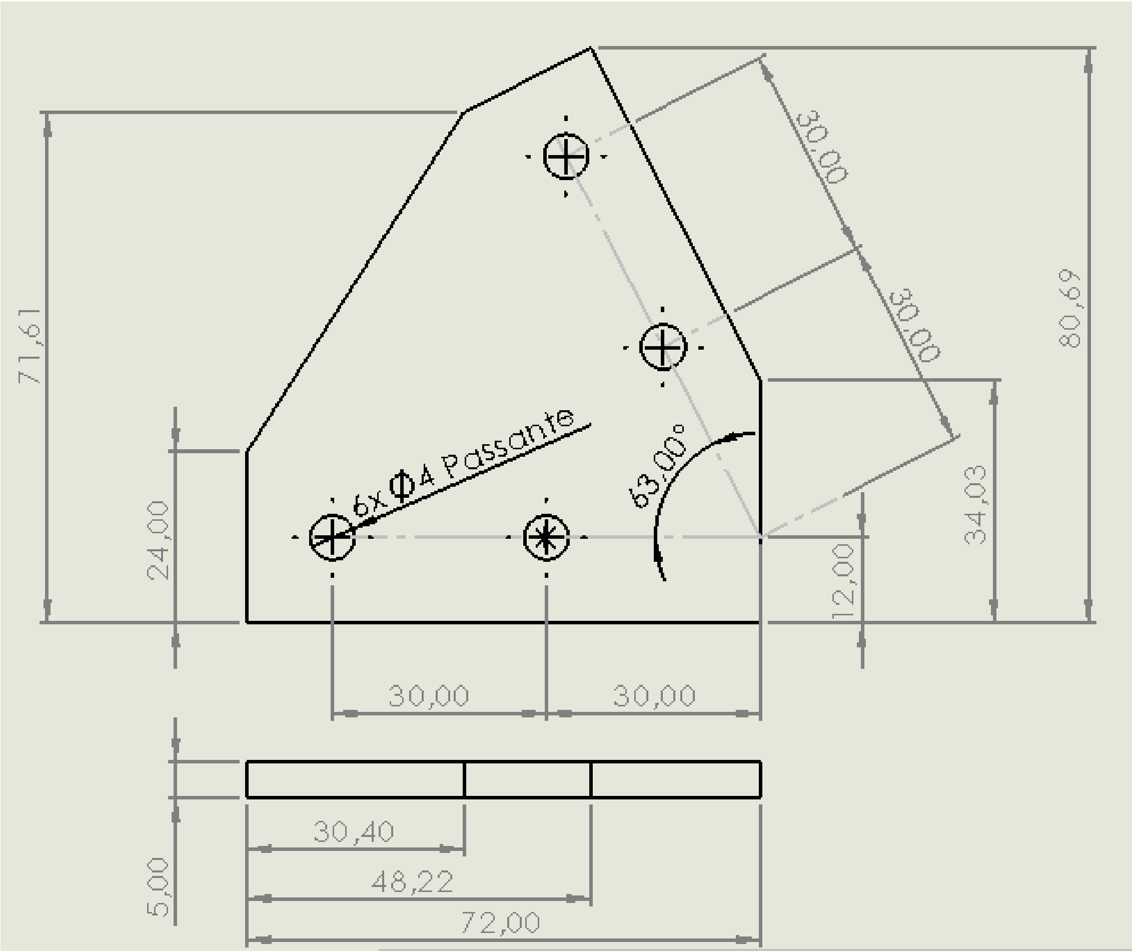

Figure B.9: Floor corner connection 2.

Appendix C

Strain gauge specifications

C.1 HBM 1-LY43-3/120 foil strain gauge specifications

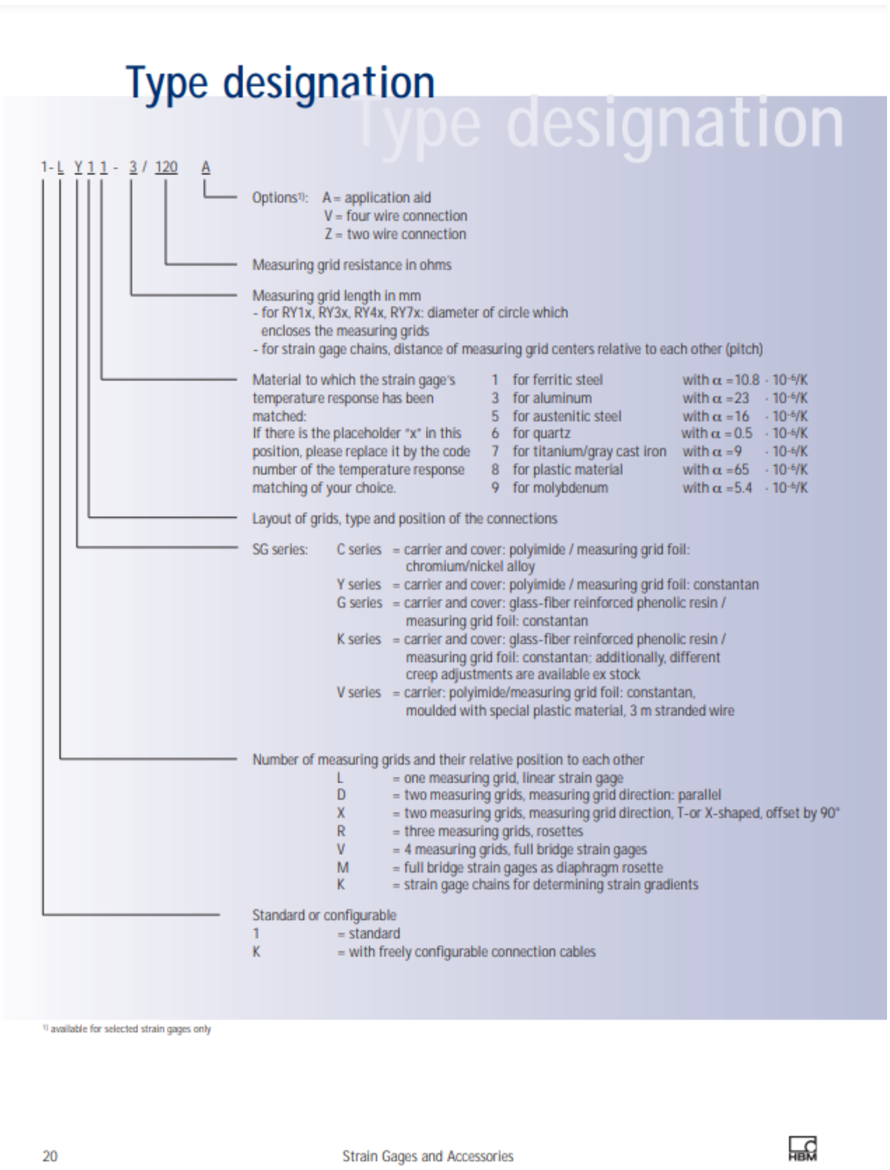
Type designation

1-L Y 1 1 - 3 / 120 A

Options[1]: A = application aid
V = four wire connection
Z = two wire connection

Measuring grid resistance in ohms

Measuring grid length in mm
- for RY1x, RY3x, RY4x, RY7x: diameter of circle which encloses the measuring grids
- for strain gage chains, distance of measuring grid centers relative to each other (pitch)

Material to which the strain gage's temperature response has been matched:
If there is the placeholder "x" in this position, please replace it by the code number of the temperature response matching of your choice.

1	for ferritic steel	with α = 10.8 · 10^{-6}/K
3	for aluminum	with α = 23 · 10^{-6}/K
5	for austenitic steel	with α = 16 · 10^{-6}/K
6	for quartz	with α = 0.5 · 10^{-6}/K
7	for titanium/gray cast iron	with α = 9 · 10^{-6}/K
8	for plastic material	with α = 65 · 10^{-6}/K
9	for molybdenum	with α = 5.4 · 10^{-6}/K

Layout of grids, type and position of the connections

SG series:
C series = carrier and cover: polyimide / measuring grid foil: chromium/nickel alloy
Y series = carrier and cover: polyimide / measuring grid foil: constantan
G series = carrier and cover: glass-fiber reinforced phenolic resin / measuring grid foil: constantan
K series = carrier and cover: glass-fiber reinforced phenolic resin / measuring grid foil: constantan; additionally, different creep adjustments are available ex stock
V series = carrier: polyimide/measuring grid foil: constantan, moulded with special plastic material, 3 m stranded wire

Number of measuring grids and their relative position to each other
L = one measuring grid, linear strain gage
D = two measuring grids, measuring grid direction: parallel
X = two measuring grids, measuring grid direction, T-or X-shaped, offset by 90°
R = three measuring grids, rosettes
V = 4 measuring grids, full bridge strain gages
M = full bridge strain gages as diaphragm rosette
K = strain gage chains for determining strain gradients

Standard or configurable
1 = standard
K = with freely configurable connection cables

[1] available for selected strain gages only

20 Strain Gages and Accessories HBM

Figure C.1: HBM 1-LY43-3/120 specifications [2].

Specifications

strain gage construction		foil SG complete with embedded measuring grid
measuring grid		
material		Constantan foil
thickness	µm	3.8 or 5, depending on strain gage type
carrier		
material	µm	polyimide
thickness		45 ± 10
cover		
material		polyimide
thickness	µm	25 ± 5
connections		nickel plated Cu leads, approx. 30mm in length.
for strain gages without leads		integrated solder tabs, approx. 1.5mm in length, approx. 1.6 ... 2.2mm wide
nominal resistance	Ω	120, 350, 700, or 1000, depending on SG type
resistance tolerance	%	± 0.3 without; ± 0.35 with leads)
gage factor		approx. 2
nominal value of the gage factor		specified on each package
gage factor tolerance for 0.6mm and 1.5mm measuring grid length	%	± 1.5
for ≥3 mm measuring grid length	%	± 1
temperature coefficient of the gage factor	1/K	approx. (115 ± 10) · 10^{-6}
nominal value of the temperature coefficient of the gage factor		specified on each package
reference temperature	°C	23
operating temperature range		
for absolute, i.e. zero point related measurements	°C	-70 ... + 200
for relative, i.e. not zero point related measurements	°C	-200 ... + 200
transverse sensitivity		specified on each package
within reference temperature range using adhesive Z 70 on strain gage type LY 11-6/120	%	- 0.1
temperature response		specified on each package
temperature response at customer's choice matched to the thermal expansion coefficient		
α for ferritic steel	1/K	10.8 · 10^{-6}
α for aluminum	1/K	23 · 10^{-6}
α for plastic material	1/K	65 · 10^{-6}
α for austenitic steel	1/K	16 · 10^{-6}
α for titanium/ gray steel	1/K	9 · 10^{-6}
α for molybdenum	1/K	5.4 · 10^{-6}
α for quartz	1/K	0.5 · 10^{-6}
tolerance of the temperature response	1/K	± 0.3 · 10^{-6}
temperature response with matching in the range of[3]	°C	-10... + 120
mechanical hysteresis[1]		
at reference temperature and strain ε = ± 1,000 µm/m on strain gage type LY 11-6/120		
at 1st load cycle and adhesive Z 70	µm/m	1
at 3rd load cycle and adhesive Z 70	µm/m	0.5
at 1st load cycle and adhesive X 60	µm/m	2.5
at 3rd load cycle and adhesive X 60	µm/m	1
at 1st load cycle and adhesive EP 250	µm/m	1
at 3rd load cycle and adhesive EP 250	µm/m	1
maximum elongation[1]		
at reference temperature using adhesive Z 70 on strain gage type LY 11-6/120		
absolute strain value ε for positive direction	µm/m	50,000 (≙5 %)
absolute strain value ε for negative direction	µm/m	50,000 (≙5 %)
fatigue life1)		
at reference temperature using adhesive X 60 on strain gage type LY 11-6/120		
number of load cycles L_W at		
alternating strain ε_W = ± 1,000 µm/m and zero point drift ε_m Δ ≦ 300 µm/m		>> 10^7 (test was interrupted at 10^7)
ε_m Δ ≦ 30 µm/m		> 10^7 (test was interrupted at 10^7)
minimum radius of curvature, longitudinal and transverse, at reference temperature		
for strain gages with leads	mm	0.3
for strain gages with integrated solder tabs		
within the measuring grid area	mm	0.3
within the area of the solder tabs	mm	2
bonding material that can be used		
cold curing adhesives		Z 70; X 60; X 280
hot curing adhesives		EP 250; EPS 310S

[1] The data depend on the various parameters of the specific application and are therefore stated for representative examples only.
[2] With measuring grid lengths of 0.6 mm, the nominal resistance may deviate by ± 1%. For the types LY 51/ LY5x the deviation is ± 0.75%. For XY9x, RY9x and the KY types (per chain) it is ± 0.5%.
[3] Matching to plastic (code numer 8) is only possible in the temperature range of -10...+50°C.

HBM Strain Gages and Accessories 23

Figure C.2: HBM 1-LY43-3/120 specifications [2].

SG / Y series with 1 measuring grid / linear strain gages

Stock types: Steel	Stock types: Aluminum	Variants: Others	Nominal resistance Ω	Dimensions (mm) [1 inch = 25.4 mm] Measuring grid a	Measuring grid b	Measuring grid carrier c	Measuring grid carrier d	Max. perm. effective bridge excitation voltage V	Solder terminals (1)
1-LY41-0.6/120		1-LY4x-0.6/120#	120	0.6	1.2	6	4	1.5	LS 5
1-LY41-1.5/120		1-LY4x-1.5/120	120	1.5	1.2	7	5	2.5	LS 5
1-LY41-3/120	1-LY43-3/120	1-LY4x-3/120	120	3	1.1	8	5	3.5	LS 5
		1-LY4x-3/120A	120	3	1.1	8	5	3.5	LS 5
1-LY41-6/120	1-LY43-6/120	1-LY4x-6/120	120	6	2.3	13.9	5.9	8	LS 5
1-LY41-6/120A		1-LY4x-6/120A	120	6	2.3	13.9	5.9	8	LS 5
1-LY41-10/120		1-LY4x-10/120	120	10	5	18	8	14	LS 5
		1-LY4x-10/120A	120	10	5	18	8	14	LS 5
1-LY41-20/120		1-LY4x-20/120	120	20	0.7	31.8	8.2	6.5	LS 5
1-LY41-50/120		1-LY4x-50/120	120	50	0.9	63.6	8.2	12	LS 5
1-LY41-100/120		1-LY4x-100/120	120	100	1	114.8	8.2	19	LS 5
1-LY41-150/120		1-LY4x-150/120	120	150	1.3	165.6	8.2	25	LS 5
1-LY41-1.5/350		1-LY4x-1.5/350#	350	1.5	2.3	9.2	5.9	6.5	LS 5
1-LY41-3/350	1-LY43-3/350	1-LY4x-3/350	350	3	2.5	10.9	5.9	9	LS 5
1-LY41-3/350A		1-LY4x-3/350A	350	3	2.5	10.9	5.9	9	LS 5
1-LY41-6/350	1-LY43-6/350	1-LY4x-6/350	350	6	2.7	13.9	5.9	15	LS 5
1-LY41-6/350A		1-LY4x-6/350A	350	6	2.7	13.9	5.9	15	LS 5
1-LY41-10/350		1-LY4x-10/350	350	10	5	18	8	24	LS 5
		1-LY4x-10/350A	350	10	5	18	8	24	LS 5
1-LY41-3/700	1-LY43-3/700	1-LY4x-3/700	700	3	2.7	10.9	5.9	13	LS 5
1-LY41-6/700		1-LY4x-6/700	700	6	4.1	13.9	5.9	23	LS 5
1-LY41-10/700		1-LY4x-10/700	700	10	5	18	8	33	LS 5
		1-LY4x-3/1000#	1000	3	2.7	10.9	5.9	16	LS 5
1-LY41-6/1000		1-LY4x-6/1000#	1000	6	4.3	13.9	5.9	27	LS 5
		1-LY4x-10/1000#	1000	10	5	18	8	40	LS 5

(1) Solder terminals are not compulsory
Types marked # are only available with matching to aluminum, ferritic or austenitic steel

LY41

Linear strain gage
Temperature response matched to steel with $\alpha = 10.8 \cdot 10^{-6}$/K

LY43

Temperature response matched to aluminum
with $\alpha = 23 \cdot 10^{-6}$/K

LY4x

Temperature response matching at customer's choice,
see page 20

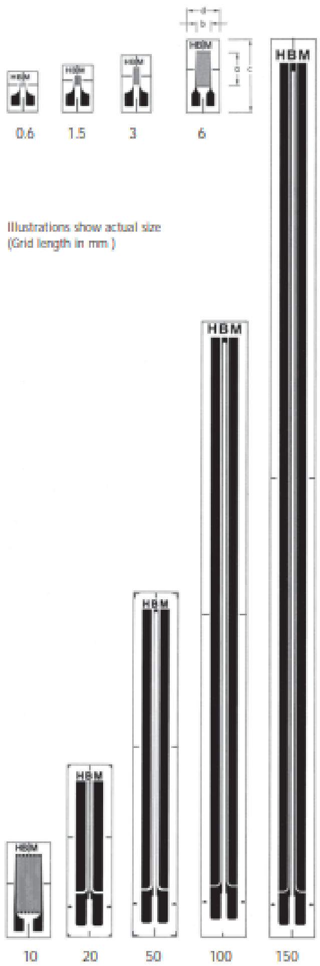

Illustrations show actual size
(Grid length in mm)

Contents per package: 10 pcs.

Figure C.3: HBM 1-LY43-3/120 specifications [2].

Appendix D

Obtained plots from the various impact tests

D.1 Resulting plots from the first impact test

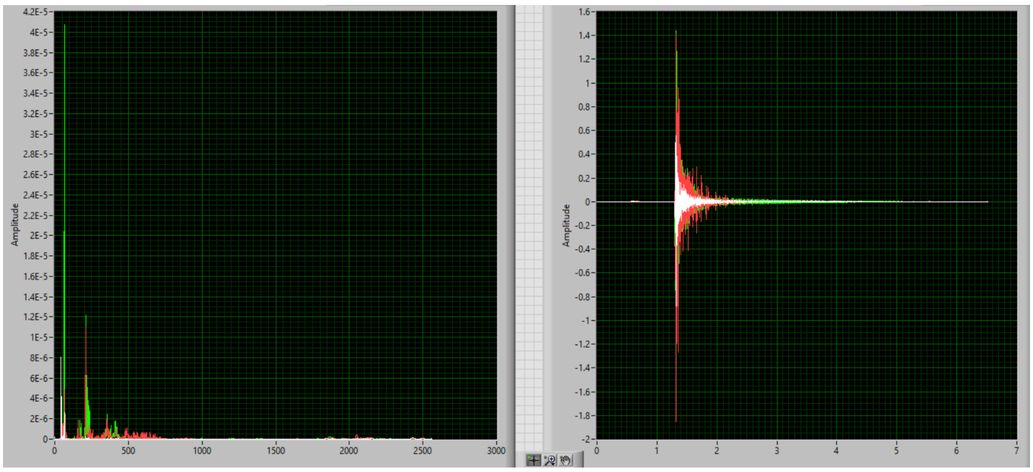

Figure D.1: Plots of the second test run.

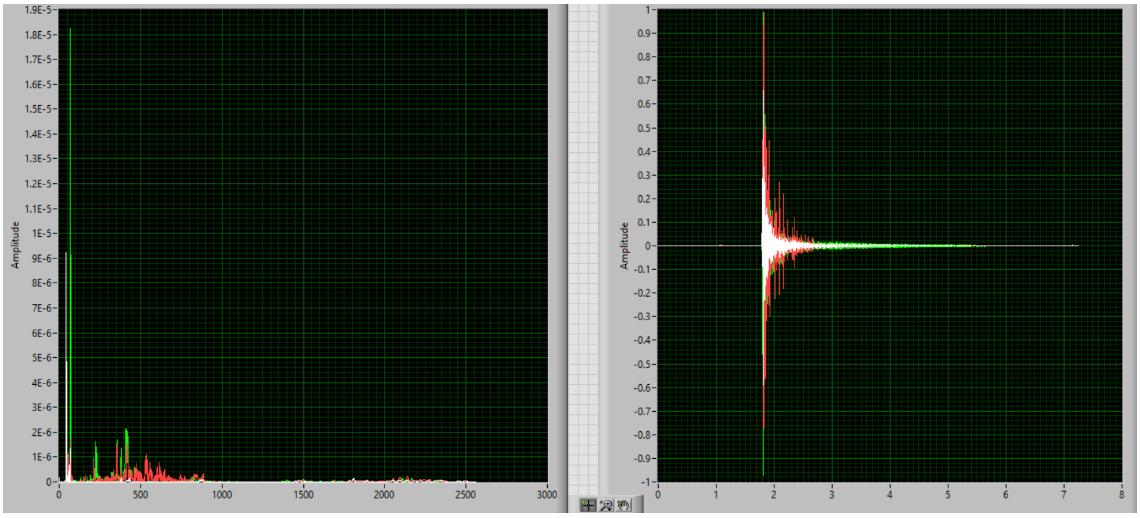

Figure D.2: Plots of the third test run.

D.2 Resulting plots from the second impact test

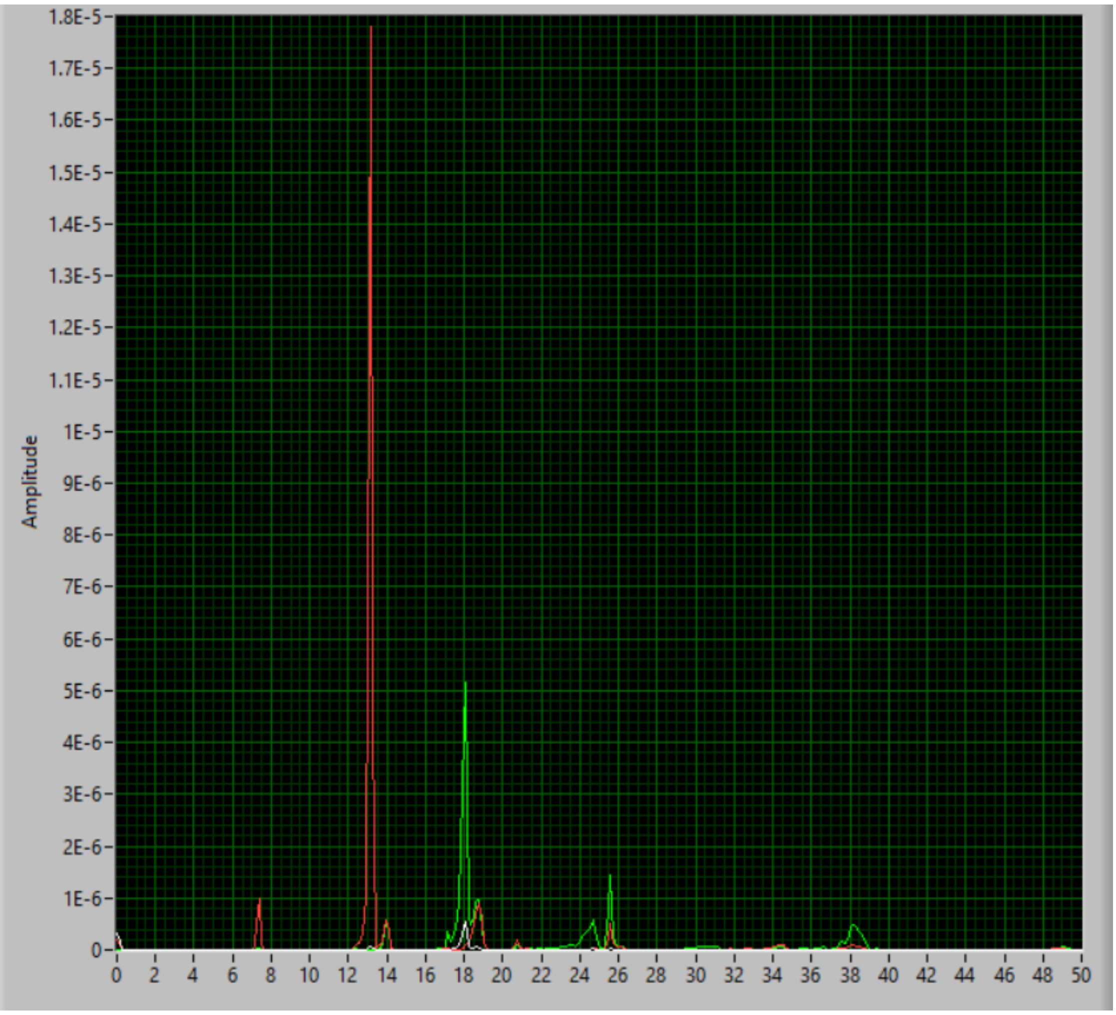

Figure D.3: Frequency plot of the first test run scaled to $[0, 50]Hz$.

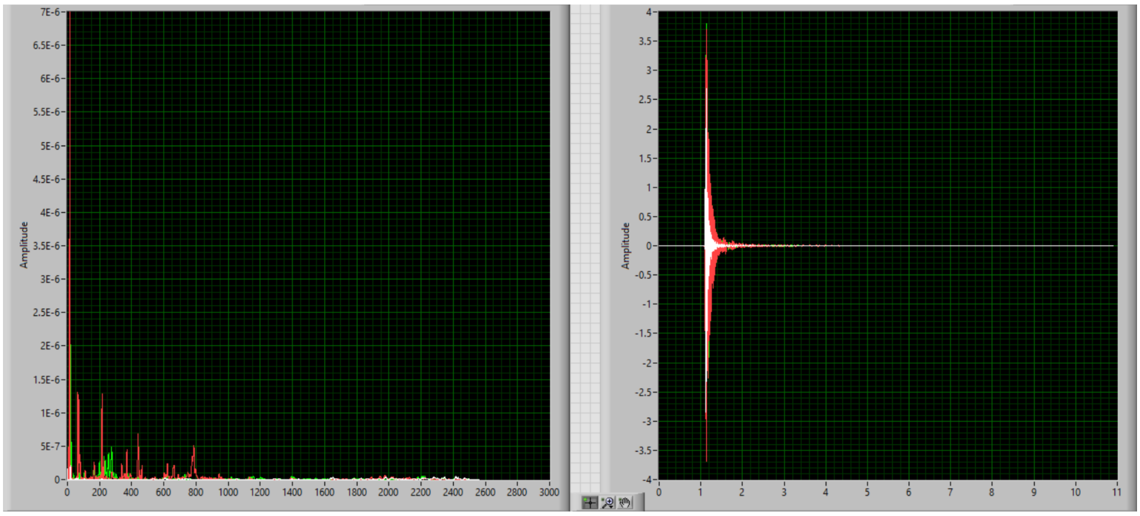

Figure D.4: Plots of the second test run.

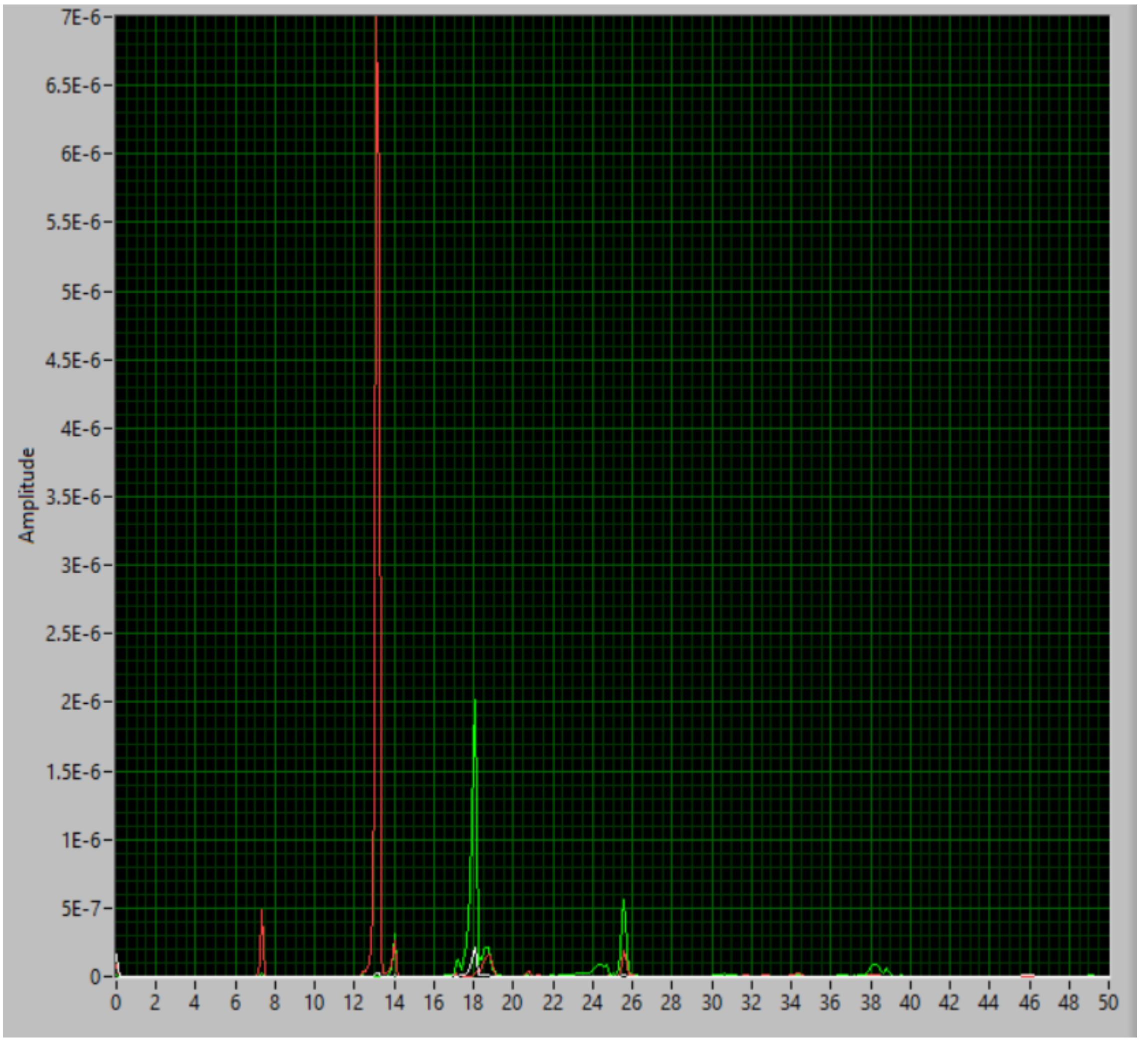

Figure D.5: Frequency plot of the second test run scaled to $[0,50]Hz$.

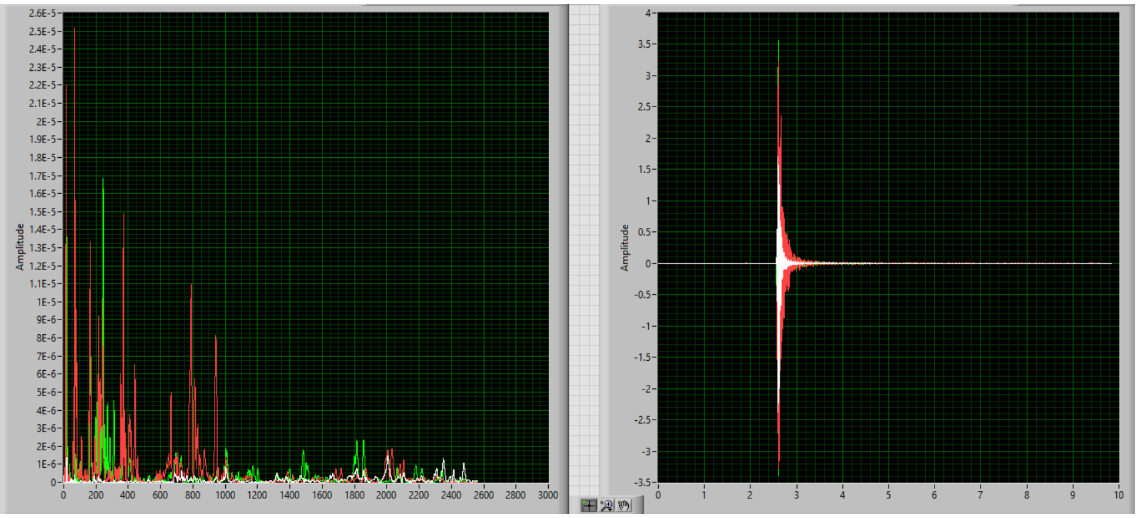

Figure D.6: Plots of the third test run.

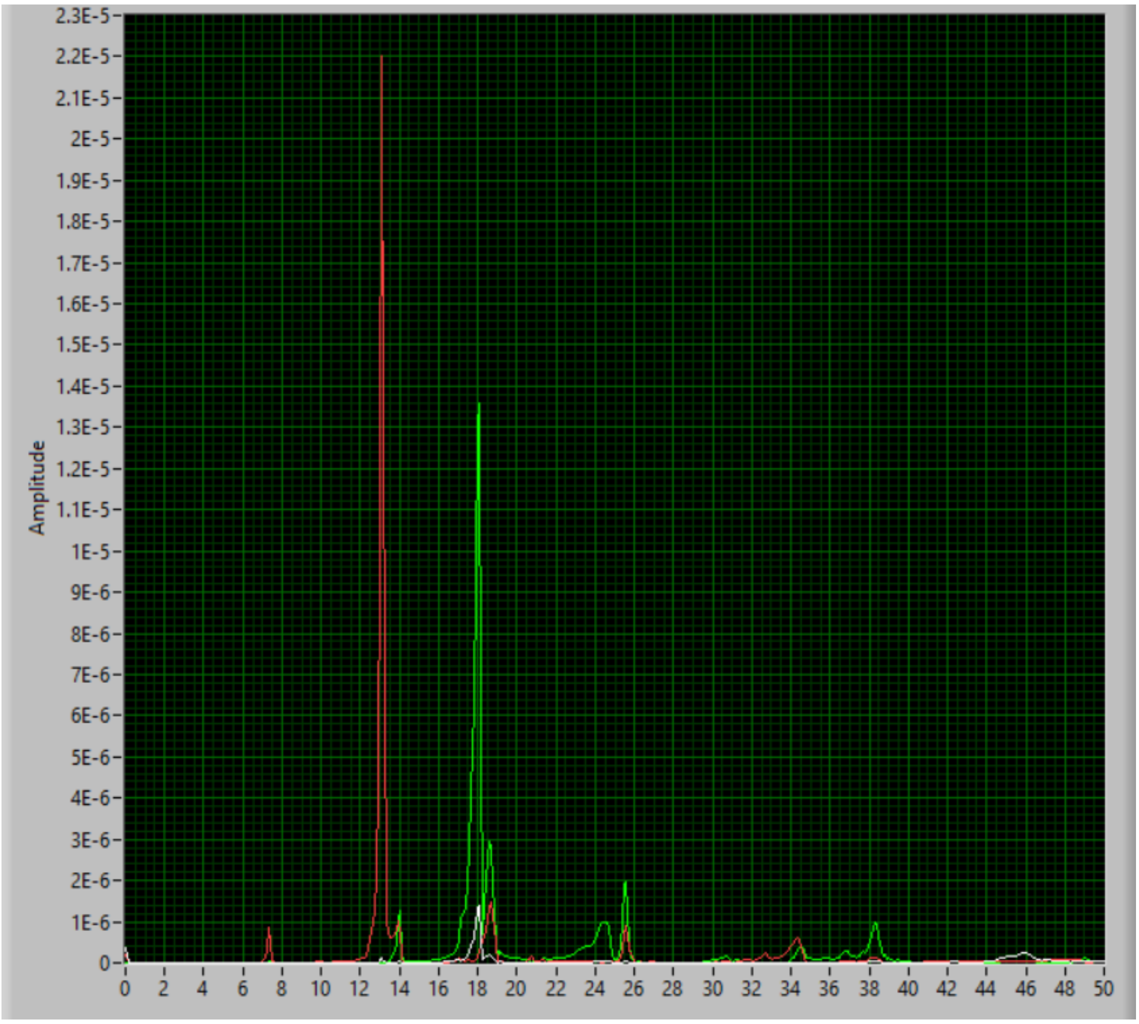

Figure D.7: Frequency plot of the third test run scaled to $[0, 50]Hz$.

D.3 Resulting plots from the third impact test

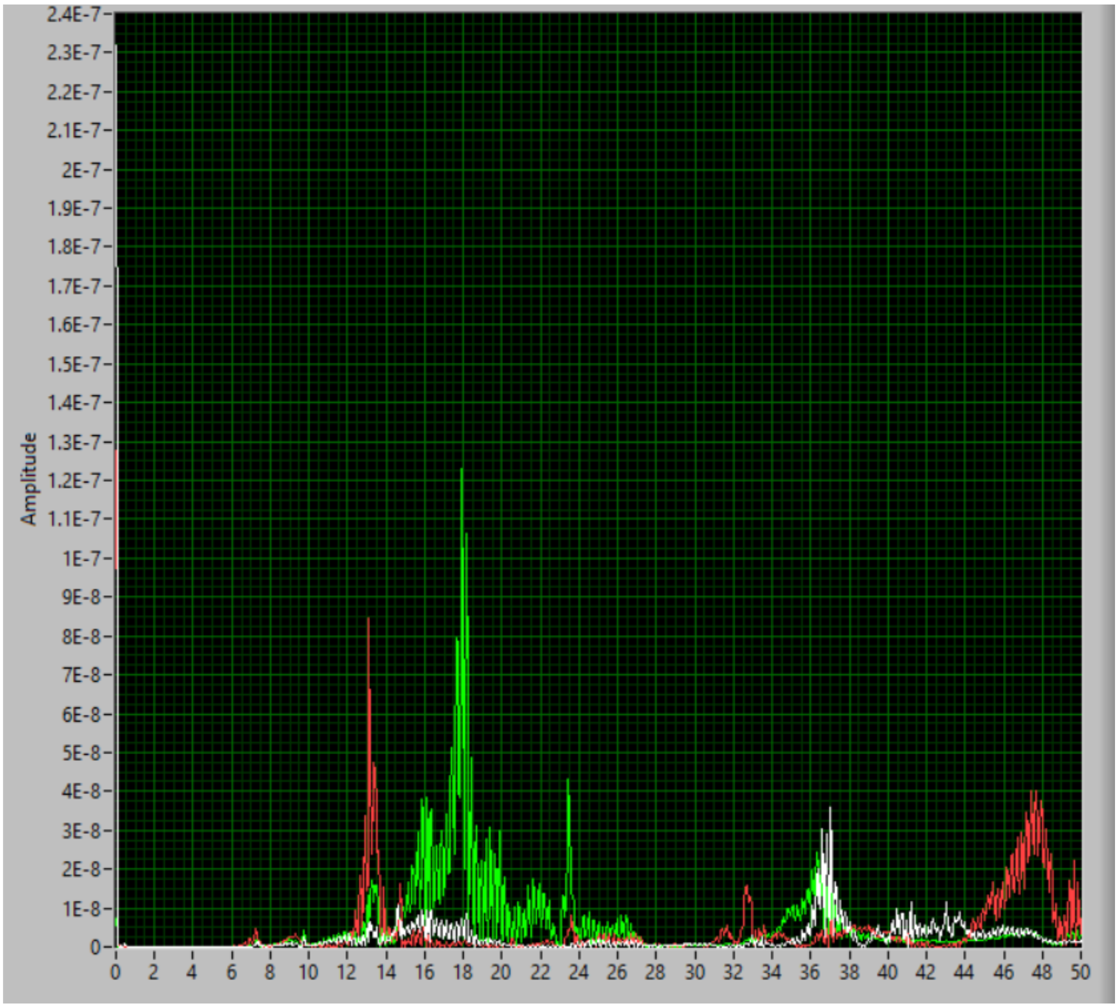

Figure D.8: Frequency plot of the first test run scaled to $[0,50]Hz$.

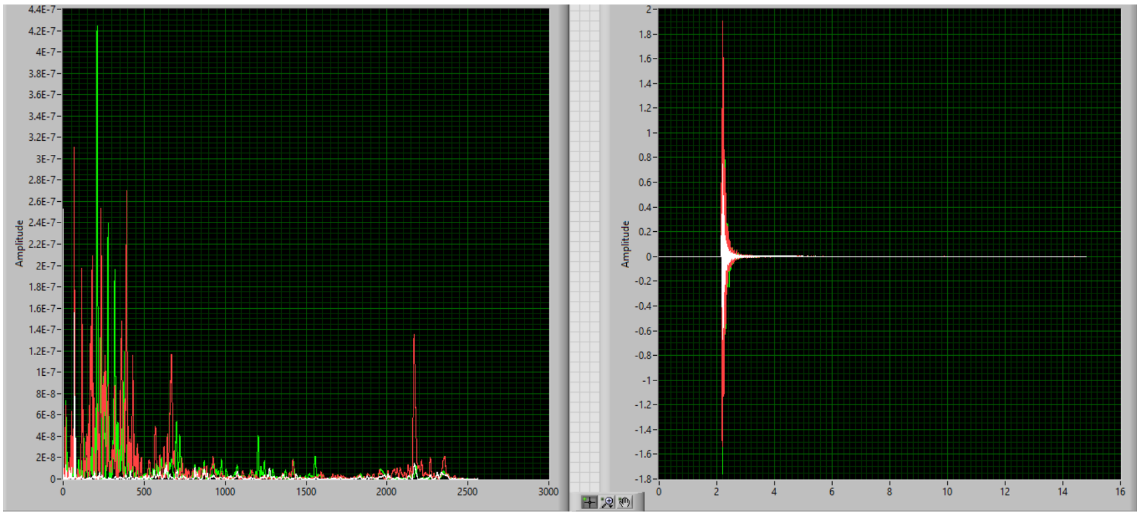

Figure D.9: Plots of the second test run.

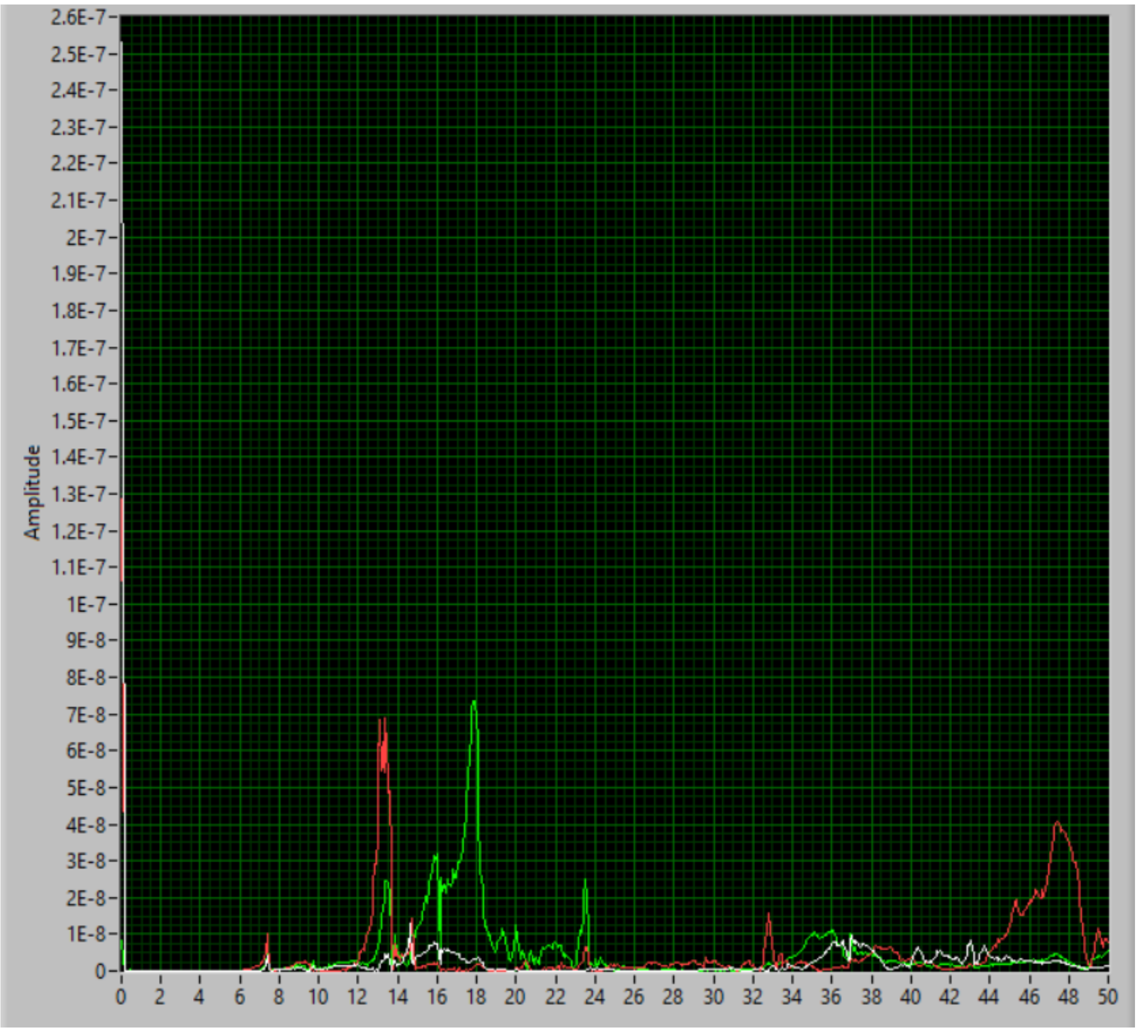

Figure D.10: Frequency plot of the second test run scaled to $[0,50]Hz$.

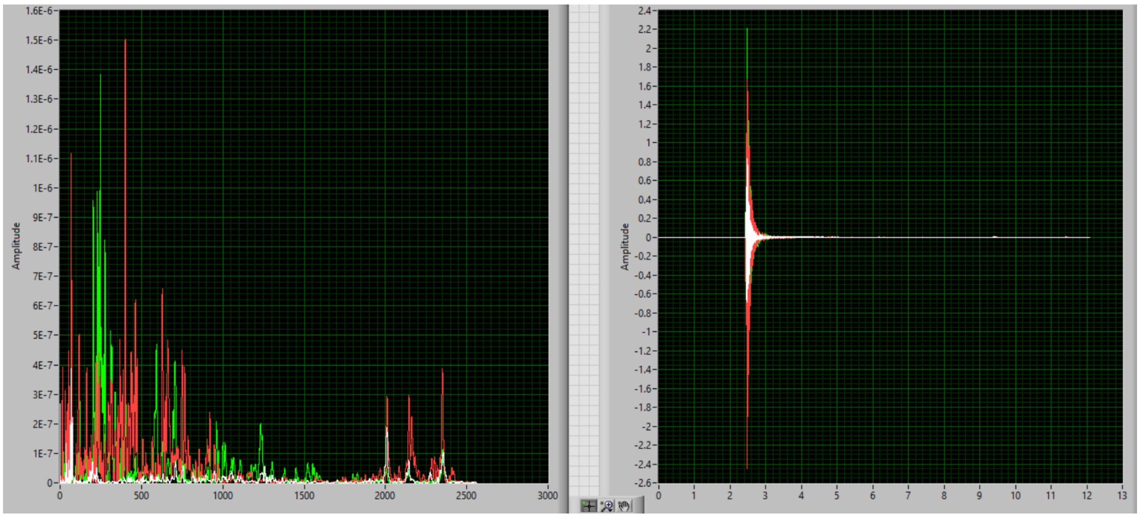

Figure D.11: Plots of the third test run.

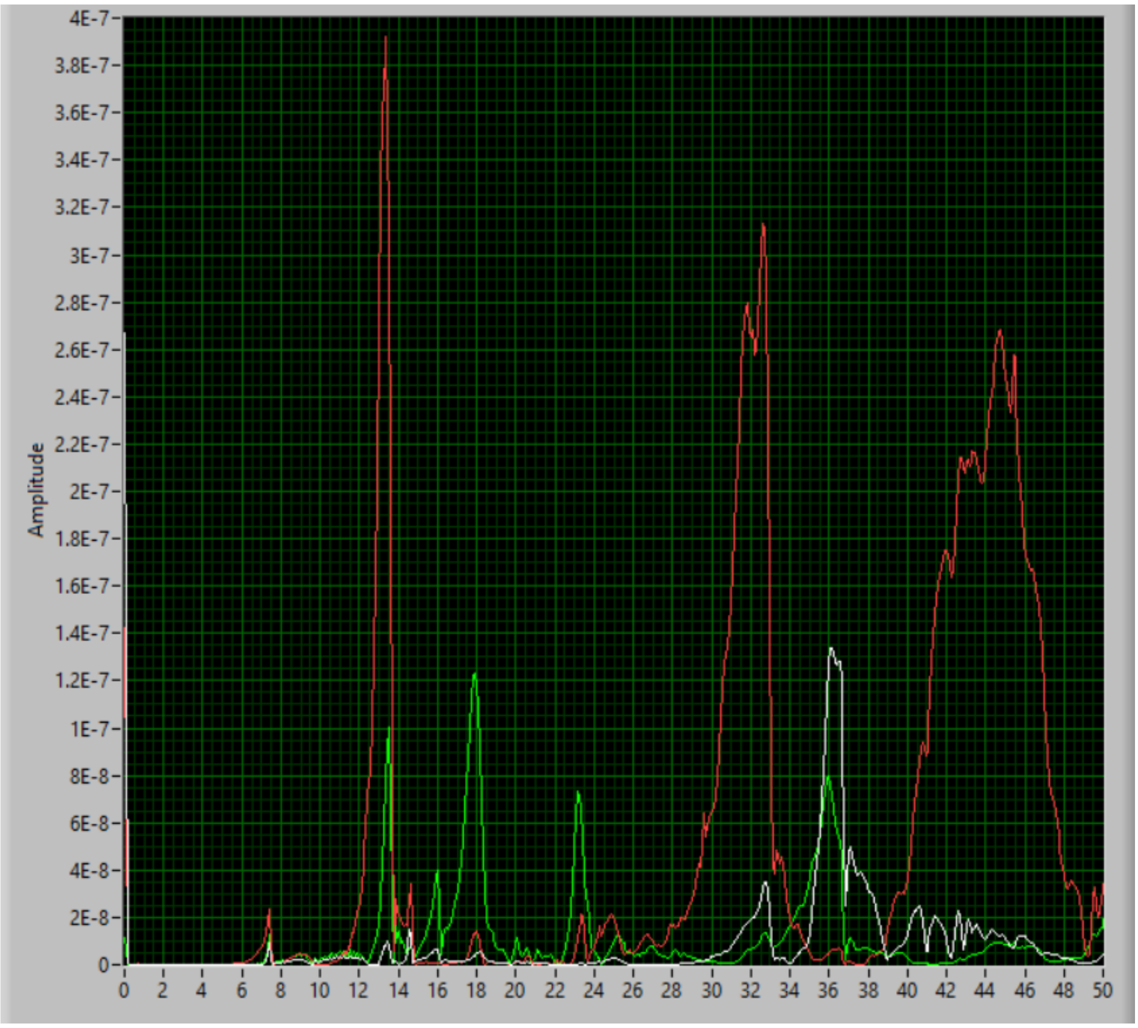

Figure D.12: Frequency plot of the third test run scaled to $[0,50]Hz$.